

# Moisture Content Measurements Using Time-domain Techniques

by  
Bin Xiao

B. Eng., Tsinghua University, 1990

A Thesis Submitted in Partial Fulfillment of the  
Requirements for the Degree of

MASTER OF APPLIED SCIENCE

in the Department of  
Electrical and Computer Engineering

We accept this thesis as conforming  
to the required standard



---

Dr. S. S. Stuchly, Supervisor



---

Dr. A. Zielinski, Departmental Member



Dr. G. F. McLean, Outside Member (Dept. of Mech. Eng.)



Dr. N. J. Livingston, External Examiner (Dept. of Biology)

@Bin Xiao, 1994

UNIVERSITY OF VICTORIA

*All rights reserved. This thesis may not be reproduced  
in whole or in part by mimeograph or other means,  
without the permission of the author.*

QC665

E4X5

Supervisor: Dr. S. S. Stuchly

## ABSTRACT

In this thesis, the time-domain reflectometry (TDR) technique applied to moisture content measurements of the dispersive and porous dielectric substance is studied. The TDR sensors with uniform sensitivity and definite sampling volume are proposed. Their characteristics are studied theoretically and experimentally. The propagation of electromagnetic pulses in dispersive media is also investigated. The dispersion of the dielectric constant smears the pulses and makes the accurate measurement of the propagation time difficult. The results partially explain the reason for the increase in the rise-time of the pulse in TDR moisture content measurements.

Examiners

[Redacted]

---

Dr. S. S. Stuchly, Supervisor

[Redacted]

Dr. ~~W.~~ Zielinski, Departmental Member

[Redacted]

Dr. G. F. McLean, Outside Member (Mech. Eng.)

[Redacted]

Dr. N. J. Livingston, External Examiner (Biology)

# Table of Contents

<b>Table of Contents</b>	<b>iii</b>
<b>List of Tables</b>	<b>vi</b>
<b>List of Figures</b>	<b>vii</b>
<b>Acknowledgments</b>	<b>xi</b>
<b>1 Introduction</b>	<b>1</b>
1.1 Motivation . . . . .	1
1.2 Objectives of the Project . . . . .	2
1.3 Overview of the Thesis . . . . .	3
<b>2 State of the Art</b>	<b>5</b>
2.1 Review of Present Knowledge . . . . .	5
2.2 Moisture Content and Basic Measurement Method . . . . .	7
2.2.1 Definitions of moisture content . . . . .	7
2.2.2 Gravimetric method of moisture content measurement . . . . .	7
2.3 Dielectric Properties of Soils . . . . .	8
2.3.1 Dielectric properties of porous materials. . . . .	8
2.3.2 Dielectric constant of soils . . . . .	11
2.3.3 Loss tangent of soils. . . . .	11
2.4 Time-Domain Reflectometry (TDR) . . . . .	14
2.4.1 Theory of the TDR technique . . . . .	14
2.4.2 TDR system and measurement procedure . . . . .	17
2.5 TDR Application to Moisture Content Measurements. . . . .	18
2.6 TDR Sensors for Moisture Content Measurements . . . . .	21
2.6.1 Coaxial transmission line. . . . .	21
2.6.2 Two-rod parallel line . . . . .	21
2.6.3 Multi-rod sensors . . . . .	21

2.6.4	Remote shorting diode sensor . . . . .	23
2.6.5	Other sensors . . . . .	26
<b>3</b>	<b>Analysis of Sensors</b>	<b>28</b>
3.1	Analysis of TDR Sensors . . . . .	28
3.1.1	Spatial weighing function . . . . .	28
3.1.2	Spatial weighing functions of sensors . . . . .	30
3.2	Characteristic Impedance of Sensors . . . . .	33
3.2.1	Characteristic impedance of TEM transmission lines . . . . .	33
3.2.2	Characteristic impedance of parallel plates . . . . .	34
3.3	Pulse Propagation in Porous Media . . . . .	36
3.3.1	Debye relation of permittivity . . . . .	36
3.3.2	Time Domain Maxwell's equations in Debye medium . . . . .	38
3.3.3	FDTD implementation of Maxwell's equations . . . . .	40
<b>4</b>	<b>Numerical Results</b>	<b>42</b>
4.1	Sensitivity of Sensors . . . . .	42
4.1.1	Parallel-plate sensor . . . . .	43
4.1.2	Parallel-plate sensor with dielectric shield . . . . .	45
4.1.3	Sensor with Rogowski's Profile . . . . .	49
4.1.4	Uniform field sensor . . . . .	53
4.1.5	Sensors with three electrodes . . . . .	56
4.2	Pulse Propagation - FDTD Results . . . . .	58
4.2.1	Signal analysis for TDR system . . . . .	58
4.2.2	Pulse propagation in water . . . . .	62
4.2.3	Pulse propagation in wet soil . . . . .	66
<b>5</b>	<b>Sensitivity Experiment</b>	<b>69</b>
5.1	Experimental Techniques . . . . .	69
5.1.1	Objectives . . . . .	69
5.1.2	Perturbation theory . . . . .	70
5.1.3	Principle of experiment . . . . .	71
5.1.4	Experiment system . . . . .	72
5.2	Experimental Results . . . . .	74
5.2.1	Weighing function measurement . . . . .	74
5.2.2	Uncertainty analysis . . . . .	77
<b>6</b>	<b>Discussion and Conclusions</b>	<b>79</b>
	<b>Bibliography</b>	<b>82</b>
	<b>Appendix A Frequency Change by Dielectric Perturbation in Cavity</b>	<b>85</b>

**Appendix B Index for Abbreviations**

## List of Tables

Table 5.1. The sensitivity experiment data of the parallel-plate sensor.. . . .	75
---	----

## List of Figures

- Figure 2.1 Relaxation dispersion and absorption in liquid water [11].  $\epsilon'$  and  $\epsilon''$  are the dielectric constant and dielectric loss factor of water, respectively. 9
- Figure 2.2 Permittivity of a silty clay with 15% (g water/g soil) water content versus frequency [26]. . . . . 10
- Figure 2.3 Dielectric constant vs. temperature for a surface Caldwell clay loam, water content 32.4% [4]. . . . . 12
- Figure 2.4 The loss tangent of Goodrich clay at 24 °C as a function of frequency at two water contents (g water/g soil). The dielectric property data are from [3]. . . . . 13
- Figure 2.5 The loss tangent of a kind of loamy soil vs. frequency at 25 °C, 2.2% water content. The dielectric property data are from [27]. . . . . 13
- Figure 2.6 The loss tangent of a kind of sandy soil vs. frequency at 25 °C, 16.8% water content. The dielectric property data are from [27]. . . . . 14
- Figure 2.7 The effect of loss factor on the propagation velocity for the TEM waves. The relative error is calculated by comparison of (2.10) and (2.11). . . . . 16
- Figure 2.8 Block diagram of a typical TDR system. . . . . 17
- Figure 2.8 The waveforms displayed on the oscilloscope. (a) The displayed waveform when the reflected wave is zero; (b) The displayed waveform when the reflected wave is not zero.  $T$  is twice of propagating time from the sampler to the mismatch point. . . . . 18
- Figure 2.9 An idealized representation of the TDR measurement output on a soil sample; time interval C-D represents the travel time in the test substance. . . . . 19
- Figure 2.10 Typical TDR trace in a wet soil from parallel transmission lines with an open circuit at the end. Point A: start of parallel transmission lines; point B: end of parallel transmission lines [1]. . . . . 20
- Figure 2.11 (a) Three-rod sensor; (b) Four-rod sensor. [15] . . . . . 22

Figure 2.12	Remote shorting diode circuit [18]. . . . .	23
Figure 2.13	Waveforms generated from a one-diode probe. The diode is at the surface of the soil [18]. (a) Measured waveforms; (b) Subtraction result. . . . .	24
Figure 2.14	Water boxes used to simulate the interfering reflections found in layered soil. (a) Experiment configuration; (b) Experimental waveforms [18].. . . .	25
Figure 2.15	Configurations of the discontinued impedance transmission line. (a) transmission line with unfilled discontinuities; (b) transmission line with discontinuities filled with dielectric. . . . .	26
Figure 3.1	The configuration of the coordinate axes ( $x_1, x_2$ ) on the plane $\Omega$ . . . . .	29
Figure 3.2	Two parallel-rod sensor. . . . .	32
Figure 3.3	Contour of the relative spatial sensitivity function for two parallel-rod sensor in the first quadrant of the plane [16]. The number $n$ on the contour indicates a level of $2^n$ . . . . .	32
Figure 3.4	Configuration of the parallel strip line. . . . .	35
Figure 3.5	The impedance vs. dimension parameter for broad strips. . . . .	35
Figure 3.6	Frequency dependance of the permittivity according to Debye relation ( $\epsilon_{rel} = \omega/2\pi = 1/2\pi\tau_0$ ) . . . . .	37
Figure 4.1	Configuration of the parallel-plate sensor and the selected coordinate system. . . . .	43
Figure 4.2	Field distribution along x-axis at $y=0$ (center between two plates). . . . .	44
Figure 4.3	Field distribution along x-axis at $y=a$ (on the surface of the plate). . . . .	44
Figure 4.4	Weighing factor for parallel-plate line along x-axis at $y=0$ and $y=a$ . . . . .	45
Figure 4.5	Configuration of the parallel-plate sensor with the dielectric shield. . . . .	46
Figure 4.6	Field distribution along x-axis at $y=0$ (at the center between the electrodes). The electric field is normalized to that of the parallel-plate sensor, and the widths is normalized to that of the parallel-plate sensor, too. . . . .	46
Figure 4.7	The field distribution along x-axis at $y=0.8a$ (at the surface of dielectric shield). The electric field is normalized to that of the parallel-plate sensor, and the widths is normalized to that of the parallel-plate sensor, too. . . . .	47
Figure 4.8	The field distribution along x-axis at $y=a$ (at the electrode). The electric field is normalized to that of the parallel-plate sensor, and the width is normalized to that of the parallel-plate sensor, too. . . . .	47
Figure 4.9	Weighing factor along x-axis at $y=0$ and $y=0.8a$ . The weighing factor is normalized to that of the parallel-plate sensor. . . . .	48
Figure 4.10	Weighing factor along x-axis at $y=a$ . The weighing factor is normalized	

	to that of the parallel-plate sensor. . . . .	48
Figure 4.11	Rogowski's profile [31]. . . . .	50
Figure 4.12	Configuration of the Rogowski's profile sensor. The half width of the electrode is normalized to 1. The width of parallel plates which can generate such a profile is 1.35. . . . .	50
Figure 4.13	Field distribution for Rogowski's profile along x-axis at $y=0$ (center between two electrodes).. . . . .	51
Figure 4.14	Field distribution for Rogowski's profile along x-axis at $y=a$ . . . . .	52
Figure 4.15	Weighing factor of Rogowski's profile sensor along x-axis at $y=0$ and $y=a$ . . . . .	52
Figure 4.16	Half contour of the uniform field electrode [32]. . . . .	53
Figure 4.17	Configuration of the sensor with a flat part at center and curved part at the edge. . . . .	54
Figure 4.18	Field distribution along x-axis at $y=0$ (center between the two electrodes). . . . .	54
Figure 4.19	Field distribution along x-axis at $y=a$ (along parallel part of the electrodes). . . . .	55
Figure 4.20	Weighing factor along x-axis at $y=0$ and $y=a$ . . . . .	55
Figure 4.21	Configuration of the three-electrode sensor. The width of the Rogowski's profile which has the same parameters as in Fig. 4.12 is normalized to 1. . . . .	56
Figure 4.22	Field distribution along x-axis at $y=0$ (along the center electrode). The lines represent different width of central electrodes. The electric field is normalized to that of three-parallel-plate sensor. . . . .	57
Figure 4.23	Weighing factor along x-axis at $y=0$ (along the center electrode). The lines represent different width of central electrodes. The weighing factor is normalized to that of three-parallel-plate sensor. . . . .	57
Figure 4.24	The normalized incident ramp signal with the rise time $t_r$ . . . . .	59
Figure 4.25	The FFT spectrum of the ramp signal with the rise time of 20, 40, 60, 80, 100, 120, 140, 160, 180, and 200 ps. . . . .	59
Figure 4.26	The normalized triangular pulse with the pulse width $t_p$ . . . . .	60
Figure 4.27	The FFT spectrum of the triangular pulse signal with the pulse width 20, 40, 60, 80, 100, 120, 140, 160, 180, and 200 ps. . . . .	60
Figure 4.28	The normalized gaussian pulse. . . . .	61
Figure 4.29	The FFT spectrum of the gaussian pulse with the pulse width 20, 40, 60, 80, 100, 120, 140, 160, 180, and 200 ps. . . . .	61
Figure 4.30	Gaussian pulse in air at $z=0$ as a function of time. . . . .	63
Figure 4.31	Gaussian pulse propagating in water as a function of time. The pulse	

	width is 100 ps. . . . .	.63
Figure 4.32	Gaussian pulse propagating in water as a function of distance. The pulse width is 100 ps . . . . .	.64
Figure 4.33	Ramp signal propagating in pure water as a function of time. The rise time is 100 ps. . . . .	.64
Figure 4.34	Ramp signal propagating in pure water as a function of distance. The rise time of the ramp is 100 ps. . . . .	.65
Figure 4.35	Gaussian pulse propagating in soil as a function of time. The pulse width is 100 ps. . . . .	.66
Figure 4.36	Gaussian pulse propagating in soil as a function of distance. The pulse width is 100 ps. . . . .	.67
Figure 4.37	Ramp signal propagating in soil as a function of time. The rise time of the ramp is 100 ps. . . . .	.68
Figure 4.38	Ramp signal propagating in soil as a function of distance. The rise time is 100 ps. . . . .	.68
Figure 5.1	The configuration of the experiment system. . . . .	.73
Figure 5.2	The coordinate system of the test parallel-plate sensor. . . . .	.75
Figure 5.3	The normalized experiment and theoretical weighing factors at $y=0.0$ cm. The solid line is the theoretical result and the separate data points are experimental results. . . . .	.76
Figure 5.4	The normalized experiment and theoretical weighing factors at $y=1.0$ cm. The solid line is the theoretical result and the separate data points are experimental results. . . . .	.77

# Acknowledgments

I would like to thank my supervisor, Dr. S. S. Stuchly, for his guidance, constant encouragement and great patience throughout the study and the research work of my M. A. Sc. program at the University of Victoria. I am also grateful to him for his financial support to my study and the research work.

I would like to thank Dr. M. Okoniewski and Mr. K. Caputa with whom I had many stimulating discussions.

I would also like to thank Dr. A. Zielinski and Dr. G. McLean for being my supervisory committee and the faculty members and staff at the University of Victoria from whom I got much help.

# Chapter 1

## Introduction

### 1.1 Motivation

Soil moisture content is of fundamental importance in many areas, especially in agriculture, forestry, hydrology and civil engineering. Knowledge of soil moisture content and its profile over large areas is necessary for applications to crop management and irrigation control. Significant economic benefits can be obtained by understanding soil properties through the moisture content investigation.

A rapid, reliable, *in-situ*, non-destructive and accurate method is required in various applications. Currently, available methods involve point measurements, which are too costly for extensive use, or remotely sensed techniques, which at best detect surface conditions [1]. The neutron moderation technique is used for monitoring at established sites. However, the need for site calibration and the inherent radiation hazard make this technique less than ideal [1]. The direct measurement of water content by removal and drying of samples is reliable and the most accurate, but is destructive and time consuming, and thus impractical for large scale, *in-situ* measurement [1].

An ideal method would use a physical property of the soil to conduct indirect measurement. Such a property should be primarily a function of water content and should be measured directly and reliably. The dielectric constant of soil is such a property and the time-domain reflectometry (TDR) technique is the measurement method which is consistent with above requirements. The original idea of using TDR for measurement of the

dielectric properties was proposed by Fellner-Felldg [2].

The reason why TDR was chosen as the measurement method is, first, the technique measures the average moisture content along the sensor, while this property is not available by other techniques, second, TDR system is a wide band system, which provides wider frequency range than those frequency domain methods.

## 1.2 Objectives of the Project

The objective of the project is to study the electromagnetic wave propagation along the TDR sensor immersed in the dispersive and inhomogeneous dielectric, investigate the influence of the wave behavior on TDR measurements and improve the sensor's performance.

In the investigation of the wave propagation along the sensor, the dielectric is assumed to be described by Cole-Cole equation [3]. It is also assumed to occupy infinite half space and be homogeneous or stratified along the propagation direction. Incident fields are assumed to be TEM pulses, which means the electromagnetic pulses propagates along a TEM transmission line, because the TDR system supports TEM mode and usually utilizes short rise-time ramp or pulse signals. In one-dimensional problem, the behavior of the TEM wave is similar to that of a plane wave. The wave forms in the dielectric are calculated by the Finite-Difference Time-Domain (FDTD) method. The calculation results are expected to show the performance of the electromagnetic pulses used in the TDR techniques in dispersive media. The effects of the dispersion of the dielectric constant on the wave are investigated.

The sensitivity of the sensor is also studied. The weighing function is obtained under the perturbation assumption. The spatial responses of the TDR sensors to small perturbations of the dielectric constant of soils are obtained. The quasi-static assumption is used in the sensor's sensitivity study. Sensors with uniform sensitivity are designed and their characteristics are investigated. Experiments are conducted using perturbation techniques to test the sensitivity of the proposed sensors and confirm the theoretical sensi-

tivity results.

### 1.3 Overview of the Thesis

The foundation of the TDR technique depends on the fact that the propagation velocity of the electromagnetic wave is determined by the permittivity of the dielectric in which the electromagnetic wave propagates. Since the TDR technique utilizes the TEM mode as propagation mode, the wave's propagation velocity in the TDR system is the same as that in free space, provided that the wave propagates in the same medium.

For low loss media, the propagation velocity is determined by the dielectric constant and is independent of the loss factor. This conclusion is valid for the loss tangent  $\tan\delta < 0.3$  such that the maximum relative error of propagation velocity is below 1%. The effect of the loss factor on the propagation velocity is negligible even when the loss factor is large [1] [4] [5].

The velocity of propagation can be determined by measuring the time that the wave propagates along the sensor of a known length. The relationship between time, which can be read directly from the instrument, and the dielectric constant of the measured substance has been obtained. The relationship between the water content and the dielectric constant has also to be determined. Many researches have obtained this relationship through calibration [4] [6] [7] [8] [9].

The TDR utilizes a short rise-time ramp signal or a short pulse to measure the propagation time. The trace analysis is the key for identifying the propagation time, and in turn the moisture content. The media were assumed to be non-dispersive in all TDR studies. However, soil is a dispersive dielectric [3], and the signal is smeared as it propagates along the direction of propagation. The propagation of pulses can be studied by the FDTD method [10].

Sensor design is a key part of the TDR system. Its performance is the determining factor of whole system's performance. Although they have linear longitude sensitivity functions, all the TDR sensors now developed have inhomogeneous lateral sensitivity

which is dependent on the water distribution. To improve the performance of the sensor, the uniform spatial sensitivity is needed. An optimized sensor was developed to comply with the above specifications.

## Chapter 2

### State of the Art

#### 2.1 Review of Present Knowledge

Water content measurement in soil is of critical importance in agriculture and forestry because their productions are mainly limited by water's availability. Furthermore, non-intrusive and reliable measurements of water content are in great demand in many other industries. In spite of these demands, measurement systems which provide highly accurate, routine and non-destructive measurements at a reasonable cost are still not generally available for common use. However, time-domain reflectometry (TDR) appears to show the potential of meeting many of the criteria related to measurements of water content in porous media.

Considerable attention has been concentrated on the determination of water content from measuring electrical properties of wet substances. Electrical conductance techniques for example, have drawbacks in that both electrical conductivity and water content must be determined independently to provide accurate measurement results. Due to these limitations, research has been concentrated on techniques based on the measurement of the dielectric properties [2] [4] [11] [12] [13] [14]. These techniques can be categorized as capacitance, microwave transmission and reflection, and TDR [4] [13] [14].

Microwave transmission and reflection techniques have been used to determine the water content of porous materials. These include measurements of sample's impedance, measurements of frequency shift, polarization change, transmission and reflection coeffi-

cients and measurements of complex resonant frequency [11] [12] [13]. Most of these techniques are not practical for *in situ* measurements because of the complex and expensive equipments required. Detailed calibration must be conducted for each material being investigated by these techniques and this limits their broad applications.

Time-domain reflectometry (TDR) involves the measurement of the propagation velocity of a pulse with radio frequency energy as it travels along a transmission line buried in the test material (e.g., soil). This technique has a major advantage over above techniques in that water content measurement is independent of the test material's electrical conductivity [4]. This is important in many applications, for instance, in soil water content measurements where usually significant amount of salts are present.

Typical TDR sensors consist of a simple transmission line. A coaxial line sample holder is used in laboratory measurements. Two-rod lines are most frequently used in field measurements. Three- and four-rod lines are improvements of the two-rod line. This design attempts to emulate the geometry of the coaxial transmission line [15]. It has some advantages over two-rod probes in that it can connect directly to the coaxial cable without using a balun so that it is easier to match the impedance of the sensor. This arrangement also samples a slightly larger volume of the test material. However, all configurations presently used have a highly non-uniform electric field distribution, and hence highly non-uniform measurement sensitivity [16] [17].

An important improvement of the sensor is achieved by addition of remote shorting diodes to reduce time measurement error [18]. This improvement along with subtraction techniques greatly improves the effective amplitude of desired reflections and reduce the background noise. With multiple diodes, this technique allows to measure the profile of water in soil.

Several TDR systems for measuring soil water content were developed [19] [20]. These systems are used to automatically monitor soil water content in real time. They can also carry out *in situ*, multiplexing and long term measurements.

Recent research [5] [21] [22] found that the attenuation of the reflected TDR signal

can be used to infer soil electrical conductivity. This proposal has been investigated further by Topp *et al* [23] and Yanuka *et al* [24].

## 2.2 Moisture Content and Basic Measurement Method

### 2.2.1 Definitions of moisture content

Moisture content on gravimetric basis is usually defined as relative content  $W_r$  [11]

$$W_r = \frac{m_m - m_d}{m_m} \quad (2.1)$$

or as absolute moisture content  $W_a$  [11]

$$W_a = \frac{m_m - m_d}{m_d} \quad (2.2)$$

where  $m_m$  is the mass of wet material, and  $m_d$  is the mass of dry material.

Similarly, moisture content on volumetric basis can be defined as relative content  $\theta_r$

$$\theta_r = \frac{v_m - v_d}{v_m} \quad (2.3)$$

or as absolute moisture content  $\theta_a$

$$\theta_a = \frac{v_m - v_d}{v_d} \quad (2.4)$$

where  $v_m$  is the volume of wet material, and  $v_d$  is the volume of dry material.

### 2.2.2 Gravimetric method of moisture content measurement

Gravimetric method is the direct measurement method of moisture content. This method is simple, reliable and cheap, though it is destructive and time consuming [1].

The procedure of this method is straightforward. A soil sample is placed in a heat-proof dish of known weight, weighed, dried in an oven set at a temperature of 100-110 °C,

removed and allowed to cool down in a desiccator, then re-weighed. This procedure is repeated until the sample attains a constant weight. The gravimetric water content of the sample is the mass of water per unit mass of dry soil, which is described in (2.2).

A good oven, which is ventilated and distributes the heat evenly, is required. The heating time required to dry a sample to constant weight is affected by the oven's efficiency and the size, condition, and number of samples in it. An oven temperature of 105°C and a 24-hour drying period are widely adopted standards [1]. A constant weight can be assumed to have been achieved when the changes between two weighing results are less than 0.1% of the original sample weight.

## 2.3 Dielectric Properties of Soils

Since TDR technique is primarily used in soil moisture content measurements and since the available soil data are more detailed than for other materials, the review in this section is concentrated on soil. However, the mixture theory can be applied to any porous medium.

### 2.3.1 Dielectric properties of porous materials

Moist soil can be considered, in the physical sense, as a three-component mixture of air, solid substance, and water. Water in soil appears in the forms of bound and free water. The model of the dielectric constant of soil  $\epsilon'$  can be described as follows [25]:

$$\epsilon'^a = \epsilon'_s{}^a f_s + \epsilon'_w{}^a f_w + \epsilon'_a{}^a f_a \quad (2.5)$$

where  $a$  is the exponent of the dielectric constants  $\epsilon'$ ;  $f_s$ ,  $f_w$  and  $f_a$  are the volume fraction of solid substance, water and air, respectively, and  $\epsilon'_s$ ,  $\epsilon'_a$  and  $\epsilon'_w$  are the dielectric constants of solid substance, air and water, respectively. The exponent  $a$  is approximately 0.5 and some physical basis has been found [25].

In the microwave frequency range, the dielectric constant of water varies with frequency from 80 to 10. The dielectric constants of the other two parts in soil are much

lower than water: the dielectric constant of dry soil is around 4 and of air is 1. Therefore, a small amount of water causes significant change of the dielectric constant of soil. The amount of water in soil is the dominant factor that affects the dielectric constant of soil [4] [26]. Any change in the dielectric constant of soil predominately reflects the change in water content.

Water is a dispersive substance which means that its dielectric constant is a function of frequency. In the radio and microwave frequency range, the dispersion results from the directional relaxation of the molecule. Water molecule can be modeled as a dipole and it will take time  $\tau$  to re-align in the electric field. When the frequency is around  $1/\tau$ , the imaginary part of water's permittivity is high and the real part decreases in value with the increasing frequency. This frequency with the highest loss factor is called relaxation frequency. The relaxation frequency of liquid water at room temperature is around 17 GHz (See Fig. 2.1), while bound water has much lower relaxation frequency and smaller dielectric constant.

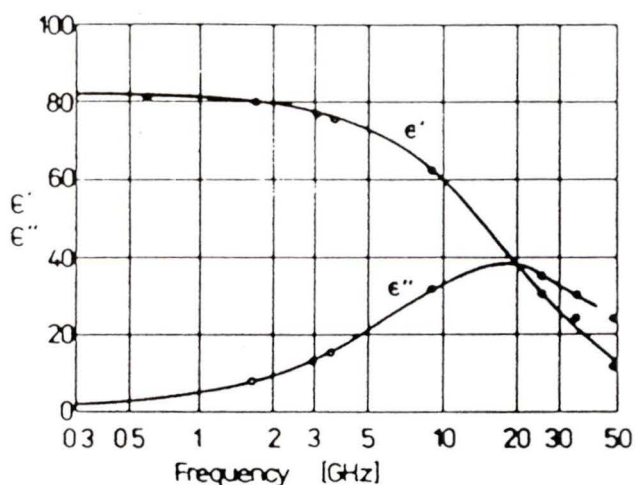


Figure 2.1 Relaxation dispersion and absorption in liquid water [11].  $\epsilon'$  and  $\epsilon''$  are the dielectric constant and dielectric loss factor of water, respectively.

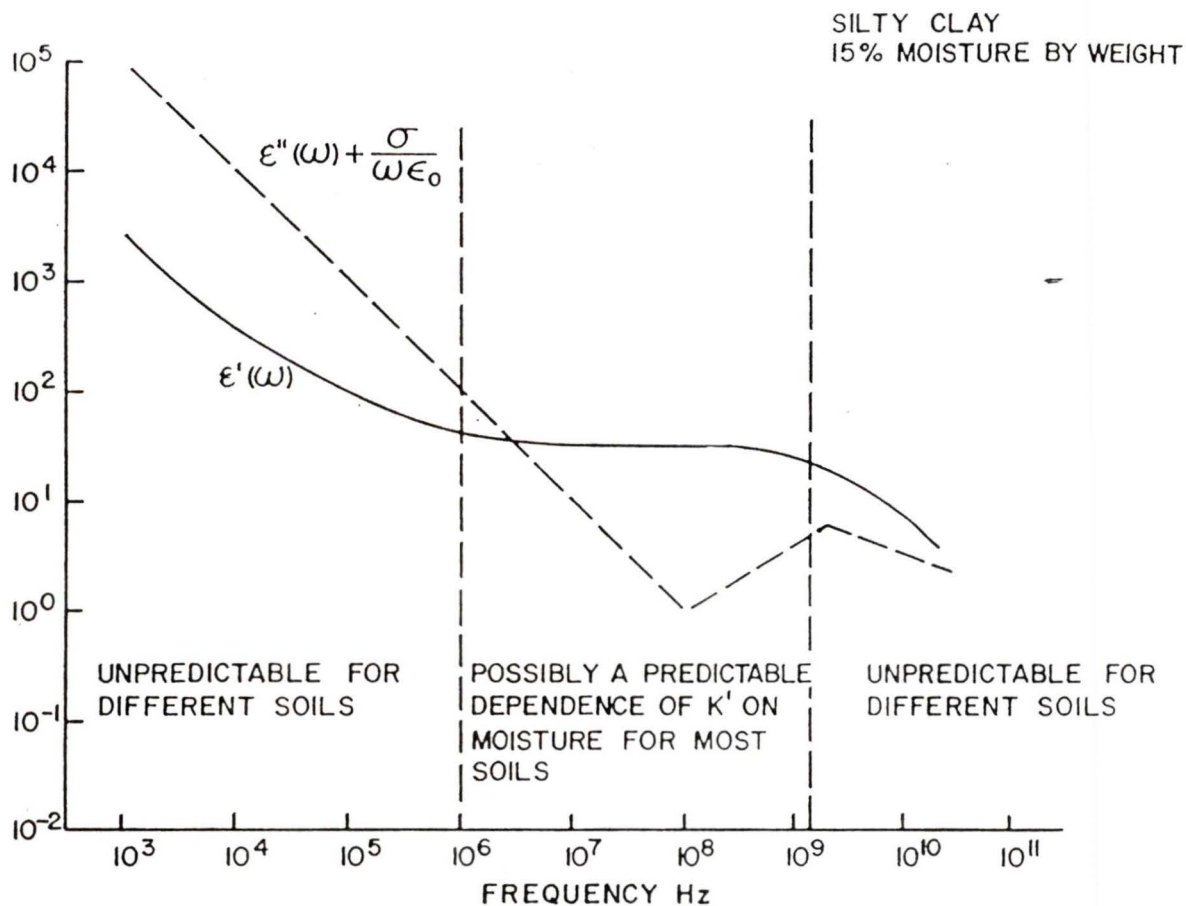


Figure 2.2 Permittivity of a silty clay with 15% (g water/g soil) water content versus frequency [26].

Moist soil is also a dispersive substance. The relaxation observed in soil can be mainly attributed to the presence of water. But the relaxation frequency is around 10 GHz rather than 17 GHz as for water (See Fig. 2.2) [26]. However, there is no evidence that the lower relaxation frequency is due to the bound water in soil [3].

### 2.3.2 Dielectric constant of soils

The relation between the volumetric water content of free water and the dielectric constant of soil can be expressed by an empirical equation. There are many different empirical relations depending on the model used. It has been shown that the relationship is not strongly dependent on soil type, density, temperature (See Fig. 2.3), and soluble salt content. Therefore, the relation is primarily dominated by water content. The widely accepted relation at frequencies from 1 MHz to 1 GHz is [4]:

$$\theta_v = A + B\varepsilon' + C\varepsilon'^2 + D\varepsilon'^3 \quad (2.6)$$

where  $\theta_v$  is the volumetric water content,  $A=-0.053$ ,  $B=0.0292$ ,  $C=-5.5 \times 10^{-4}$  and  $D=4.3 \times 10^{-6}$ . The dielectric constant of soil obtained from the volumetric water content can also be found [4]:

$$\varepsilon' = 3.03 + 9.3\theta_v + 146.0\theta_v^2 - 76.7\theta_v^3 \quad (2.7)$$

Research [26] also showed that the dielectric constant of soil changes little in the frequency range from 1 MHz to 1 GHz so that the dielectric constant of soil can be considered as constant in this frequency range.

### 2.3.3 Loss tangent of soils

Loss tangent is the ratio of the loss factor  $\varepsilon''$  and the dielectric constant  $\varepsilon'$  of the dielectric substance:  $\tan \delta = \varepsilon''/\varepsilon'$ . Davis and Annan [26] summarized the dielectric constant and the loss factor of typical soils. They divided the frequency range into three regions and presented physical phenomena responsible for the relaxation:

1.  $f < 1$  MHz: Space charge and electrochemical relaxation mechanisms with inherent frequency dependence generate complicated dielectric dispersion. Dielectric constant of soil is not only dependent on water content in this region.

2.  $f > 1$  GHz: The soil shows frequency dependent properties due to the relaxation of water. The relaxation causes the permittivity of moist soil to be temperature dependent.
3.  $f \sim 1$  MHz to 1 GHz: The dielectric constant varies with frequency less than 10%. It is strongly dependent on the volumetric water content and weakly dependent on frequency, soil type, density and temperature.

It can be shown that for the loss tangent  $\tan \delta < 0.3$ , the effect of the loss factor on the propagation velocity, and the error in the measured moisture content due to the loss factor are negligible.

From the data collected in literature [3] and [27], the loss tangent of soil is illustrated in Fig. 2.4, Fig. 2.5 and Fig. 2.6. We can see that the loss tangent is smaller than 0.3 which is the criterion of using the dielectric constant instead of the permittivity in calculating propagation velocity, in frequency range from 1 MHz to 1 GHz.

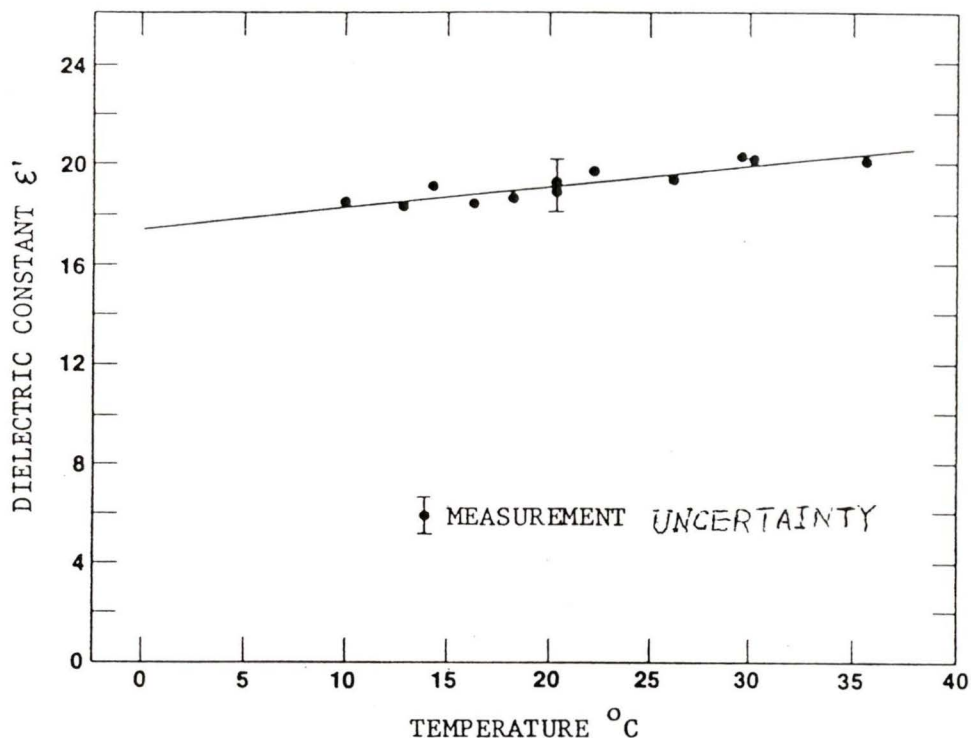


Figure 2.3 Dielectric constant vs. temperature for a surface Caldwell clay loam, water content 32.4% [4].

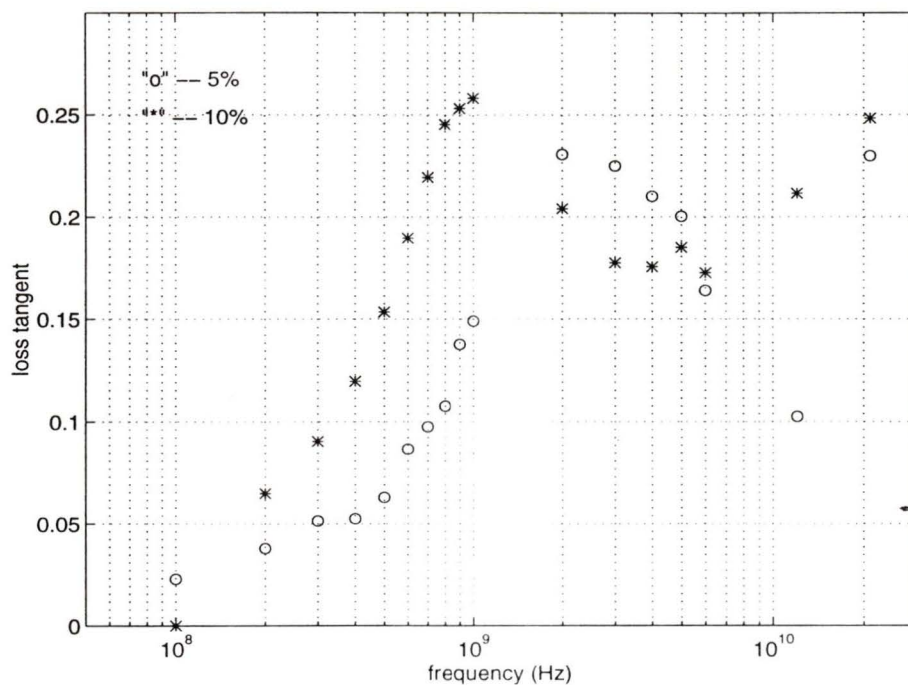


Figure 2.4 The loss tangent of Goodrich clay at 24 °C as a function of frequency at two water contents (g water/g soil). The dielectric property data are from [3].

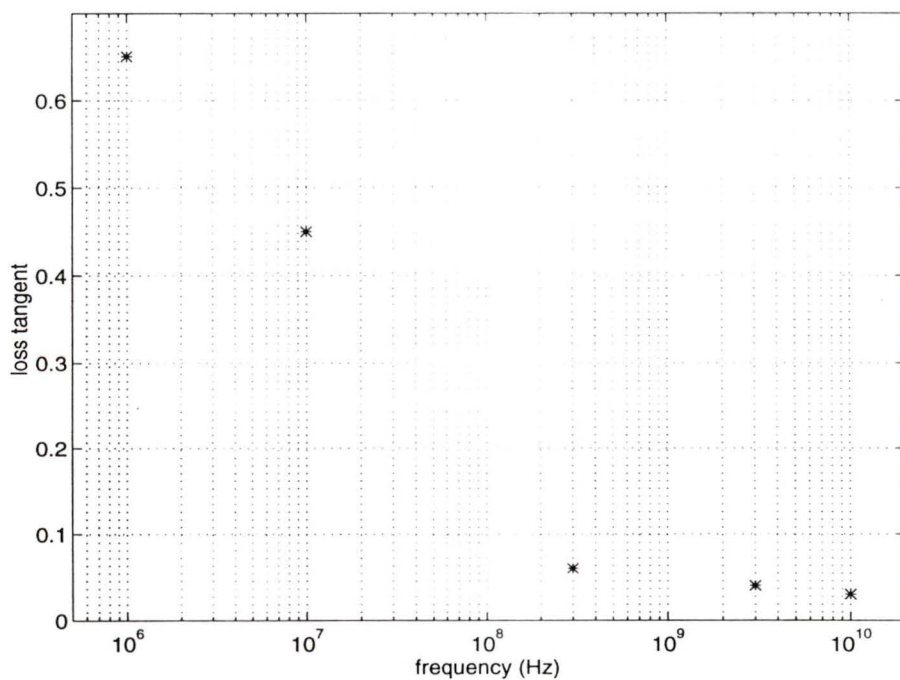


Figure 2.5 The loss tangent of a kind of loamy soil vs. frequency at 25 °C, 2.2% water content. The dielectric property data are from [27].

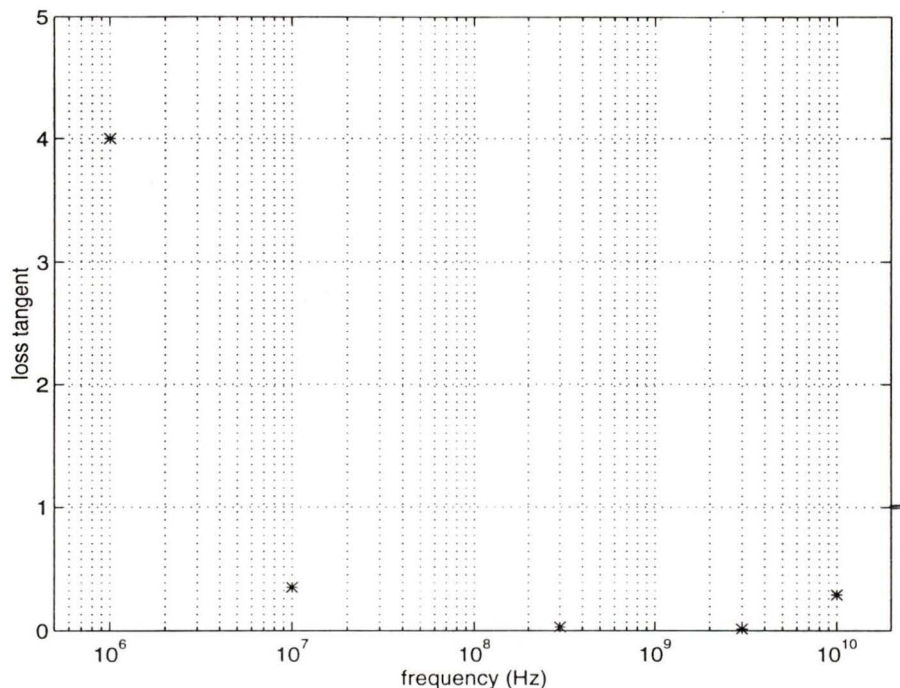


Figure 2.6 The loss tangent of a kind of sandy soil vs. frequency at 25 °C, 16.8% water content. The dielectric property data are from [27].

## 2.4 Time-Domain Reflectometry (TDR)

### 2.4.1 Theory of the TDR technique

Time domain reflectometry is not a new technique. Traditionally, it is used by electrical engineers to locate discontinuities in power transmission line systems through monitoring reflections of an electrical pulse. It is also used in evaluating the transmission line, e.g. coaxial cable, and in analyzing the impedance characteristics of a device terminating a transmission line. In recent years TDR found applications in monitoring moisture content in liquid and solid materials, especially in porous materials.

The foundation of the TDR technique in this application relates to the fact that the propagation velocity of the electromagnetic pulse is determined by the permittivity of a dielectric in which the wave propagates. Since the TDR technique utilizes the transverse

mode (TEM) wave due to the measurement system's structure, the wave's propagation velocity in the TDR system is the same as that in free space, provided that the wave propagates in the same medium.

The permittivity of a wet material may be expressed as:

$$\epsilon = \epsilon' - j\epsilon'' \quad (2.8)$$

where  $\epsilon$  is the permittivity of the dielectric material in which a wave propagates,  $\epsilon'$  is the dielectric constant and  $\epsilon''$  is the loss factor. The propagation velocity  $v$  in the dielectric material is [26]:

$$v = \frac{c}{\text{real}(\epsilon^{1/2})} \quad (2.9)$$

where  $c$  is the velocity of light in vacuum. And

$$\begin{aligned} \text{real}(\epsilon^{1/2}) &= \text{real}[(\epsilon' - j\epsilon'')^{1/2}] \\ &= \sqrt{\epsilon' \left( \frac{1 + \sqrt{1 + \tan^2 \delta}}{2} \right)} \end{aligned} \quad (2.10)$$

where  $\tan \delta = \epsilon''/\epsilon'$  is the loss tangent. So from (2.10), we can see when  $\tan \delta \ll 1$  [4] [11],

$$v = \frac{c}{\sqrt{\epsilon'}} \quad (2.11)$$

Therefore, the conclusion is, the propagation velocity of electromagnetic wave in low loss dielectric media is determined by the dielectric constant and independent of the loss factor. This is valid for  $\tan \delta < 0.3$ , under which condition, the calculation difference of the propagation velocity between formulae (2.10) and (2.11) is less than 1%. The relation between the relative velocity error and the loss tangent is illustrated in Fig. 2.7.

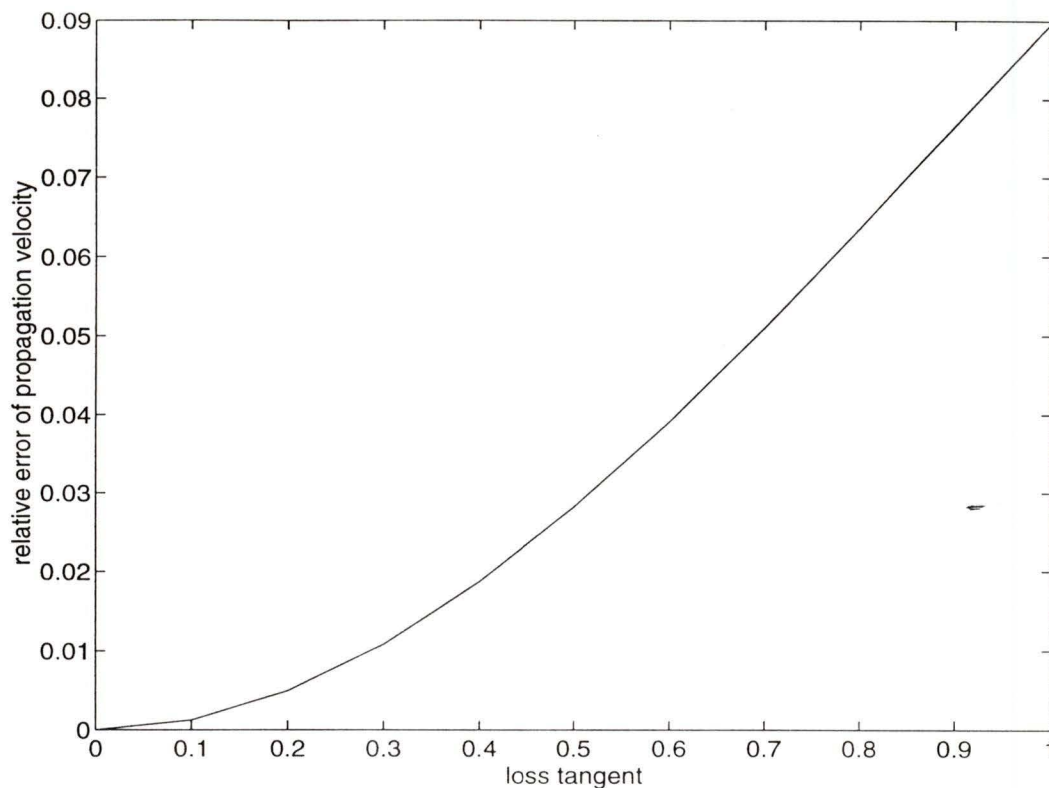


Figure 2.7 The effect of loss factor on the propagation velocity for the TEM waves. The relative error is calculated by comparison of (2.10) and (2.11).

To perform measurements, the sensor (a transmission line) is typically configured to have two discontinuities, usually at the beginning and the end of the line. Each of these discontinuities produces a reflection. The propagation velocity can be calculated by measuring the time interval between the two reflections. Assume that  $t$  is the measured time and  $L$  is the length of the sensor between the discontinuities. Then

$$v = \frac{2L}{t} \quad (2.12)$$

From (2.11) and (2.12),

$$\epsilon' = \left( \frac{ct}{2L} \right)^2 \quad (2.13)$$

## 2.4.2 TDR system and measurement procedure

A TDR system comprises of six blocks: a pulse generator, a sampling oscilloscope, a sampler, coaxial cables, an impedance transformer or balun, and a sensor (See Fig. 2.8). A typical procedure of operation is as following: A fast rise ramp or impulse, usually a few tens of picoseconds rise time, is delivered by a matched generator. This incident ramp or impulse passes through the sampler. The oscilloscope displays and records the incident and reflected signal by sampling the signal passing through the sampler. The wave propagates along the transmission line and reaches the input of the sensor. If a mismatch exists at input of the sensor, a part of the incident wave will be reflected. At the end of the sensor, there is another impedance mismatch. This mismatch creates a second reflection. The reflected voltage wave will algebraically add to the incident wave, and can be displayed on the oscilloscope through the sampler (See Fig. 2.8). The time delay can be interpreted as the propagating velocity when the length of the sensor is known.

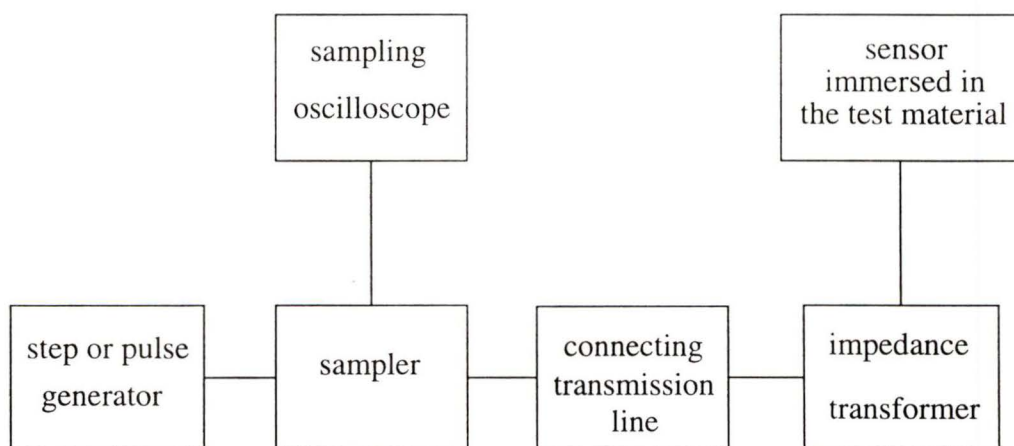


Figure 2.8 Block diagram of a typical TDR system.

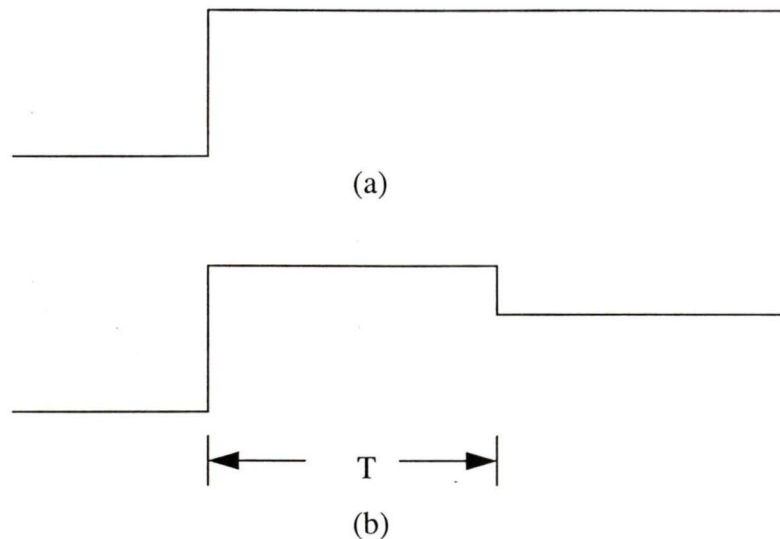


Figure 2.8 The waveforms displayed on the oscilloscope. (a) The displayed waveform when the reflected wave is zero; (b) The displayed waveform when the reflected wave is not zero.  $T$  is twice of propagating time from the sampler to the mismatch point.

## 2.5 TDR Application to Moisture Content Measurements

The time-domain reflectometry (TDR) technique for measurement of soil water content involves the propagation velocity measurement of a pulse while it travels along a sensor which holds or is immersed in soil. The technique has great potential for providing accurate, rapid and non-invasive soil water content measurements with high spatial resolution.

The sensor can be immersed in the porous materials or contain the material samples, e.g. coaxial line with sample packed between inner and outer conductors. There are two impedance discontinuities at the beginning and the end of the sensor, respectively. A part of incident wave will be reflected to the input and will be recorded by the oscilloscope through the sampler. The reflection points at the start and the end of the sensor can be readily identified on the display (See Fig. 2.9). So, the propagation time along the sensor can be determined, and therefore the average dielectric constant of the test substance.

With the measured dielectric constant and the empirical relation shown in Section 2.3.2, the volumetric moisture content is obtained.

To identify the propagation time between the start and the end of the sensor, it is necessary to know the accurate position on the TDR trace of the start point and the reflection point arising from the end of the line. In ideal situation, both reflections are sharp. However, in practical situation, as shown in Fig. 2.10 which is a typical TDR trace, we can see that is not so easy. The start point is readily identified. But the end point distributes over a range of time. The reason may be the dispersion of the pulse and penetration of the pulse field beyond the end of the transmission line. It may be also because soil is a dispersive dielectric.

A practical estimate of the end of the sensor has been developed. The method estimates the end of the transmission line from the intersection of two tangents to the line near the end as shown in Fig. 2.10 [1].

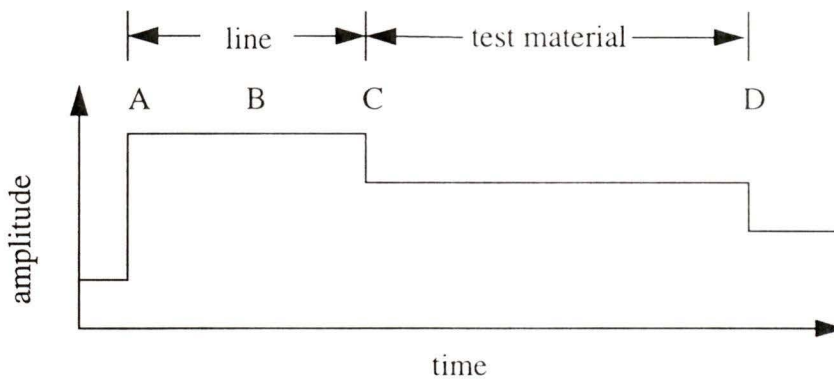


Figure 2.9 An idealized representation of the TDR measurement output on a soil sample; time interval C-D represents the travel time in the test substance.

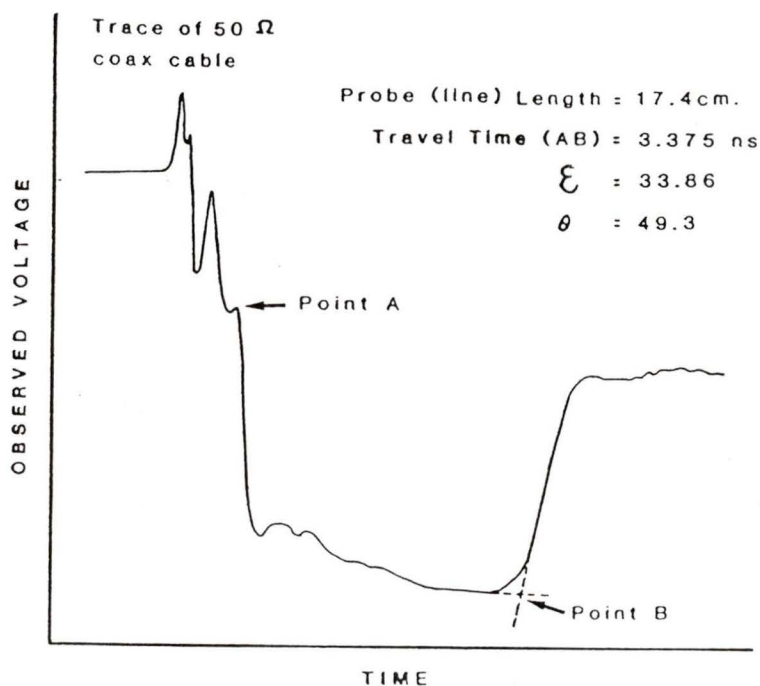


Figure 2.10 Typical TDR trace in a wet soil from parallel transmission lines with an open circuit at the end. Point A: start of parallel transmission lines; point B: end of parallel transmission lines [1].

The main advantage of the TDR technique is in that the measurement results are in some range independent of the loss factor and rely on the dielectric constant only, when the test substance is low loss. Another advantage of the TDR technique is the fact that the average water content along the length of the sensor can be measured. Other measurement methods, such as resonant method, due to non-uniform field distribution, has non-uniform sensitivity along the sensor so that the measurement results are affected by the position of the test substance. A third advantage is that the TDR technique is not sensitive to some characteristics of the test substance, for example, density and type of soil [4], while other microwave measurement methods have to keep the density the same during the measurement of the moisture content [11] [12].

## 2.6 TDR Sensors for Moisture Content Measurements

Several kinds of sensors have been designed to conduct moisture content measurements. They are divided into two categories: sensors used in the laboratory are usually sample containers, and those used in the field measurement usually can be inserted into the test substances (e.g. soil) easily. All sensors presently used have non-uniform sensitivity [16] [17].

### 2.6.1 Coaxial transmission line

Coaxial transmission line is used mainly in the laboratory as a sample holder [4]. The sample fills the space between the inner and outer conductors. This kind of sensor can be connected directly to the connecting line. However, because it is a closed configuration, it cannot be used *in situ*. The measurement sensitivity is high around the inner conductor and quite low near the outer conductor [16].

### 2.6.2 Two-rod parallel line

Another frequently used sensor is the two-rod line. This kind of sensor can be inserted into the soil. Its measurement region is open and this configuration is widely used in the *in situ* measurement. Because it is a balanced transmission line, a balun is needed to connect it to the standard transmission line, which is usually unbalanced (a coaxial cable).

### 2.6.3 Multi-rod sensors

Multi-rod transmission lines can be inserted into the soil to carry out *in situ* measurements. Because the geometry of the two-rod line differs from that of the coaxial cable connecting the sensor to other TDR devices, considerable signal and information losses occur at the coaxial cable and the sensor interface [15]. In an attempt to match the electrical characteristics a balancing transformer, or a balun, is used. However, this transformer can itself be a source of unwanted reflections and can cause difficulties in analyzing the TDR signal, particularly in saline soils. Such reflections can also cause serious problems

in analyzing the signals from short probes [15]. The coaxial transmission line does not need a balun, but it is unsuitable for *in situ* measurements. The multi-rod sensors which emulate coaxial transmission lines, eliminate the necessity for balancing transformers, and reduce spurious noise and reflections.

Three- and four-rod sensors are frequently used. The configurations of the three- and four-rod lines are illustrated in Fig. 2.11. The central rod is directly connected to the center conductor of the coaxial cable and two or three outer rods are connected to the cable's shield.

Actually, the two or three outer rods have similar function of the shield of the coaxial cable. Obviously, multi-rod sensors with more than three rods around the perimeter would more closely approximate a coaxial transmission line. According to the analysis [15], the TDR information derived from the three- and four-rod sensors closely approximate that of the coaxial transmission line.

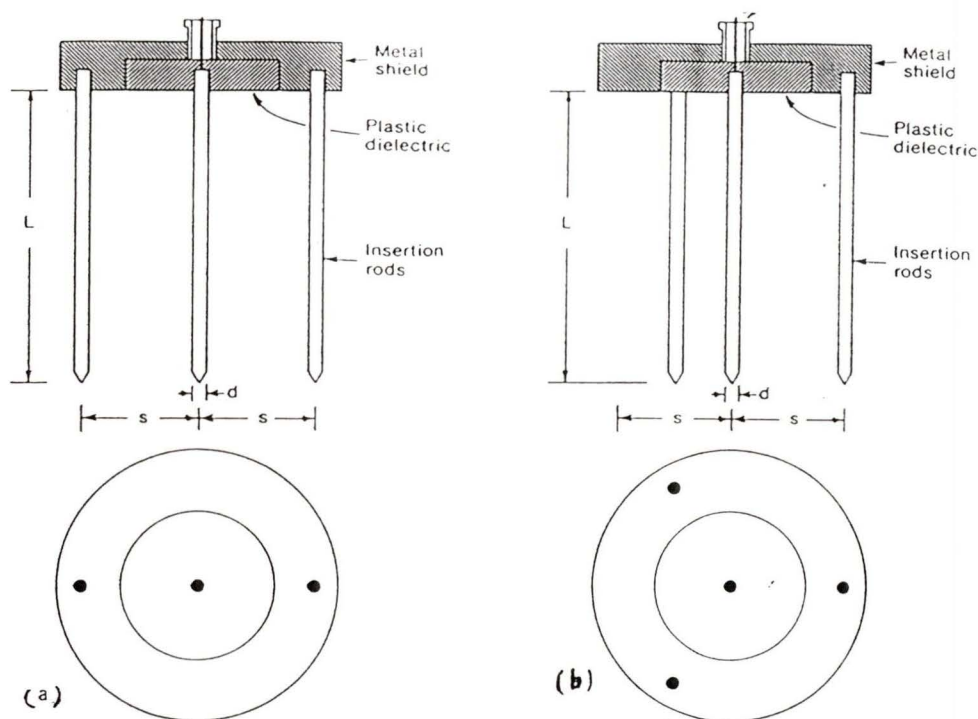


Figure 2.11 (a) Three-rod sensor; (b) Four-rod sensor. [15]

### 2.6.4 Remote shorting diode sensor

In practical TDR measurement systems which are used in field measurements, long connecting cables are usually necessary. The cables attenuate the signal, ultimately making measurements impractical [18]. The inhomogeneous properties of the soil also attenuate the reflection signal and produce high background noise, especially for heavy layered soil. The problems can be solved by using remotely switched shorting diode combined with differential detection technique (See Fig. 2.12) [18].

A bias is applied to the diode to get the short circuit and open circuit effects. When a forward bias is applied to the diode, the effective resistance is  $R_e=5 \Omega$ . When backward bias is added,  $R_e>10 \text{ k}\Omega$ . Typical characteristic impedance of the sensor (transmission line) is between 40 and 200  $\Omega$ . When the diode is forwardly biased, it is equivalent to a short circuit and when backwardly biased, it is almost an open circuit except for a small capacitance of 1 - 2 pF.

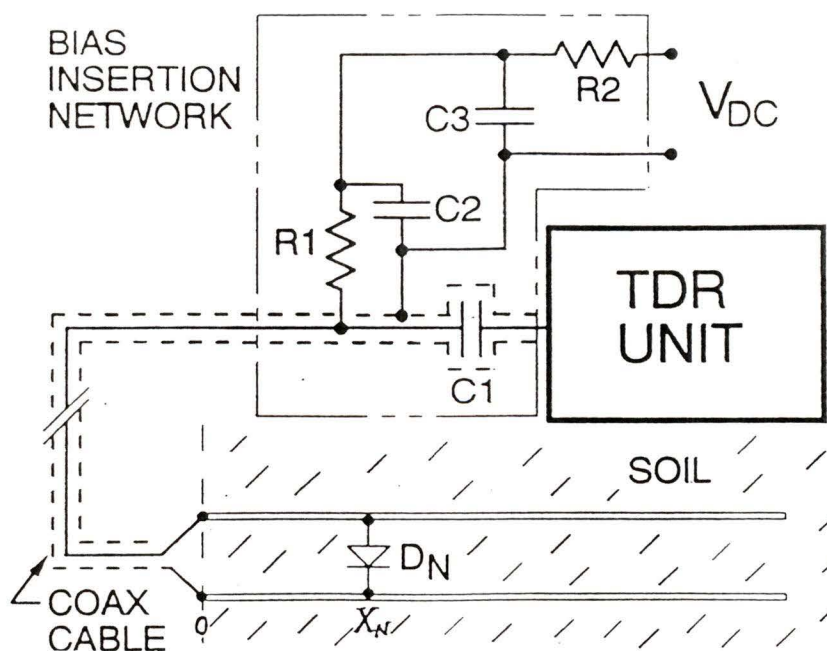


Figure 2.12 Remote shorting diode circuit [18].

A PIN diode is utilized as a switching diode (See Fig. 2.12). When the diode is short circuited, a strong negative reflection is created at  $X_N$ , when the diode is open circuited, the ramp or pulse signal is unaffected and continues propagating down the sensor. The reflected waveform obtained with diode shorted circuit is identical to that obtained with diode opened circuit until the time  $T_N$ . At this time, the reflection from the shorted diode reaches the sampling oscilloscope. Detection of  $T_N$  is best done by differential technique such as waveform subtraction. The difference waveform is zero at all times before  $T_N$ , and then rises sharply in a ramp (See Fig. 2.13).

In order to investigate the ability of the remote shorting diode technique to correctly measure  $T_2$  in heavy layered soil, a water box experiment was devised to simulate soil layers. The results showed a predictable time delay (See Fig. 2.14).

This technique allows the reliable, rapid and accurate measurement of the time delay. Multiple diodes can be used to measure the profile of water content in layered soil.

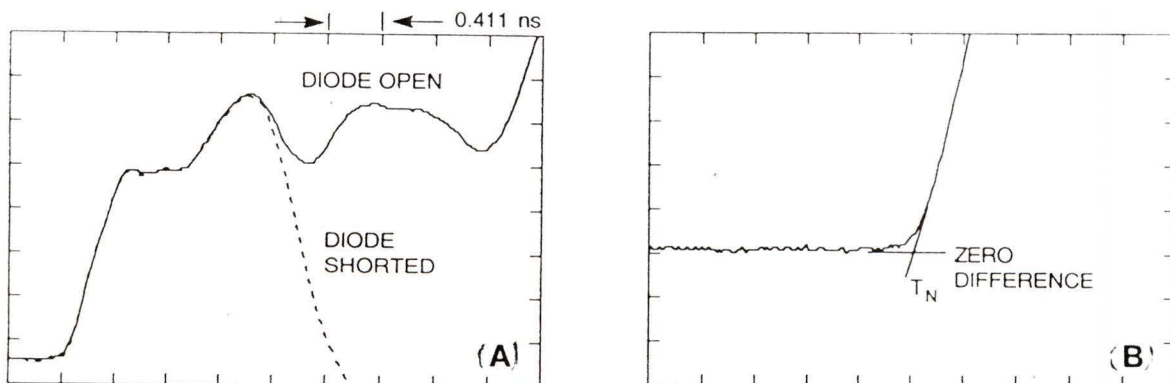


Figure 2.13 Waveforms generated from a one-diode probe. The diode is at the surface of the soil [18]. (a) Measured waveforms; (b) Subtraction result.

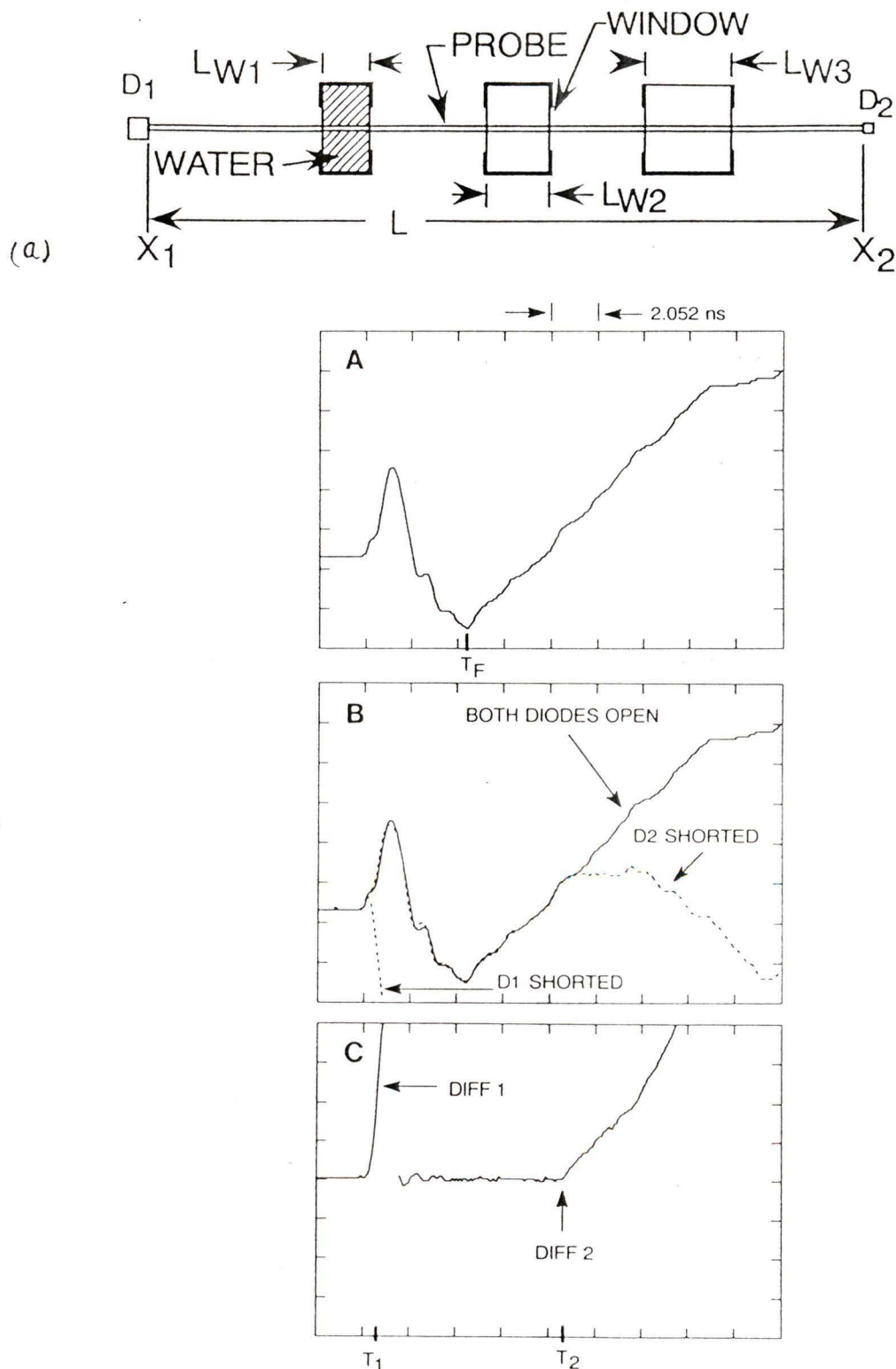


Figure 2.14 Water boxes used to simulate the interfering reflections found in layered soil. (a) Experiment configuration; (b) Experimental waveforms [18].

### 2.6.5 Other sensors

To obtain the profile of soil water content, the discontinuities of impedance of parallel rods by changing the diameter of the rod can be used to create additional reflections (See Fig. 2.15) [28].

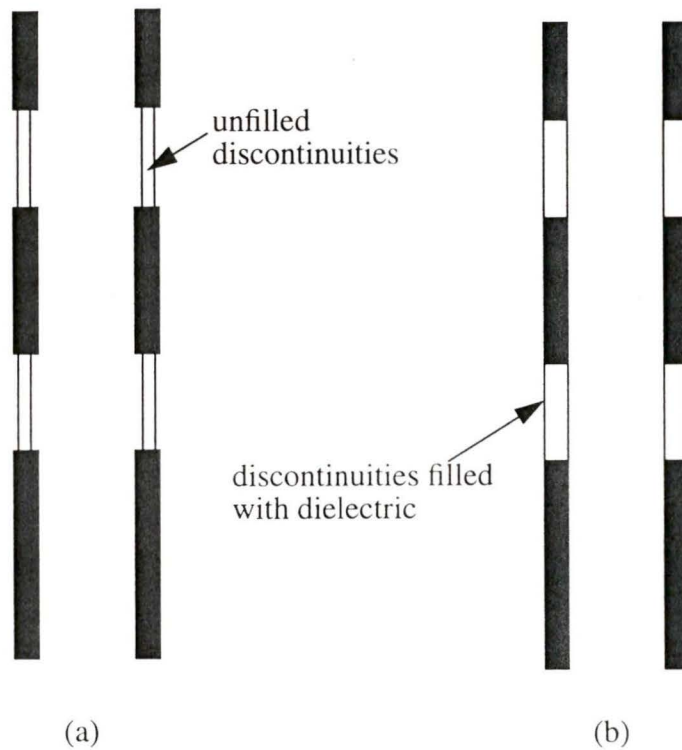


Figure 2.15 Configurations of the discontinued impedance transmission line. (a) transmission line with unfilled discontinuities; (b) transmission line with discontinuities filled with dielectric.

The impedance of the parallel transmission line is affected by the diameter and spacing of the rods [28]

$$Z = \frac{120}{\sqrt{\epsilon'}} \ln\left(\frac{2s}{d}\right) \quad (2.14)$$

where  $Z$  is the characteristic impedance of the line,  $\epsilon'$  is the dielectric constant,  $s$  is the center-to-center spacing between the rods, and  $d$  is the diameter of the rod. From (2.14), by varying the diameter of the rods at specified locations we can obtain impedance discontinuities at known locations along the line. Each of the discontinuities causes a reflection which can be used to determine the water content profiles between two discontinuities. As shown in Fig. 2.15(b), the locations of reduced diameters are filled with a nonporous material having a known dielectric constant. The outer diameter of this material is the same as the rods. This configuration can avoid air gaps at the discontinuities.

## Chapter 3

### Analysis of Sensors

In this chapter, the properties of sensors are discussed. Ideally, the sensor should sample over a known volume with the same weighing function through out it, so that the physical locations of material inhomogeneities do not significantly affect measurement results. This is related to the problem of sensor's sensitivity, which is discussed in detail in this chapter in order to determine the sensor's weighing function. The characteristic impedance of the sensor is also important when the match to the feeding line is considered. Another problem which is considered in this chapter is related to the propagation of the TDR pulses along the sensor immersed in the test substance.

#### 3.1 Analysis of TDR Sensors

##### 3.1.1 Spatial weighing function

Let us consider the spatial sensitivity of the sensor and assume that it is infinitely long and lossless. The measured dielectric constant  $\epsilon_m(\mathbf{x})$  is the convolution of the dielectric constant  $\epsilon(\mathbf{x})$  at a point  $\mathbf{x}=(x_1, x_2, x_3)$  and the weighing function of the sensor is  $w(\mathbf{x})$  [16]:

$$\epsilon_m(\hat{\mathbf{x}}) = \int_v \epsilon(x'_1, x'_2, x'_3) w(x_1 - x'_1, x_2 - x'_2, x_3 - x'_3) dx'_1 dx'_2 dx'_3 \quad (3.1)$$

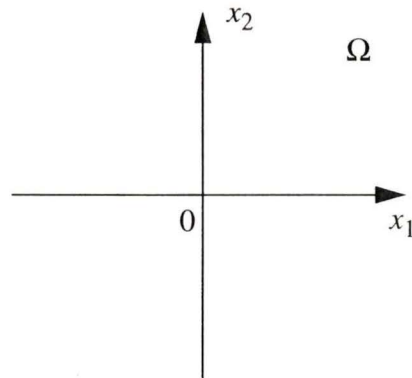


Figure 3.1 The configuration of the coordinate axes  $(x_1, x_2)$  on the plane  $\Omega$

Let  $x_3$  be the direction parallel to the electrode axis. Then, the sensitivity of measurement is independent of  $x_3$  and only the two-dimensional pattern on the plane  $\Omega$  is considered. So, (3.1) becomes

$$\varepsilon_m(\hat{x}) = \int_{\Omega} \varepsilon(x'_1, x'_2, x'_3) w(x_1 - x'_1, x_2 - x'_2) dx'_1 dx'_2 \quad (3.2)$$

The weighing function can be solved by Laplace's equation:  $\nabla^2 \Phi = 0$  and  $\mathbf{E} = -\nabla \Phi$  [16],

$$w(x_1, x_2) = \frac{|\hat{\mathbf{E}}(x_1, x_2)|^2}{\iint_{\Omega} |\hat{\mathbf{E}}_0|^2 dA} \quad (3.3)$$

where  $\mathbf{E}(x_1, x_2)$  is the electric field distribution at point  $(x_1, x_2)$  and  $\mathbf{E}_0$  is the electric field when the dielectric constant is constant.  $\Omega$  denotes the area the sensor measures and  $dA$  is an elementary area of plane  $\Omega$

If  $\mathbf{E}(x_1, x_2) = \mathbf{E}_0$  is constant, the weighing function  $w(x_1, x_2)$  is constant through out the measurement area. Therefore, the measured dielectric constant  $\varepsilon_m$  depends linearly

on  $\epsilon(x_1, x_2)$ . If the field  $\mathbf{E}(x_1, x_2)$  is non-uniform, since  $w$  depends on  $\mathbf{E}$ , which in turn depends on  $\epsilon(x_1, x_2)$ , the weighing function itself depends on  $\epsilon$ . Therefore, the dependence of  $\epsilon_m$  on the distribution of  $\epsilon$  is complicated and non-linear. Under perturbation assumption, with the non-uniformities of  $\epsilon$  small,  $\epsilon_m$  depends nearly linearly on  $\epsilon$  [16]. To the first-order accuracy, the contribution of the non-uniform perturbation in  $\epsilon$  to the field distribution, and hence to the spatial weighing function, can be ignored. The approximate weighing function  $w_0(\mathbf{x})$  is [16]

$$w_0(x_1, x_2) = \frac{|\vec{E}_0(x_1, x_2)|^2}{\iint_{\Omega} |\vec{E}_0|^2 dA} \quad (3.4)$$

satisfying

$$\epsilon_m(\hat{x}) = \int_{\Omega} \epsilon(x'_1, x'_2, x'_3) w_0(x_1 - x'_1, x_2 - x'_2) dx'_1 dx'_2 \quad (3.5)$$

From (3.4), we can see that  $w_0(x_1, x_2)$  is the normalized electrostatic energy density for uniform dielectric constant. (3.5) can be applied to various configurations.

### 3.1.2 Spatial weighing functions of sensors

#### 3.1.2.1 Coaxial transmission line

The weighing function of the coaxial line can be obtained by solving Laplace's equation. Assume that the coaxial line has the inner and outer radii of  $r_1$  and  $r_2$  and electric potentials of zero and unity, respectively. Without loss of generality, the solution is [16]

$$|\vec{E}_0|^2 = [\ln(r_2/r_1)]^{-2} r^{-2} \quad (3.6)$$

and from (3.4), we get [16]

$$w_0(r, \varphi) = [2\pi \ln(r_2/r_1)]^{-1} r^{-2} \quad (3.7)$$

This is the normalized weighing function, satisfying

$$\int_0^{2\pi} \int_{r_1}^{r_2} w_0(r, \varphi) r dr d\varphi = 1 \quad (3.8)$$

From (3.7), we can see, first, the contours of the weighing function on the cross section plane are concentric circles; second, there is a singularity at  $r=0$  so that most of the energy and hence most of the sensitivity is concentrated in a small cylinder around the inner electrode; third, the median radius  $r_m$  with half energy between  $r_1$  and  $r_m$  satisfies

$$r_m/r_2 = (r_1/r_2)^{1/2} \quad (3.9)$$

That means the volume per unit length in which half of the total energy is concentrated is proportional to the square root of the ratio of the inner and outer radius.

### 3.1.2.2 Two parallel rods

The parameters of the sensor are: the radius of the rods  $b$  and the distance between them  $2d$  (See Fig. 3.2).

Knight [16] analyzed this kind of sensor by using a bipolar coordinate system. The normalized weighing function depends on parameters  $b$  and  $d$ . The contours near either rod are concentric circles similar to the coaxial line. Far away from the rods, the contours approach circles with centers at  $(0, 0)$  (See Fig. 3.3).

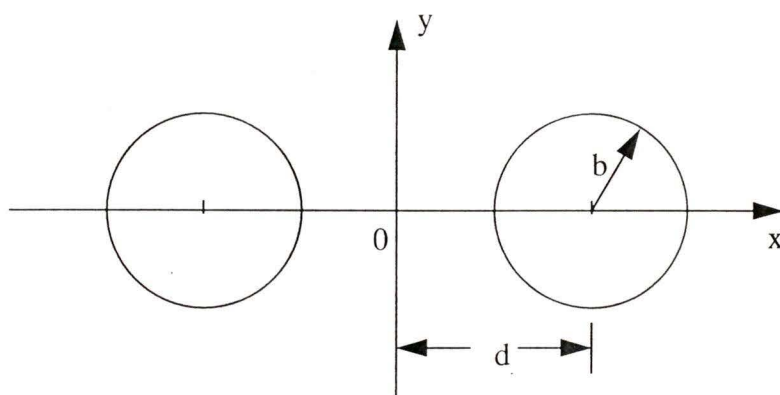


Figure 3.2 Two parallel-rod sensor.

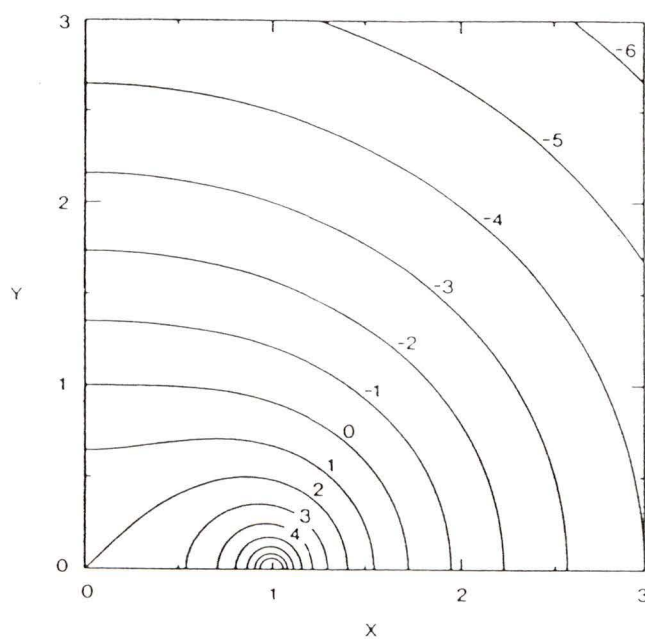


Figure 3.3 Contour of the relative spatial sensitivity function for two parallel-rod sensor in the first quadrant of the plane [16]. The number  $n$  on the contour indicates a level of  $2^n$ .

From the analysis shown in [16], the sensitivity depends on the ratio  $b/d$ . If  $b/d$  is small, say  $b/d < 0.1$ , the sensitivity is concentrated around the rods. The so called “cylinder of influence” is different for different  $b/d$ .

## 3.2 Characteristic Impedance of Sensors

In order to prevent signal from losses (reflections) the sensor should be matched to the feeding transmission line. The characteristic impedance is, therefore, a design parameter of the sensor. In this section, the calculations of the characteristic impedance of different sensors are presented.

### 3.2.1 Characteristic impedance of TEM transmission lines

For a lossless TEM transmission line, the characteristic impedance  $Z_0$ , in terms of the inductance per unit length  $L$  and the capacitance per unit length  $C$ , is:

$$Z_0 = \sqrt{\frac{L}{C}} \quad (3.10)$$

With the propagation velocity,

$$v = \frac{1}{\sqrt{LC}} = \frac{1}{\sqrt{\epsilon\mu}} \quad (3.11)$$

and with the charge per unit length  $Q=C \cdot U$ , (3.10) becomes:

$$Z_0 = \frac{\sqrt{\epsilon\mu}}{C} = \frac{\sqrt{\epsilon\mu}}{Q} U \quad (3.12)$$

Then, the calculation of the characteristic impedance of a lossless TEM transmission line is reduced to the calculation of the capacitance per unit length, i.e., an electrostatic problem. The capacitance per unit length of the transmission line can be calculated using numerical methods, such as Finite Difference or Finite Element methods.

### 3.2.2 Characteristic impedance of parallel plates

The characteristic impedance of some simple transmission lines can be calculated analytically. For the parallel-plate transmission line, the exact characteristic impedance calculation has been carried out. However, the solution is unwieldy and two useful approximations for narrow and broad strips, i.e., for  $b \ll d$  and  $b \gg d$  have been used. The characteristic impedance can be approximated by [29]:

1. broad strips:  $0 \leq Z_0/\eta \leq 0.7$  (See Fig. 3.5)

$$\frac{d}{b} = \frac{\pi}{\frac{\pi\eta}{Z_0} - \ln 2 - \ln\left(\frac{\pi\eta}{Z_0} - \ln 2\right) - 1} \quad (3.13)$$

2. narrow strips:  $0.7 \leq Z_0/\eta \leq \infty$

$$\frac{d}{b} = \frac{1}{4} e^{Z_0\pi/\eta} \quad (3.14)$$

To match the sensor to the connecting cable, the characteristic impedance should be  $Z_0=50 \Omega$  and since  $\eta=377 \Omega$  in air,  $Z_0/\eta=0.133 < 0.7$ , the broad strips' formula is applicable. Substituting  $Z_0$  and  $\eta$  in (3.13), we get  $d/b=0.167$ . A 1:4 impedance matching balun can also be used to connect the sensor. The characteristic impedance of the sensor, therefore, can be  $Z_0=200 \Omega$ . And  $Z_0/\eta=0.53 < 0.7$ . The broad strips' formula is also applicable. The dimension factor is  $d/b=1.22$ . From the practical point of view which includes the measurement volume and the convenience of insertion into the soil, the latter sensor with impedance  $200 \Omega$  is advantageous.

For complex shape sensors, analytical formulae are not available. The numerical methods can be used to carry out the calculation.

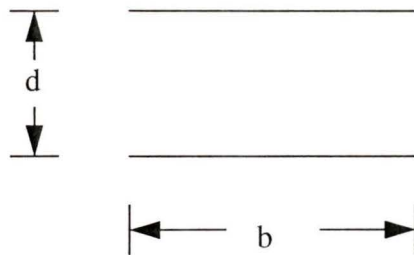


Figure 3.4 Configuration of the parallel strip line.

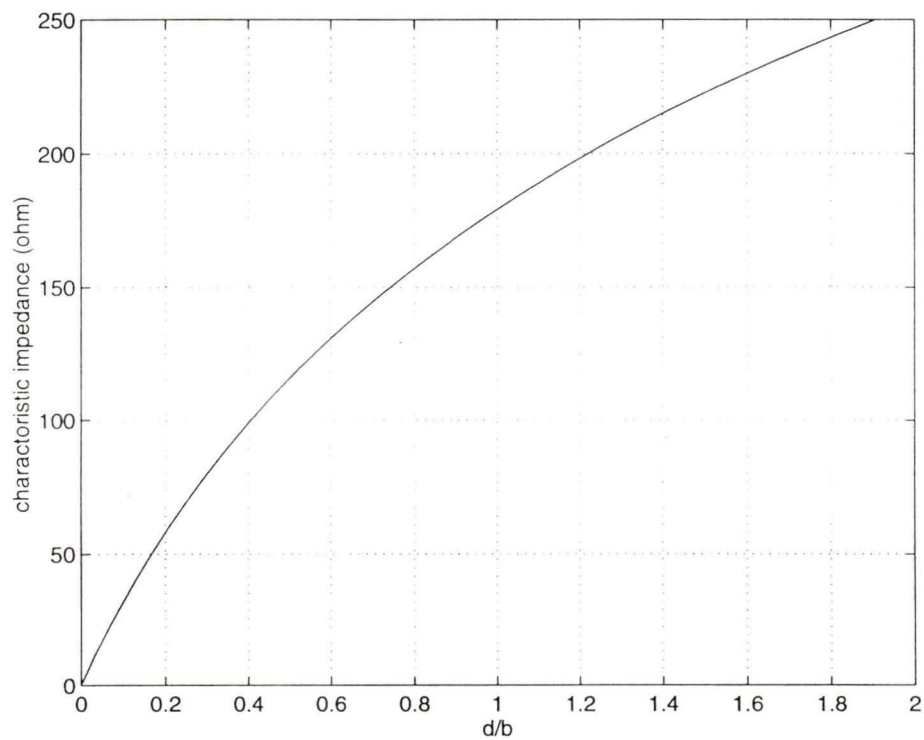


Figure 3.5 The impedance vs. dimension parameter for broad strips.

### 3.3 Pulse Propagation in Porous Media

In order to correctly interpret the wave shapes of the TDR display, a model of pulse propagation in porous media is desirable. We will discuss the Finite Difference Time Domain (FDTD) method for solution of the Time Domain Maxwell's equations in the Debye media [10].

#### 3.3.1 Debye relation of permittivity

Debye relation can be obtained by measuring the step response of the orientation polarization. The polar molecules turn and exponentially approach the final states of polarization with a time constant  $\tau_0$ , which is called the relaxation time. Deriving a formula for the permittivity as a function of frequency is done by applying the Fourier transform to the step response. Debye relation for the polar substance is:

$$\varepsilon = \varepsilon_{\infty} + \frac{\varepsilon_0 - \varepsilon_{\infty}}{1 + j\tau_0\omega} \quad (3.15)$$

where  $\varepsilon_0$  is the permittivity at low frequencies, where orientation polarization has enough time to fully develop, and  $\varepsilon_{\infty}$  is the permittivity at high frequencies, where orientation polarization has not developed. The values of the constants in (3.15) are difficult to calculate theoretically, and for practical purposes, are obtained empirically. The frequency dependence of the permittivity of a polar material, as given in Debye relation, is shown in Fig. 3.6. The dielectric constant is constant at low and high frequencies, and the transition occurs slowly in the vicinity of the relaxation frequency  $f_{rel}=1/(2\pi\tau_0)$ . The loss factor is small at both low and high frequencies and large only in the transition region.

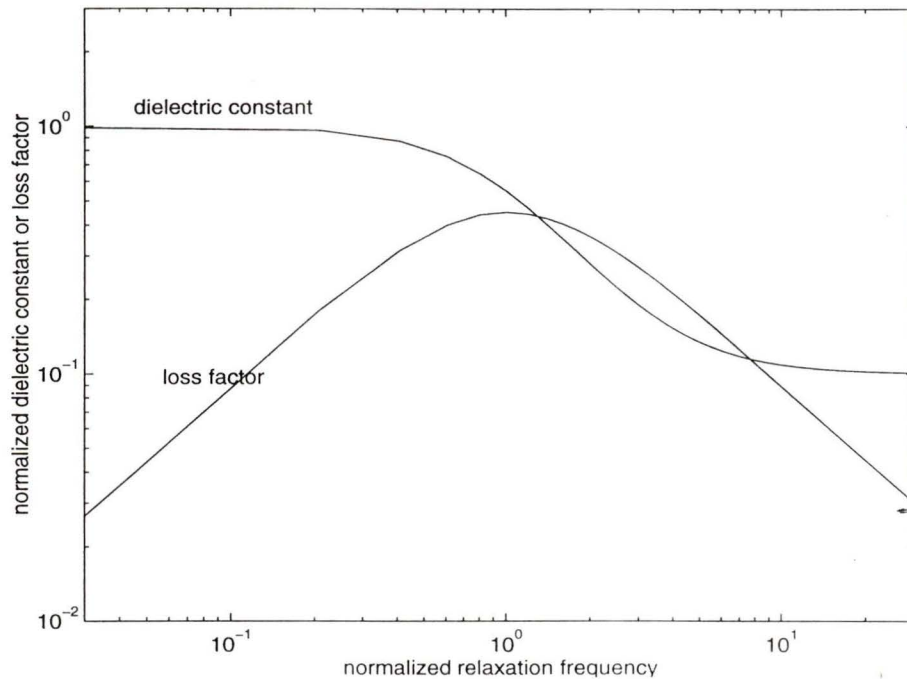


Figure 3.6 Frequency dependence of the permittivity according to Debye relation  
 $(f_{rel} = \omega/2\pi = 1/2\pi\tau_0)$

At the relaxation frequency, the loss factor reaches the maximum value:

$$\varepsilon''_{max} = \frac{\varepsilon_0 - \varepsilon_\infty}{2} \quad (3.16)$$

Debye relation contains three constants,  $\varepsilon_0$ ,  $\varepsilon_\infty$ , and  $\tau_0$ . The high frequency dielectric constant is due to electronic and atomic polarization, and is therefore, independent of temperature. The other two constants are affected by the thermal agitation. The low frequency dielectric constant decreases with rising temperature because of the increasing disorder. The relaxation time,  $\tau_0$ , is inversely proportional to temperature, due to the fact that all movements are faster at higher temperature.

### 3.3.2 Time Domain Maxwell's equations in Debye medium

Source-free Time Domain Maxwell's equations are [10]:

$$\nabla \times \vec{E}(x, y, z, t) = -\frac{\partial \vec{B}(x, y, z, t)}{\partial t} \quad (3.17)$$

$$\nabla \times \vec{H}(x, y, z, t) = \frac{\partial \vec{D}(x, y, z, t)}{\partial t} + \sigma \vec{E}(x, y, z, t) \quad (3.18)$$

where  $\vec{B}(t)$  and  $\vec{D}(t)$  can be obtained by the inverse Fourier transforms of the correspondents in frequency domain:

$$\vec{B}(\omega) = \mu^*(\omega) \vec{H}(\omega) \quad (3.19)$$

$$\vec{D}(\omega) = \varepsilon^*(\omega) \vec{E}(\omega) \quad (3.20)$$

The medium is assumed homogeneous and isotropic. The permeability is that of free space,  $\mu_0$ . The conductivity,  $\sigma$ , is constant. The permittivity is assumed to be Debye model:

$$\varepsilon^*(\omega) = \varepsilon_\infty + \frac{\varepsilon_0 - \varepsilon_\infty}{1 + j\tau_0\omega} \quad (3.21)$$

We obtain  $\vec{B}(t)$ ,  $\vec{D}(t)$ , and  $\varepsilon(t)$  from the inverse Fourier transform of (3.19), (3.20), and (3.21) [10]:

$$\vec{B}(t) = \mu_0 \vec{H}(t) \quad (3.22)$$

$$\vec{D}(t) = \int_{-\infty}^{\infty} \varepsilon(t-\beta) \vec{E}(\beta) d\beta \quad (3.23)$$

$$\varepsilon(t) = \varepsilon_\infty \delta(t) + \frac{\varepsilon_0 - \varepsilon_\infty}{\tau_0} e^{-t/\tau_0} u(t) \quad (3.24)$$

Applying (3.24) to (3.23), we get [10]:

$$\vec{D}(t) = \epsilon_{\infty} \vec{E}(t) + \frac{\epsilon_0 - \epsilon_{\infty}}{\tau_0} \int_{-\infty}^{\infty} e^{-(t-\beta)/\tau_0} u(t-\beta) \vec{E}(\beta) d\beta \quad (3.25)$$

For one-dimensional problem, we assume that the incident plane wave irradiates in the dispersive dielectric in  $z$ -direction with normal to the air/dielectric interface. Then [10],

$$D_x(t) = \epsilon_{\infty} E_x(t) + \frac{\epsilon_0 - \epsilon_{\infty}}{\tau_0} \int_{-\infty}^{\infty} e^{-(t-\beta)/\tau_0} u(t-\beta) E_x(\beta) d\beta \quad (3.26)$$

By differentiating above equation with respect to  $t$ , we obtain the first and second derivative of  $D_x(t)$  [10]:

$$\frac{\partial D_x(t)}{\partial t} = \epsilon_{\infty} \frac{\partial E_x(t)}{\partial t} + \frac{\epsilon_0 - \epsilon_{\infty}}{\tau_0} \left[ E_x(t) - \frac{\Delta t}{\tau_0} S_x(t) \right] \quad (3.27)$$

$$\frac{\partial^2 D_x(t)}{\partial t^2} = \epsilon_{\infty} \frac{\partial^2 E_x(t)}{\partial t^2} + \frac{\epsilon_0 - \epsilon_{\infty}}{\tau_0} \left[ \frac{\partial E_x(t)}{\partial t} - \frac{1}{\tau_0} E_x(t) + \frac{\Delta t}{\tau_0} S_x(t) \right] \quad (3.28)$$

where

$$S_x(t) = \frac{1}{\Delta t} \int_{-\infty}^{\infty} e^{-(t-\beta)/\tau_0} u(t-\beta) E_x(\beta) d\beta \quad (3.29)$$

and  $\Delta t$  is the time increment.  $S_x(t)$  can be reduced to the recursive form [10]:

$$S_x(t) = e^{-t/\tau_0} S_x(t-\Delta t) + \frac{1}{2} \left[ e^{-t/\tau_0} E_x(t-\Delta t) + E_x(t) \right] \quad (3.30)$$

### 3.3.3 FDTD implementation of Maxwell's equations

By manipulating one-dimensional time domain Maxwell's equations and applying (3.28) and (3.30) to the equations, we obtain [10]:

$$\frac{\partial^2 E_x(z, t)}{\partial t^2} = c_\infty^2 \frac{\partial^2 E_x(z, t)}{\partial z^2} - \left( \frac{\sigma}{\epsilon_\infty} + a\omega_0 \right) \frac{\partial E_x(z, t)}{\partial t} + a\omega_0^2 E_x(z, t) - a\omega_0^3 \Delta t S_x(z, t) \quad (3.31)$$

where

$$a = \frac{\epsilon_0 - \epsilon_\infty}{\epsilon_\infty} \quad (3.32)$$

$$\omega_0 = \frac{1}{\tau_0} \quad (3.33)$$

$$c_\infty = \frac{1}{\sqrt{\mu_0 \epsilon_\infty}} \quad (3.34)$$

We discretize (3.31) into finite difference form [10],

$$\alpha E_x^{n+1}(i) = -\beta E_x^{n-1}(i) + \left( \frac{c_\infty \Delta t}{\Delta z} \right)^2 [E_x^n(i+1) - 2E_x^n(i) + E_x^n(i-1)] \quad (3.35)$$

$$+ 2E_x^n(i) + a(\omega_0 \Delta t)^2 E_x^n(i) - a(\omega_0 \Delta t)^3 S_x^n(i)$$

where  $\Delta t$  is the time increment,  $\Delta z$  is the space increment, and

$$\alpha = 1 + \frac{\Delta t}{2} \left( \frac{\sigma}{\epsilon_\infty} + a\omega_0 \right) \quad (3.36)$$

$$\beta = 1 - \frac{\Delta t}{2} \left( \frac{\sigma}{\epsilon_\infty} + a\omega_0 \right) \quad (3.37)$$

For stability, the following condition must be satisfied:

$$\Delta z \leq c_{\infty} \Delta t$$

To simplify the formulae, reduce the number of time steps and obtain exact solution without truncation error, we choose [10]

$$\Delta z = c_{\infty} \Delta t$$

For the far-end boundary, the calculation can be terminated at the point [10]:

$$I_{END} \geq I_{obs} + \frac{N - I_{obs}}{2} + 1$$

where  $I_{END}$  is the truncation point,  $I_{obs}$  is the observation point, and  $N$  is the number of time steps to be calculated. This absorbing boundary condition assures the backscattering signal originating at the truncation point does not reach the observation point.

# Chapter 4

## Numerical Results

In this chapter, two topics are discussed. First, the results for sensors with uniform sensitivities are presented. Several sensors are proposed and their field distributions and sensitivities are calculated.

Second, the pulse propagation in water and soil is calculated using FDTD method to simulate the sensors' performance.

### 4.1 Sensitivity of Sensors

Typical TDR sensors, such as coaxial line and two or three conductor lines, produce a highly non-uniform electric field distribution, which is mostly concentrated close to the conductors as shown in Section 3.1.2. This means that the sensor measures only a very limit volume. Ideally, the sensor is required to sample over a known volume with the same weighing factor through out the volume, so that the locations of dielectric inhomogeneities do not affect measurement results.

Several sensors with different cross-sections were proposed and analyzed in order not only to increase the measurement volume but also to produce a uniform distribution of the electric field within that volume. This analysis was conducted using the Finite Element method which gives a quasi-static approximation of the electric field [30].

### 4.1.1 Parallel-plate sensor

The cross-section of the parallel-plate sensor is shown in Fig. 4.1. The coordinate system is erected as shown in order to take advantage of symmetry. The half width of the plate is set to 1 and the coordinates of  $y$ -axis of two electrodes are arbitrary  $a$  and  $-a$ . As a balanced transmission line, the electric potentials of two electrodes are set to  $+1V$  and  $-1V$ , respectively.

The idea of using parallel-plate line as a sensor is in the fact that it has uniform field distribution between two electrodes. The uniform field area is near the central region between two electrodes (See Fig. 4.2 and Fig. 4.3). This is the simplest configuration which has a uniform field area. However, due to the infinitely small curvature radius along the edge, the field strength is theoretically infinitely high at that point, and much higher than the uniform field area (See Fig. 4.3). Thus, the weighing function is also highly non-uniform. That means the response of the sensor to the inhomogeneous medium is much larger at the edge area than in the uniform area (See Fig. 4.4).

Although it is far from satisfactory, this sensor provides some clues on how to obtain uniform field distribution. Increasing the curvature radius at the edge of the electrodes can be expected to reduce the field strength in that area. We will discuss it later.

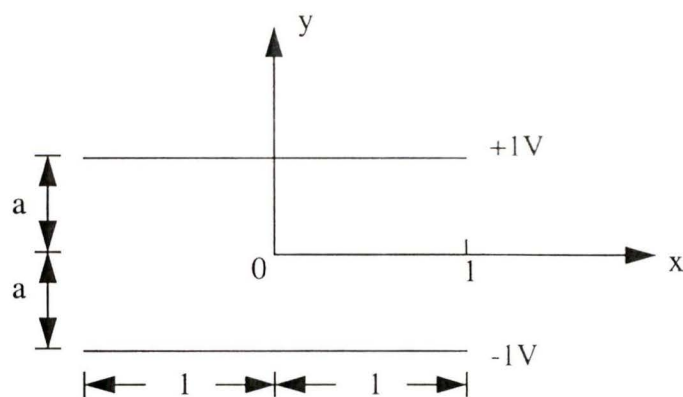


Figure 4.1 Configuration of the parallel-plate sensor and the selected coordinate system.

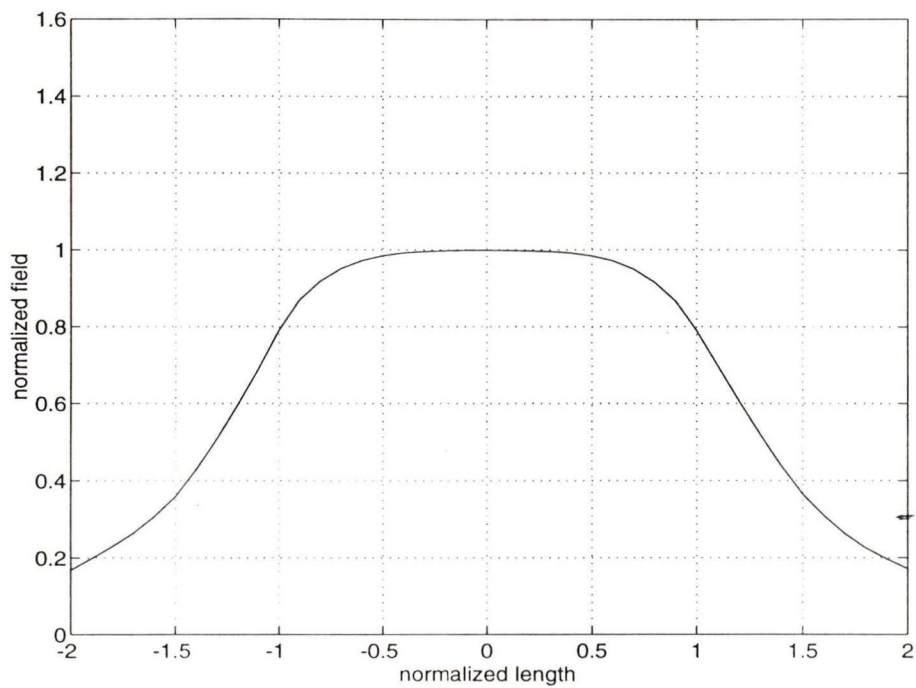


Figure 4.2 Field distribution along x-axis at  $y=0$  (center between two plates).

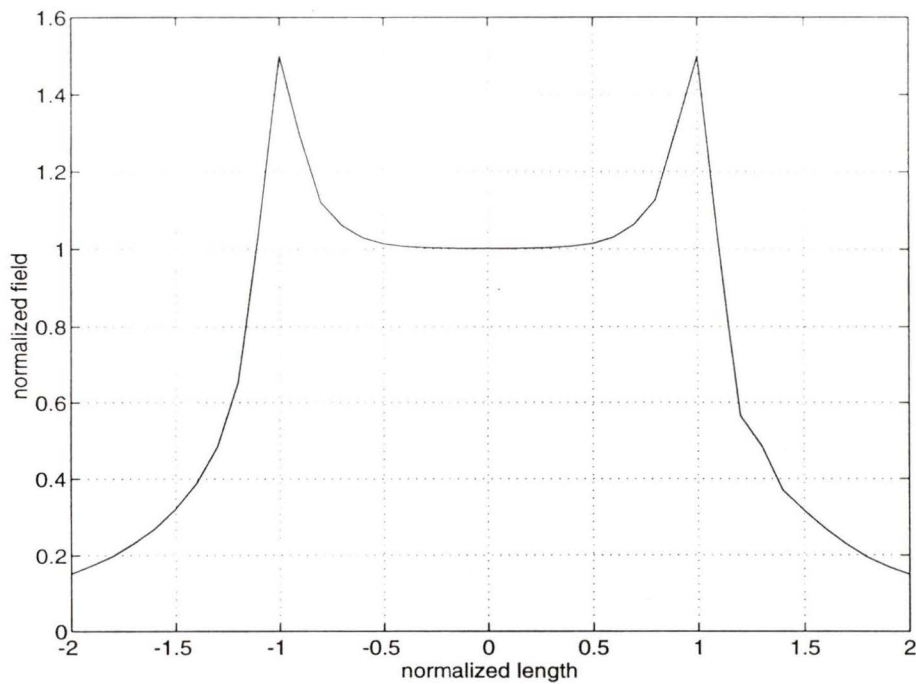


Figure 4.3 Field distribution along x-axis at  $y=a$  (on the surface of the plate).

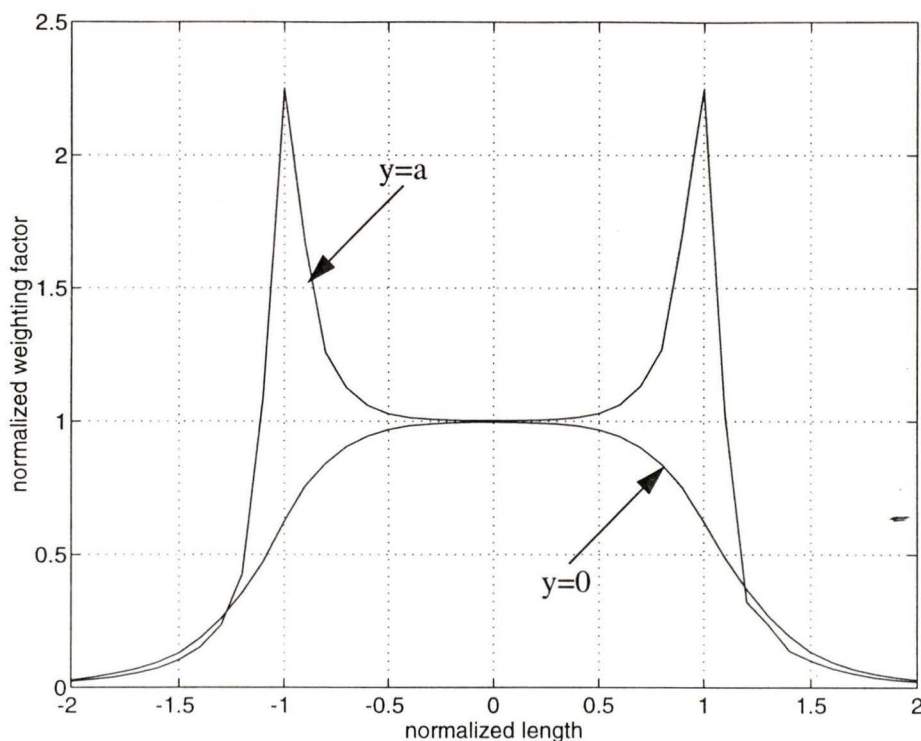


Figure 4.4 Weighing factor for parallel-plate line along x-axis at  $y=0$  and  $y=a$ .

### 4.1.2 Parallel-plate sensor with dielectric shield

To avoid the high field strength at the edge of the parallel-plate sensor described in Section 4.1.1, one straightforward method is to add a dielectric shield to the electrodes (plates). Suppose that the dielectric layer is Teflon which has the dielectric constant 2. We assume the electrodes are submerged in a medium with the dielectric constant 11 which is the typical soil's dielectric constant. The electrodes are wrapped in the shield. The shield's thickness is  $0.2a$  and it is a half circle with radius  $0.2a$  at the edge (See Fig. 4.5).

Calculation results are illustrated in Fig. 4.6, Fig. 4.7 and Fig. 4.8. The results show that there exists a high field strength in the dielectric shield (See Fig. 4.8). The greatest sensitivity appears in the shield (See Fig. 4.10). It has a desired effect on the field at the edge but cannot eliminate the high field strength completely (See Fig. 4.9).

The results are not fully satisfactory. First, the most sensitive region is in the shield which is meaningless for practical measurements. Second, when the dielectric constant of the measured medium changes, the field distribution changes so that the sensitivity of the sensor and the measurement calibration changes, too. That makes the measurement complicated.

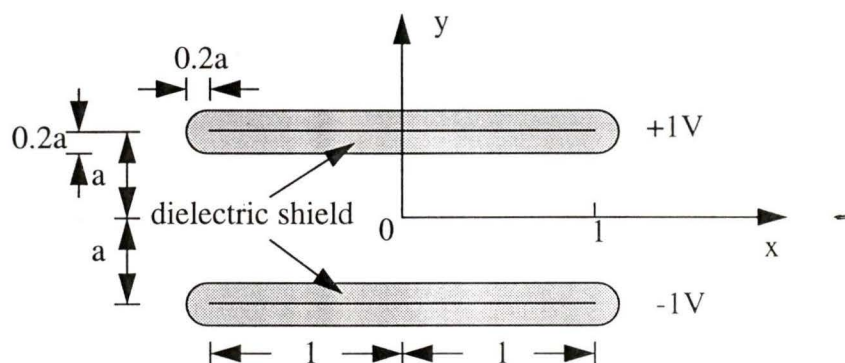


Figure 4.5 Configuration of the parallel-plate sensor with the dielectric shield.

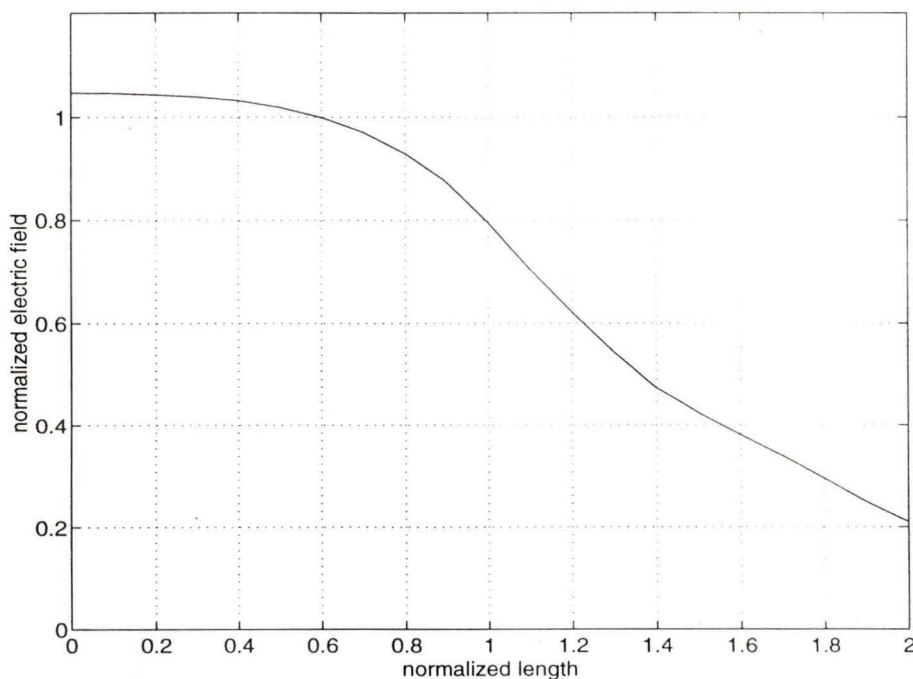


Figure 4.6 Field distribution along x-axis at  $y=0$  (at the center between the electrodes). The electric field is normalized to that of the parallel-plate sensor, and the widths is normalized to that of the parallel-plate sensor, too.

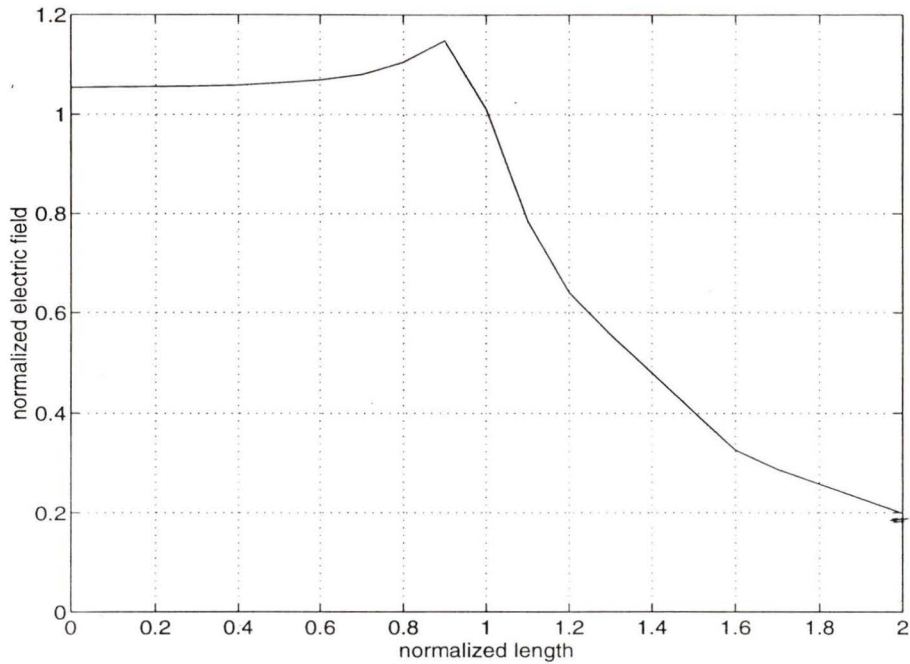


Figure 4.7 The field distribution along x-axis at  $y=0.8a$  (at the surface of dielectric shield). The electric field is normalized to that of the parallel-plate sensor, and the widths is normalized to that of the parallel-plate sensor, too.

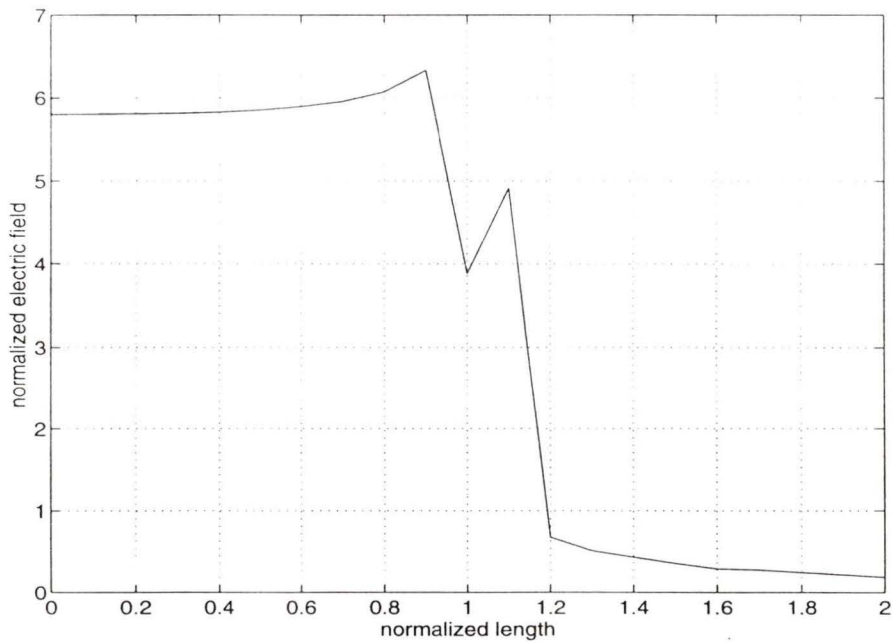


Figure 4.8 The field distribution along x-axis at  $y=a$  (at the electrode). The electric field is normalized to that of the parallel-plate sensor, and the width is normalized to that of the parallel-plate sensor, too.

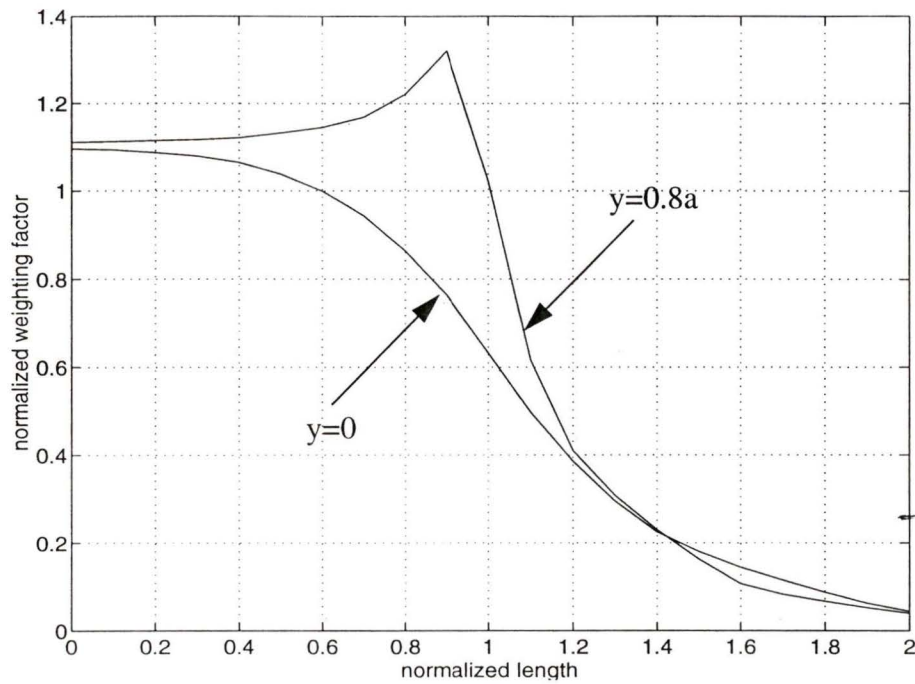


Figure 4.9 Weighing factor along x-axis at  $y=0$  and  $y=0.8a$ . The weighing factor is normalized to that of the parallel-plate sensor.

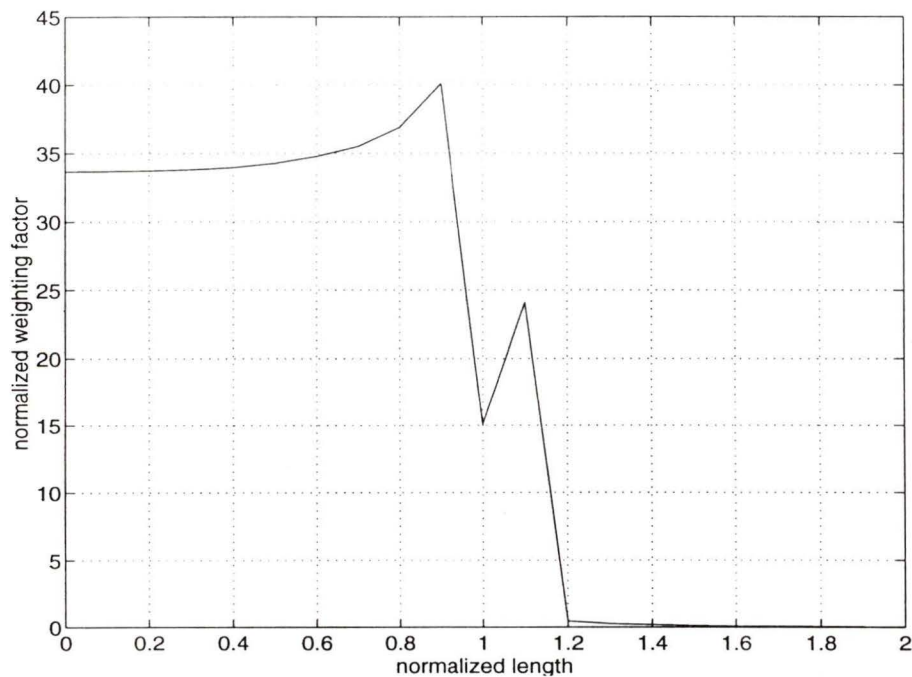


Figure 4.10 Weighing factor along x-axis at  $y=a$ . The weighing factor is normalized to that of the parallel-plate sensor.

### 4.1.3 Sensor with Rogowski's Profile

The Rogowski's profile is configured by the following relation [31]:

$$z = \frac{2a}{\pi} (w + 1 + e^w) \quad (4.1)$$

where  $z$  and  $w$  represent the complex coordinates in the  $z$ - and  $w$ -planes. Substitution of the coordinates for the complex values  $z=x+iy$  and  $w=u+iv$ , we get:

$$x = \frac{2a}{\pi} (u + 1 + e^u \cos v) \quad (4.2)$$

$$y = \frac{2a}{\pi} (v + e^u \sin v) \quad (4.3)$$

Consider two parallel plates in  $w$ -plane. In  $z$ -plane, the coordinates of these plates are given by  $v = \pm\pi$ , and other lines of  $v=\text{constant}$  with  $-\pi < v < +\pi$  are equipotential lines created by  $v = \pm\pi$  plate electrodes. All lines of  $u=\text{constant}$  with  $-\infty < u < +\infty$  indicate the directions of the electric field. All lines of  $v=\text{constant}$  with  $-\pi < v < +\pi$  are called *Rogowski's profile*. The lines appearing in the  $z$ -plane are shown in Fig. 4.11, showing the electric field distribution of parallel plates. The parallel plates terminate at  $x=0.677$ .

The field strength in the  $z$ -plane in terms of  $u$  and  $v$  is [31]:

$$|E| = \frac{V}{2a\sqrt{1 + e^{2u} + 2e^u \cos v}} \quad (4.4)$$

where  $V$  is the potential difference between two plates and  $2a$  is the half distance between the plates. In the normalized  $z$ -plane, we assume  $V=2V$  and  $a=1$ . So, the field strength becomes:

$$|E| = \frac{1}{\sqrt{1 + e^{2u} + 2e^u \cos v}} \quad (4.5)$$

The general condition for  $|E| \leq V/2a=1$  is given by  $\cos v \geq 0$  or  $v$  within  $\pm\pi/2$ . Rogowski has chosen the profile  $\cos v=0$  or  $v = \pi/2$ , the so-called *90° Rogowski's profile* [31]. Along this line the field strength has the maximum values between the plates in the

uniform field region  $u \leq -(3-5)$  and decreases gradually with the curvature increasing the value of  $u$ .

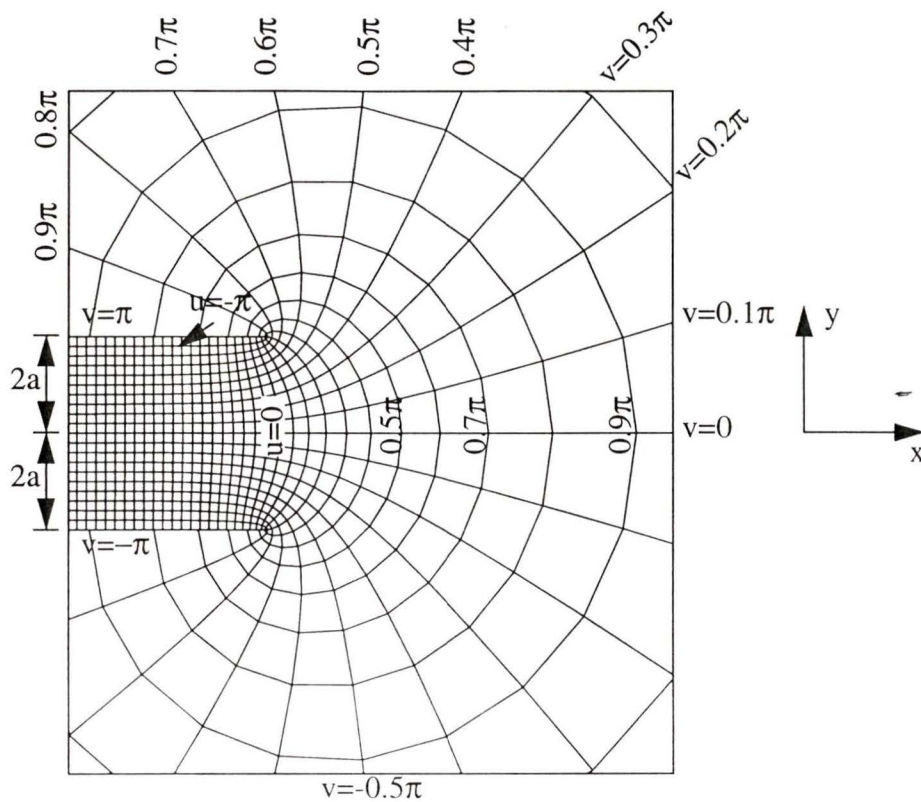


Figure 4.11 Rogowski's profile [31].

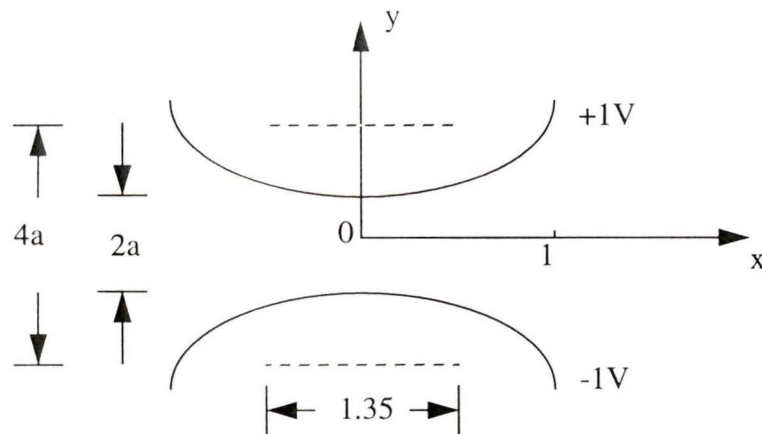


Figure 4.12 Configuration of the Rogowski's profile sensor. The half width of the electrode is normalized to 1. The width of parallel plates which can generate such a profile is 1.35.

The profile is infinitely wide. In actual situation, only a part of the profile is used as the electrodes (See Fig. 4.12). The half width of the part of the profile can be normalized to 1, when the width of  $v = \pi$  is 1.35. The calculation gives the consistent results with the theoretical analysis (See Fig. 4.13 and Fig. 4.14). The sensitivity distribution for this configuration is shown in Fig. 4.15.

Compared with parallel-plate sensor, Rogowski's profile solves the problem of high edge field. The field at the center is higher than in any other areas. However, the uniform field area is reduced. Not only the field along x-axis decreases gradually with the distance from center, but also the center field at  $y=0$  is not the same as that at electrodes  $y=a$  (See Fig. 4.15). Another problem is the "tail" of the field, i.e. the field strength decreases from a uniform level to a reasonably low level. It is also wider than for the parallel-plate sensor.

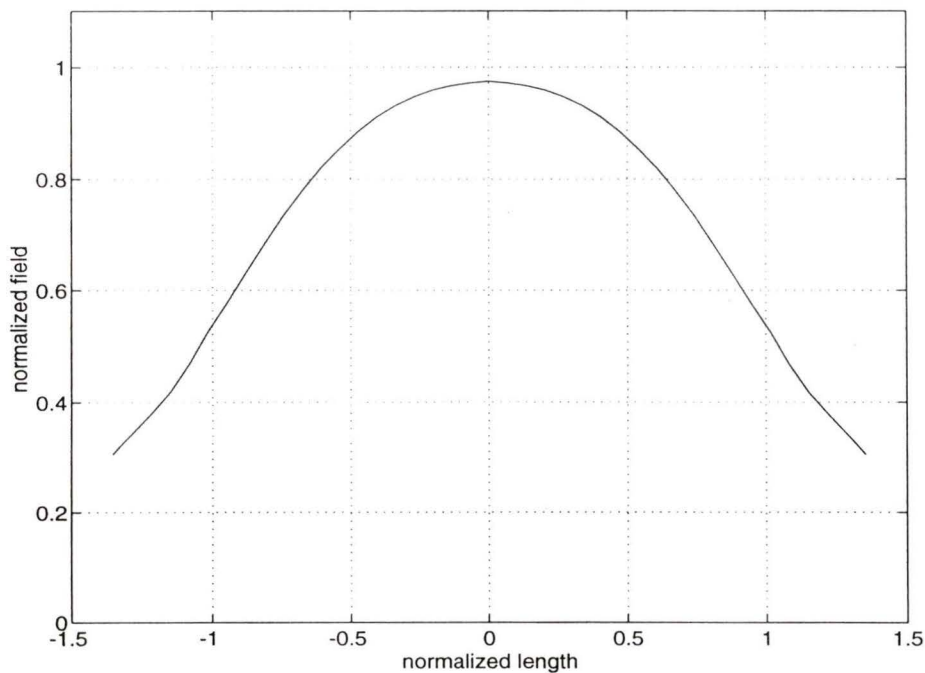


Figure 4.13 Field distribution for Rogowski's profile along x-axis at  $y=0$  (center between two electrodes).

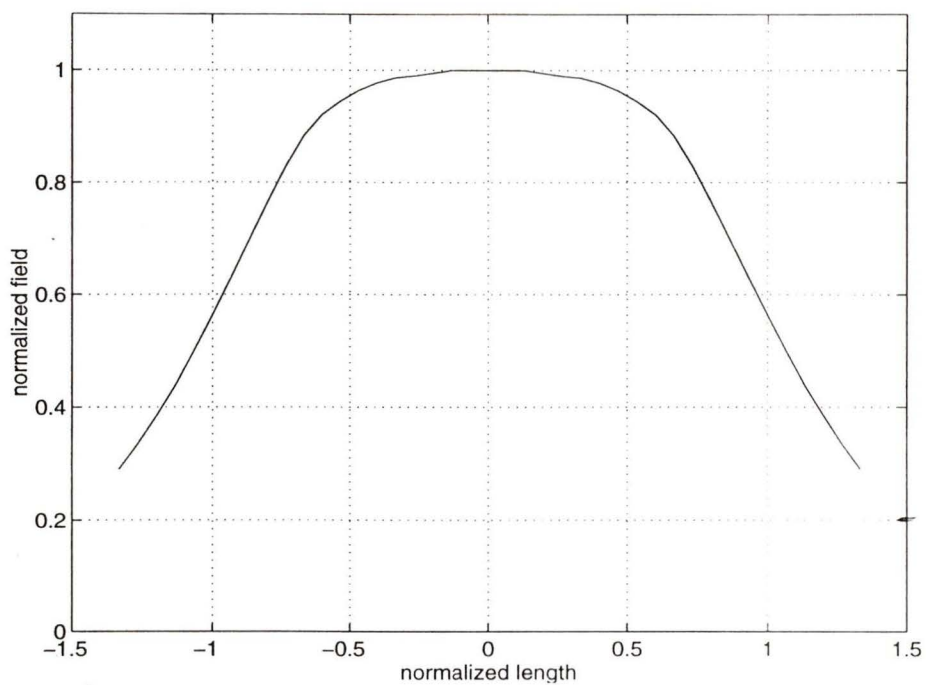


Figure 4.14 Field distribution for Rogowski's profile along x-axis at  $y=a$ .

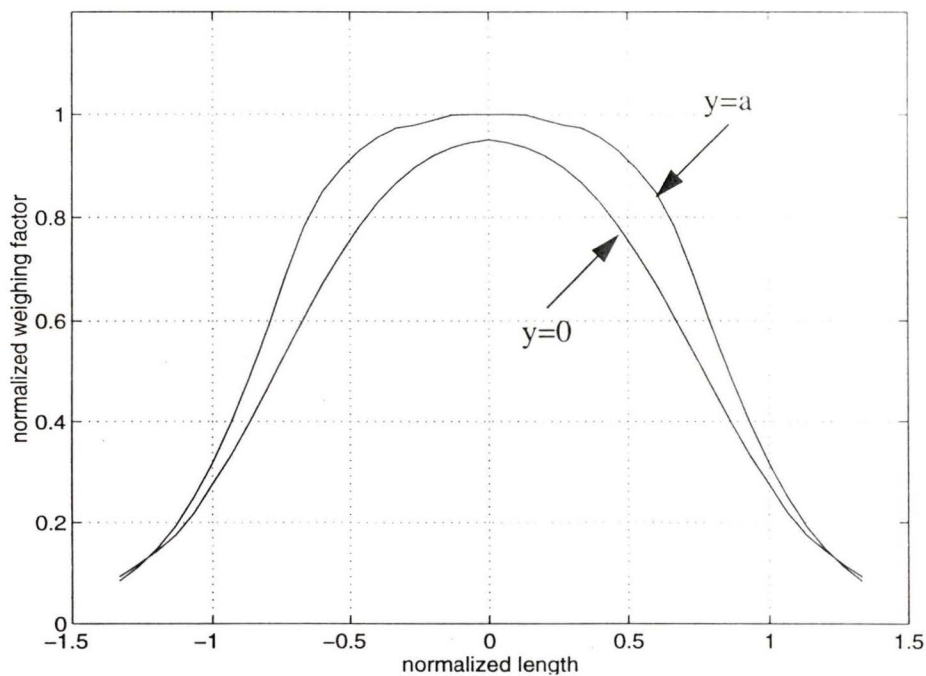


Figure 4.15 Weighing factor of Rogowski's profile sensor along x-axis at  $y=0$  and  $y=a$ .

#### 4.1.4 Uniform field sensor

To keep the advantages of the parallel-plate and Rogowski's profile sensor and overcome their shortcomings, a sensor should have a uniform field area as large as possible and have no high edge field.

Figure 4.16 shows a quarter of the whole configuration which is symmetrical with respect to  $x$ - and  $y$ -axis, which was proposed in [32]. Section AB is a flat part. Section B to C is a sinusoidal curve about axes CO and BO. That is

$$XY = CO \sin\left(\frac{BX}{BO} \cdot \frac{\pi}{2}\right) \quad (4.6)$$

In this configuration, segment B to C is critical. At point B, the sinusoidal curve not only is tangent to the flat part, but also has a infinite curvature radius. Section BC therefore, transfers from the sinusoidal curve to the flat part smoothly.

The results are shown in Fig. 4.18, Fig. 4.19 and Fig. 4.20. There are no fringing effects -- the field at edge area is only a little higher (about 2%) than in the uniform field area. The reason for this is that at the beginning of the curve BC (around point B), the curvature radius is infinite and decreases from B to C, and at point C, reaches a minimum. We know that the field strength at the edge area decreases with the increase of the radius of the edge. In our case, the curvature radius decreases form B to C, but at the same time, the distance between the two electrodes increases. The overall effect is that the field strength decreases.

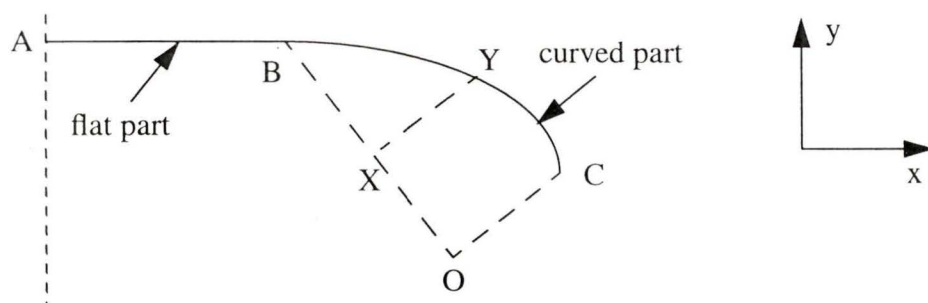


Figure 4.16 Half contour of the uniform field electrode [32].

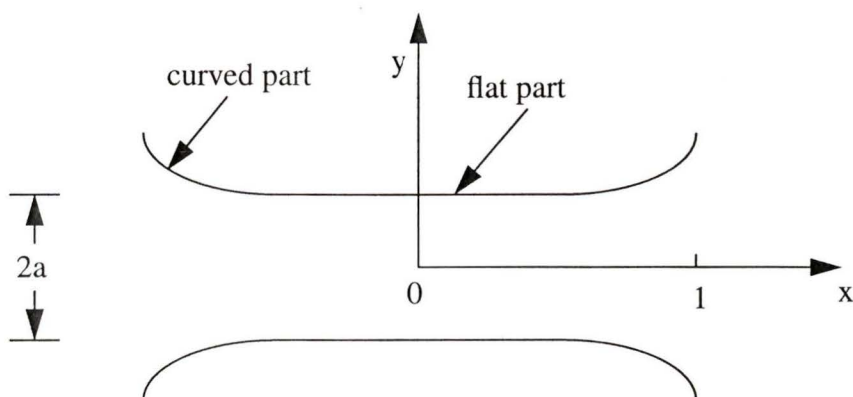


Figure 4.17 Configuration of the sensor with a flat part at center and curved part at the edge.

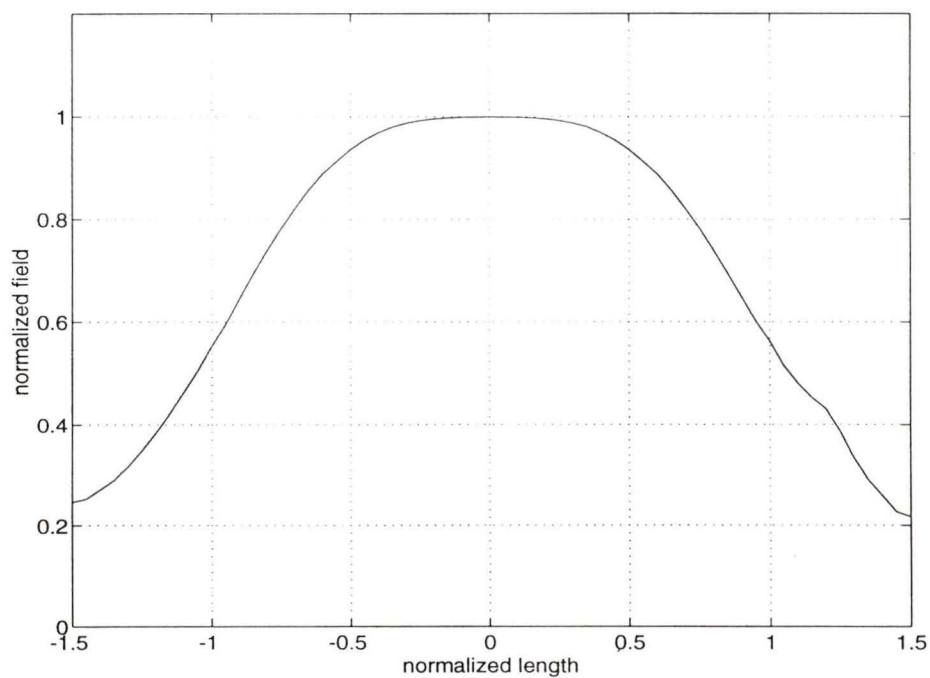


Figure 4.18 Field distribution along  $x$ -axis at  $y=0$  (center between the two electrodes).

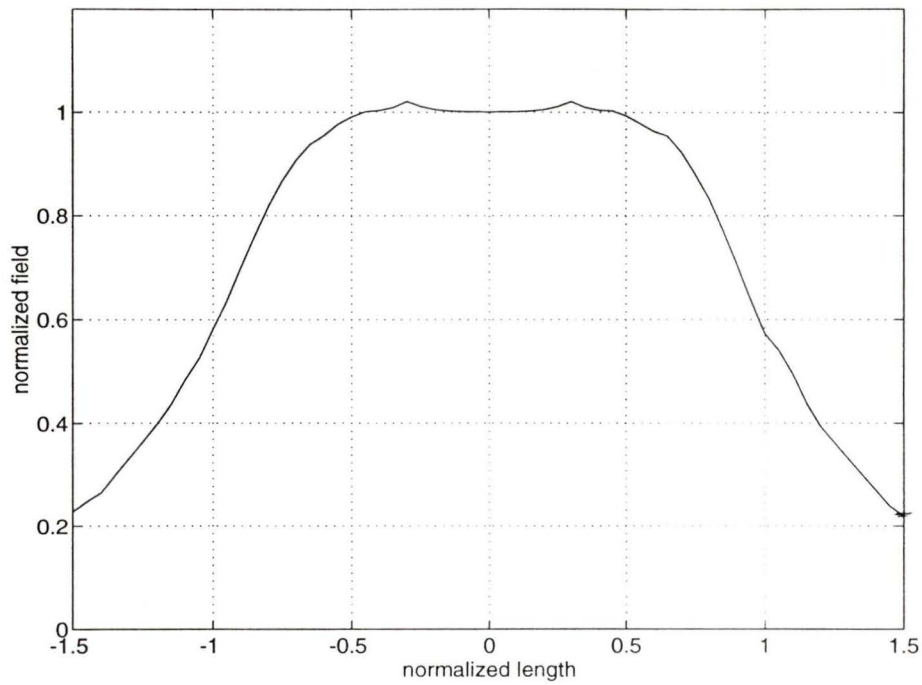


Figure 4.19 Field distribution along x-axis at  $y=a$  (along parallel part of the electrodes).

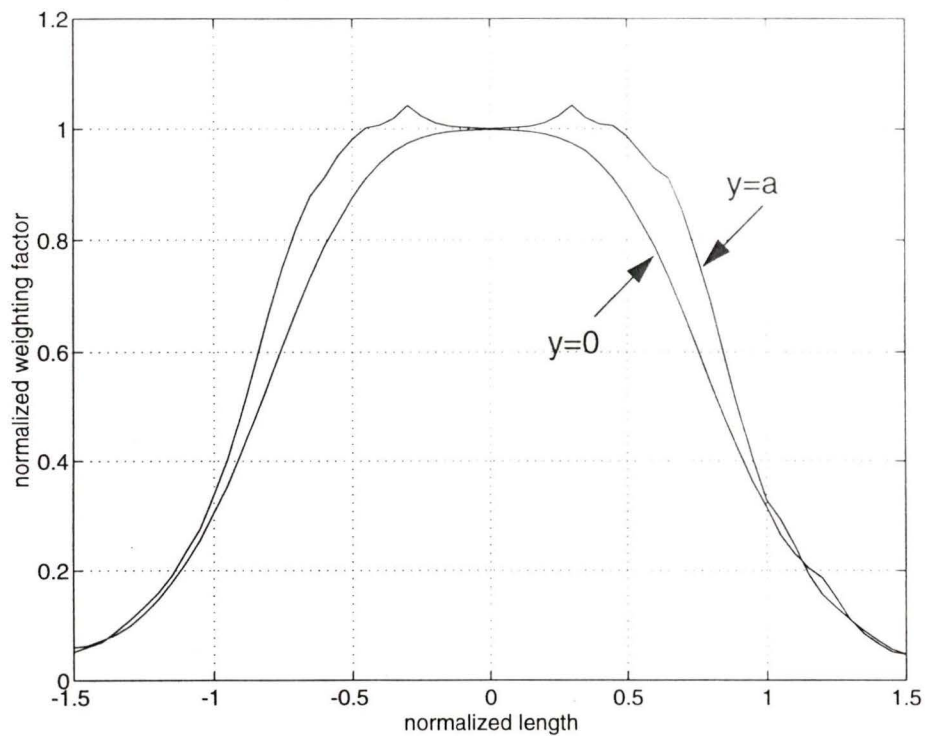


Figure 4.20 Weighing factor along x-axis at  $y=0$  and  $y=a$ .

### 4.1.5 Sensors with three electrodes

Three-electrode sensors have at least two advantages compared with the described sensors. First, they do not need a balun between the sensor and the connecting cable. Second, the outer electrodes shield the field from outside. This property makes three-electrode sensor similar to a closed configuration. Its measurement area is better defined than for other configurations.

The high field area is at the edge of the center electrode. By extending the width of the center electrode, the field decreases below that in the center area, as depicted in Fig. 4.22 and Fig. 4.23.

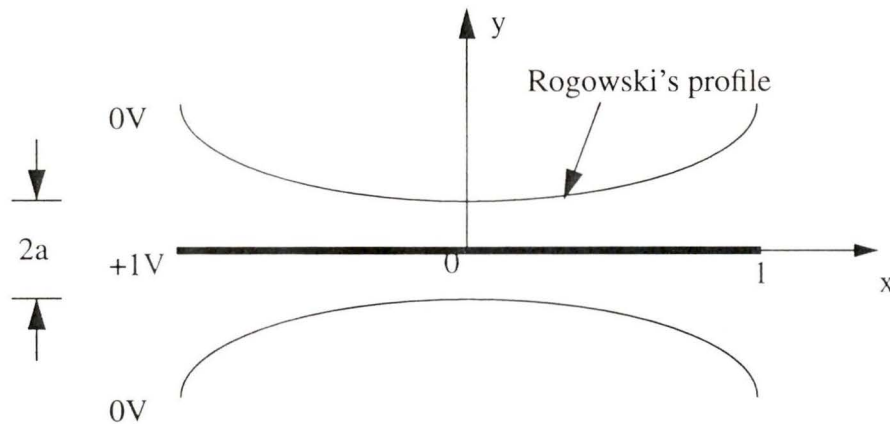


Figure 4.21 Configuration of the three-electrode sensor. The width of the Rogowski's profile which has the same parameters as in Fig. 4.12 is normalized to 1.

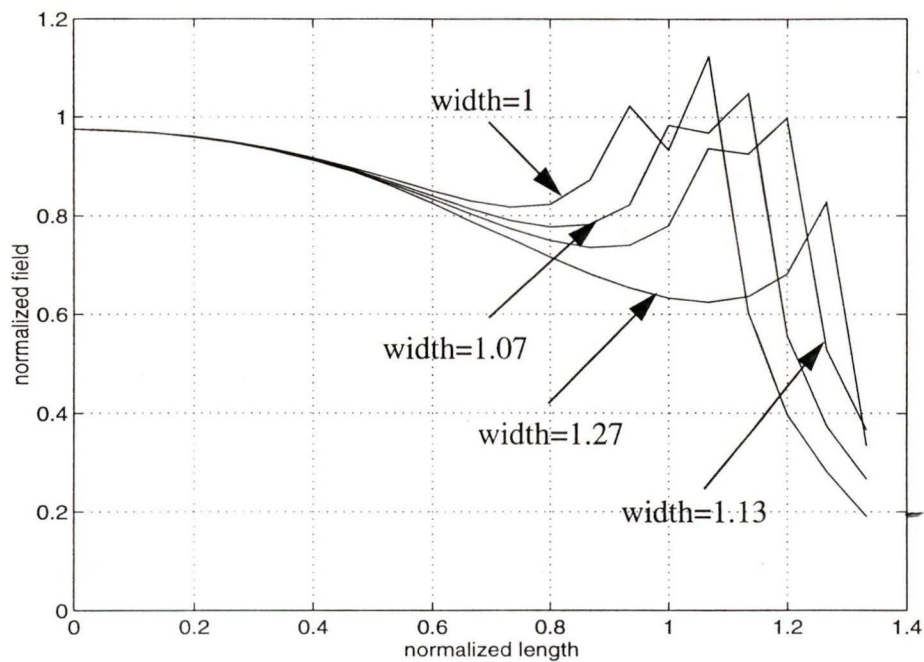


Figure 4.22 Field distribution along x-axis at  $y=0$  (along the center electrode). The lines represent different width of central electrodes. The electric field is normalized to that of three-parallel-plate sensor.

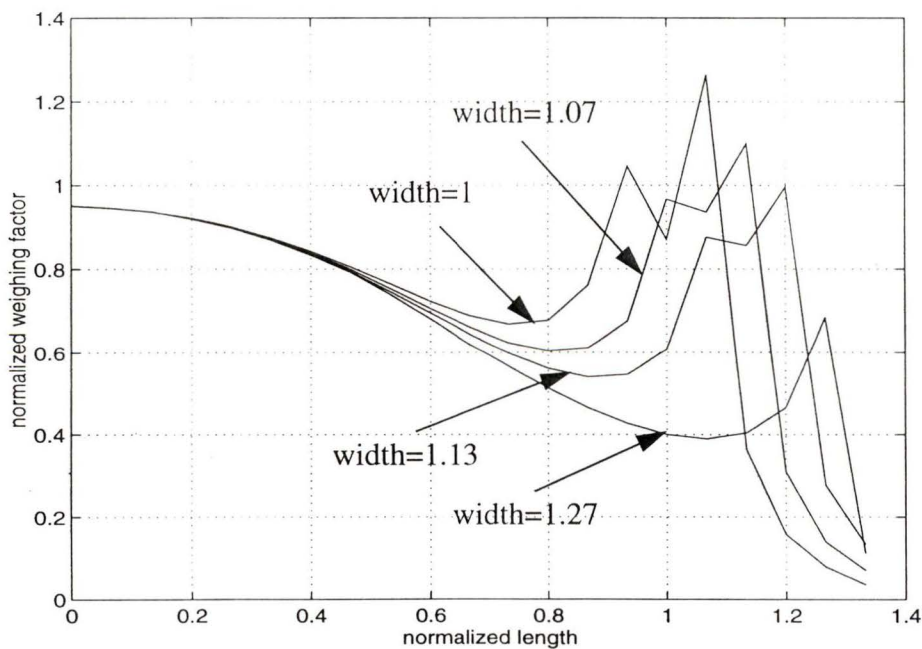


Figure 4.23 Weighing factor along x-axis at  $y=0$  (along the center electrode). The lines represent different width of central electrodes. The weighing factor is normalized to that of three-parallel-plate sensor.

All sensors proposed here use plates instead of presently used rods as the electrodes. These configurations make the insertion of the sensors into soil a little difficult. However, the sensors can be used in other areas, where they can be easily immersed in the measured substance. From this point of view, the proposed sensors may be more applicable to industrial applications.

## 4.2 Pulse Propagation - FDTD Results

### 4.2.1 Signal analysis for TDR system

Ramp, triangular and gaussian pulses are utilized in TDR systems as measurement signals [33] [34]. They all have easily identifiable sharp edges which allow accurate time measurements:

The rise time of a ramp signal  $t_r$  (See Fig. 4.24) determines its band-width. A shorter rise time means more high frequency components present (See Fig. 4.25). The ramp signal is a base-band signal and has a large DC component. The triangular pulse was proposed by Malicki *et al* (See Fig. 4.26) [33] [34]. The spectrum of the gaussian pulse is still a gaussian function. The triangular and gaussian pulses have a similar frequency spectrum to the ramp signal except a much lower DC component (See Fig. 4.27 and Fig. 4.29).

The band-width of the signals can be estimated by  $0.35/t_r$

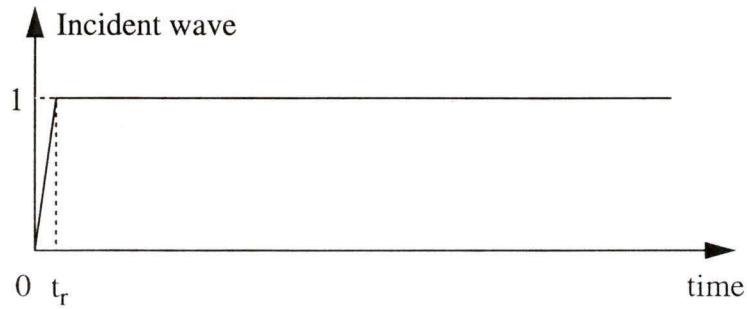


Figure 4.24 The normalized incident ramp signal with the rise time  $t_r$ .

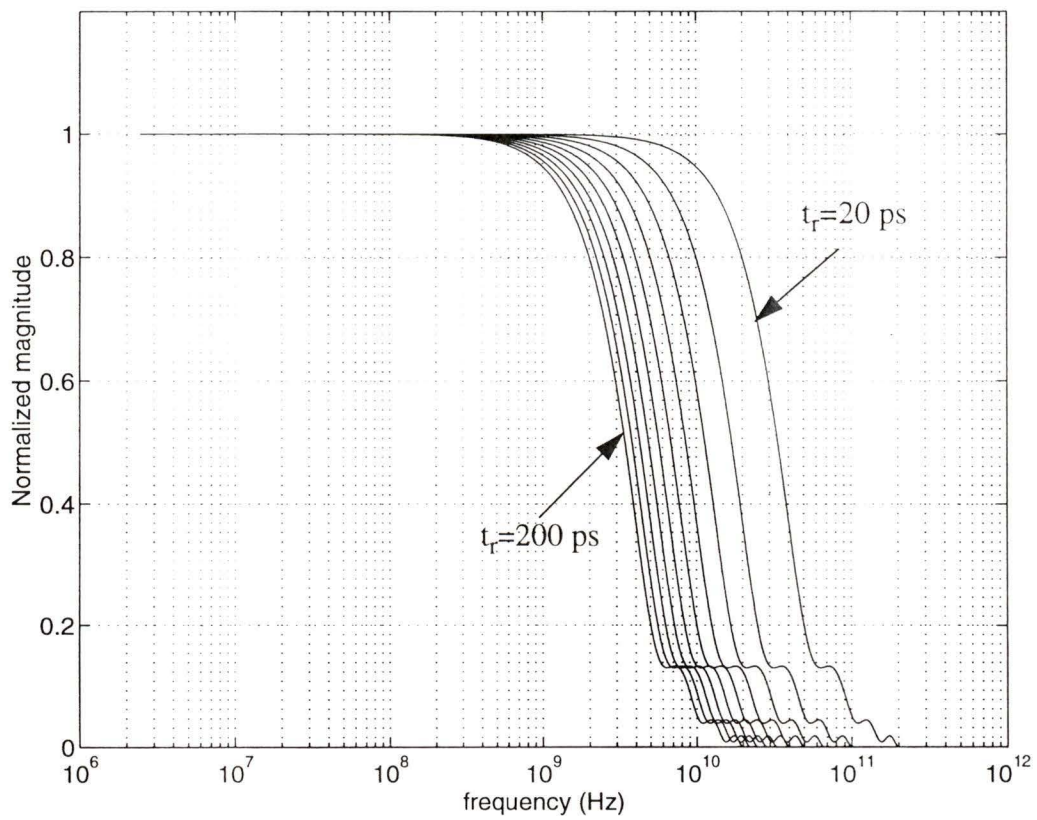


Figure 4.25 The FFT spectrum of the ramp signal with the rise time of 20, 40, 60, 80, 100, 120, 140, 160, 180, and 200 ps.

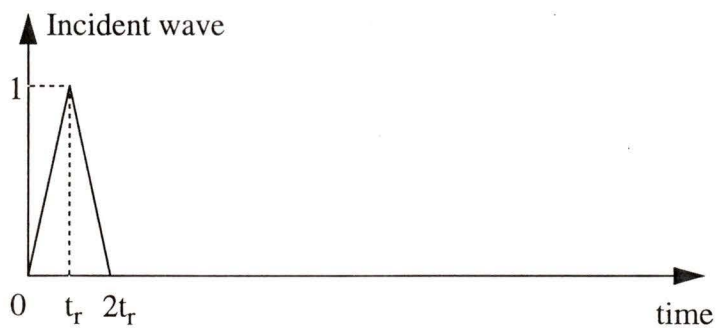


Figure 4.26 The normalized triangular pulse with the pulse width  $t_r$

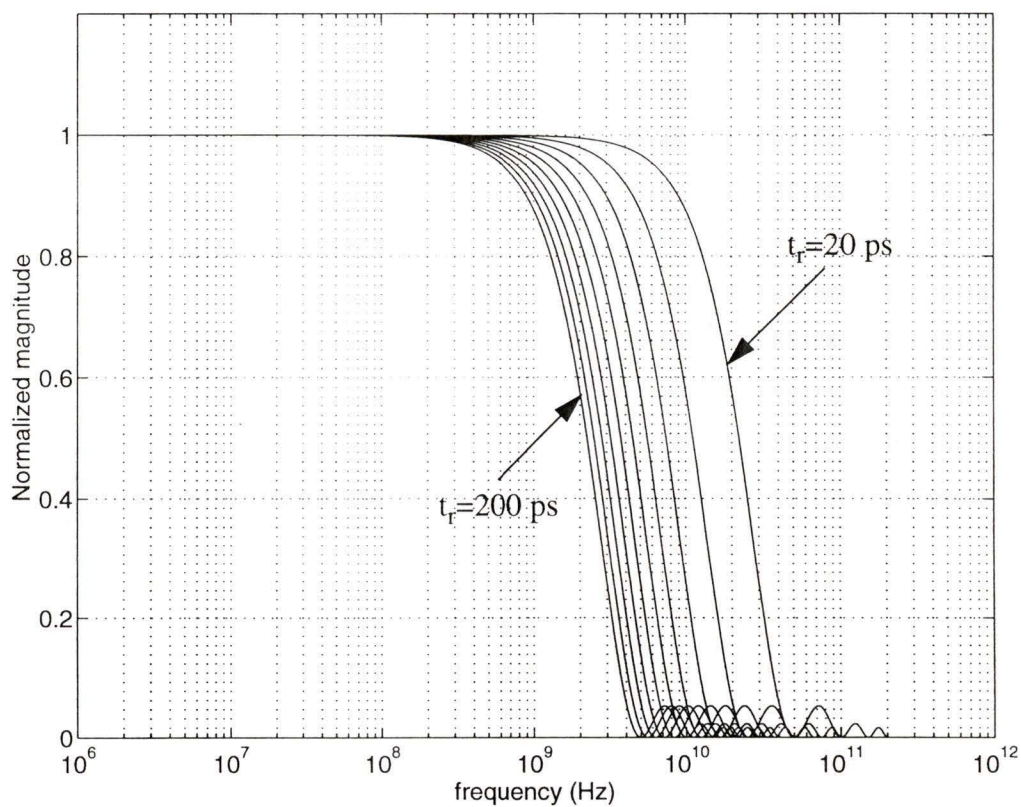


Figure 4.27 The FFT spectrum of the triangular pulse signal with the pulse width 20, 40, 60, 80, 100, 120, 140, 160, 180, and 200 ps.

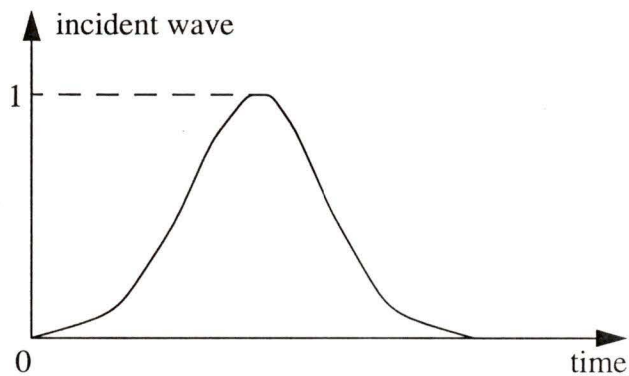


Figure 4.28 The normalized gaussian pulse.

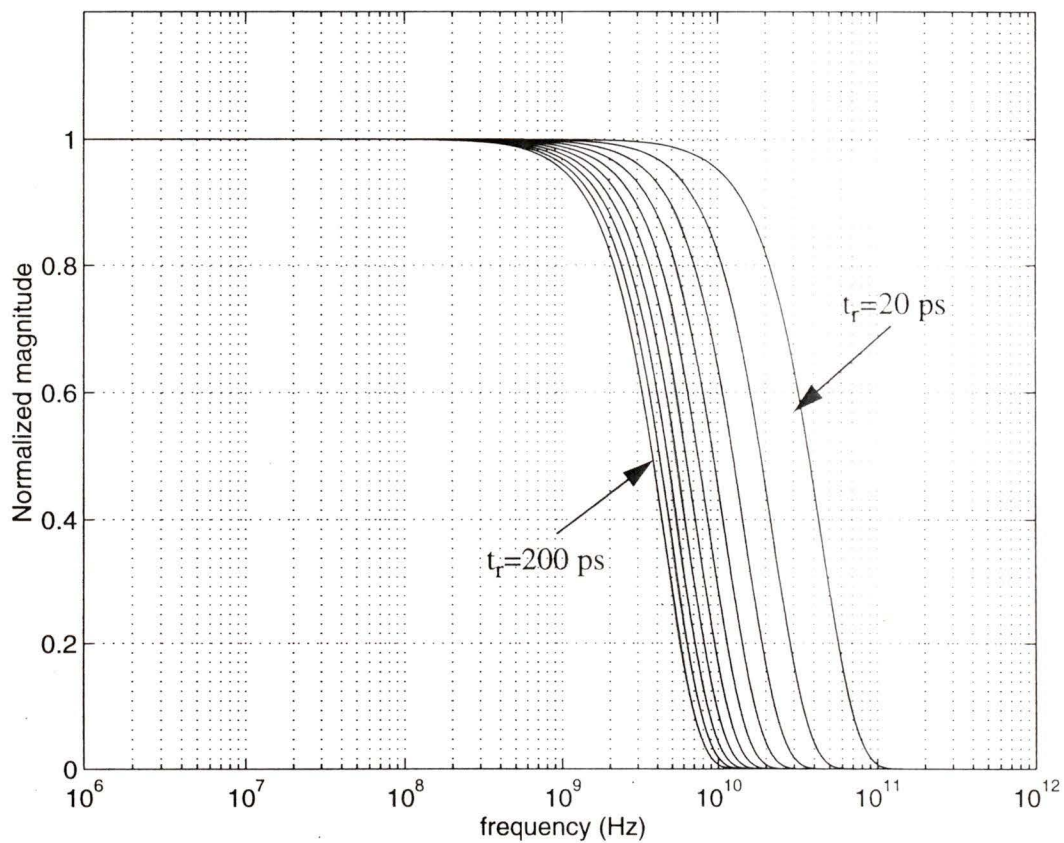


Figure 4.29 The FFT spectrum of the gaussian pulse with the pulse width 20, 40, 60, 80, 100, 120, 140, 160, 180, and 200 ps.

## 4.2.2 Pulse propagation in water

Water is present in almost every measurement situation and one of the most important applications of microwave sensors is measurement of moisture content, e.g. TDR technique application to soil moisture content measurement. We are, therefore, interested in the pulse propagation in water.

Water is a highly dispersive medium and obeys the Debye relation:

$$\epsilon = \epsilon_{\infty} + \frac{\epsilon_0 - \epsilon_{\infty}}{1 + j\tau_0\omega} \quad (4.7)$$

The constants in (4.7) could, in principle, be calculated approximately from the properties of the water molecule. There is, however, a substantial amount of measurement data available. Therefore, a best-fit polynomial approximations for the constants can be obtained [35]:

$$\epsilon_0 = 88.195 - 0.40349 \cdot t + 0.65924 \times 10^{-3} \cdot t^3 \quad (4.8)$$

$$\epsilon_{\infty} = 4.9 \quad (4.9)$$

$$\tau \times 10^{12} = 19.39 - 0.6802 \cdot t + 0.95865 \times 10^{-3} \cdot t^3 - 0.65303 \times 10^{-17} \cdot e^t \quad (4.10)$$

where the salinity is set to be 0 and  $t$  is the temperature in degrees (°C).

In calculation, we assume temperature  $t=25$  °C. Then the dielectric constant at low frequency is  $\epsilon_0=78.5198$ , the high frequency dielectric constant is  $\epsilon_{\infty}=4.9$ , and the relaxation frequency is  $\omega_0=1/\tau=1.1938 \times 10^{11}$  rad/s.

An incident gaussian pulse in air is applied to water:

$$E(z, t) = e^{-\frac{(t-z/c_0)^2}{2t_1^2}} \quad (4.11)$$

where  $t_1$  is one half of the pulse width in time,  $c_0$  is the velocity of light in free space, and  $z=0$  at the interface (See Fig. 4.30). We use half pulse width  $t_1=50$  ps.

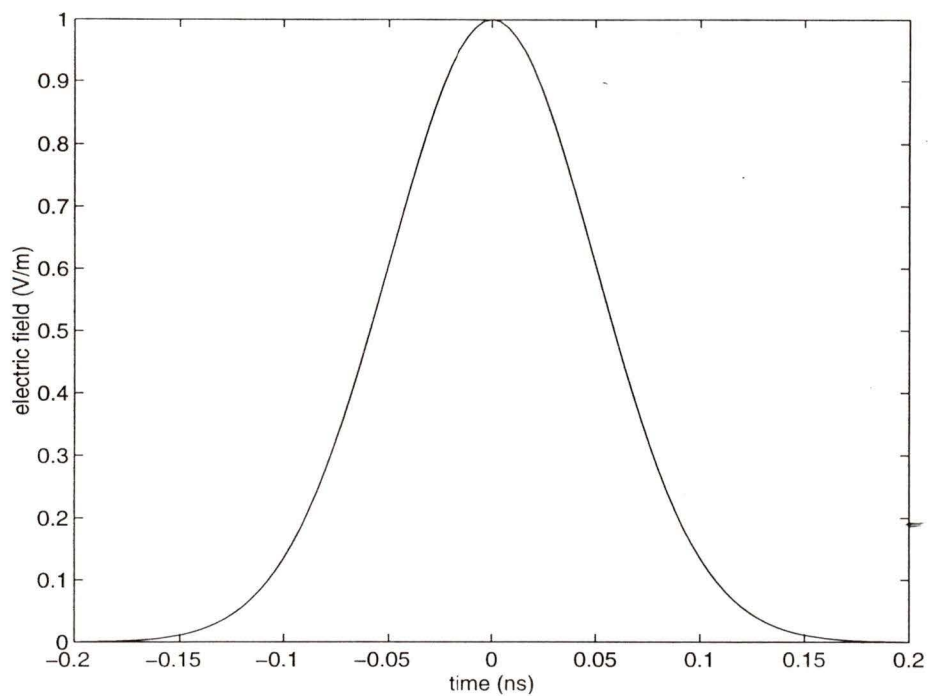


Figure 4.30 Gaussian pulse in air at  $z=0$  as a function of time.

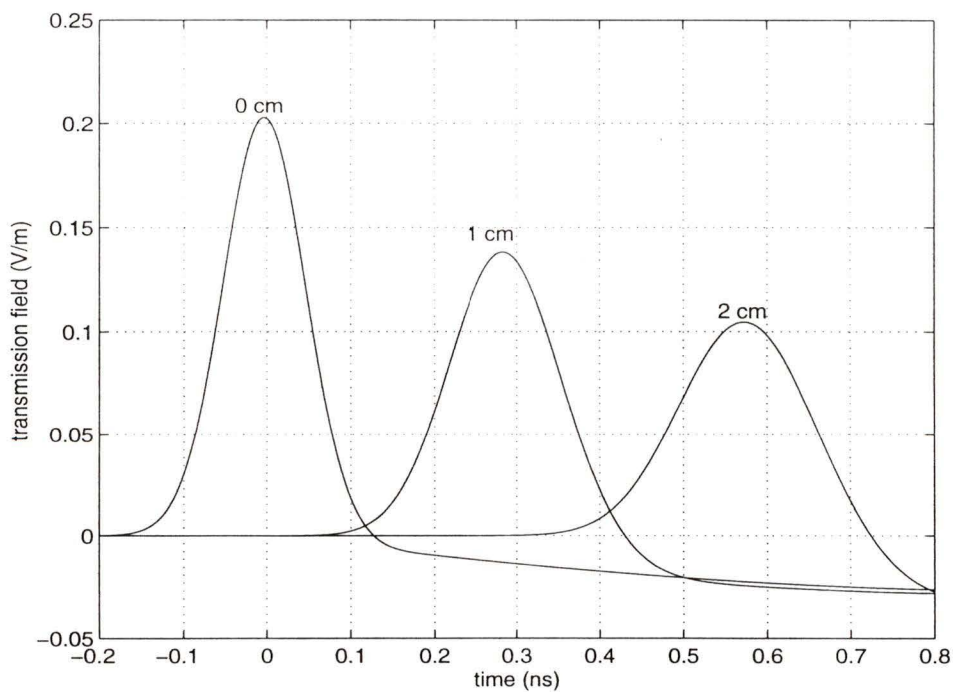


Figure 4.31 Gaussian pulse propagating in water as a function of time. The pulse width is 100 ps.

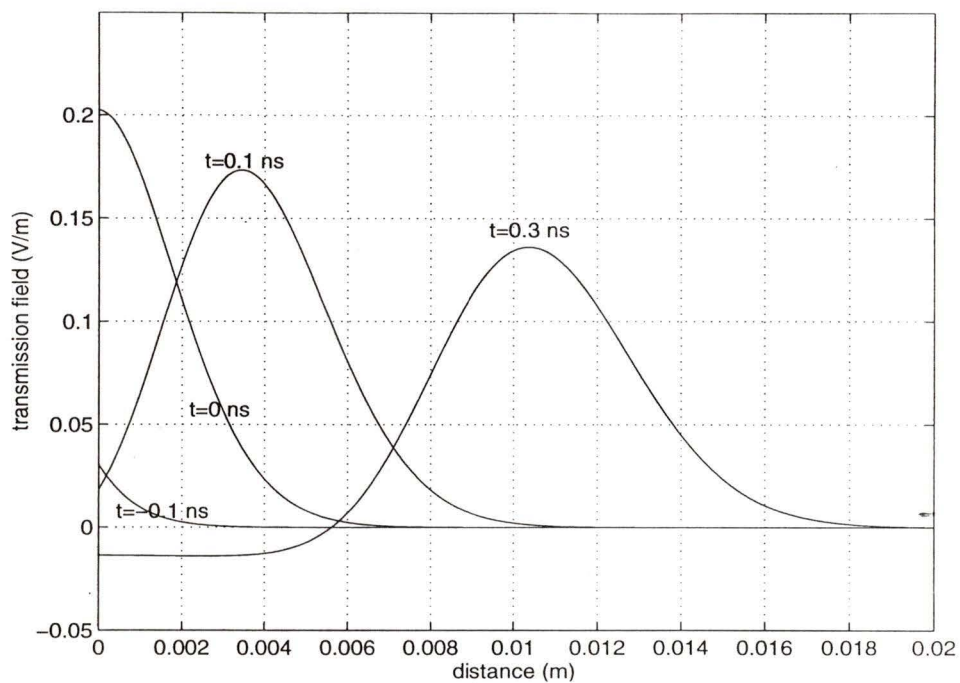


Figure 4.32 Gaussian pulse propagating in water as a function of distance. The pulse width is 100 ps

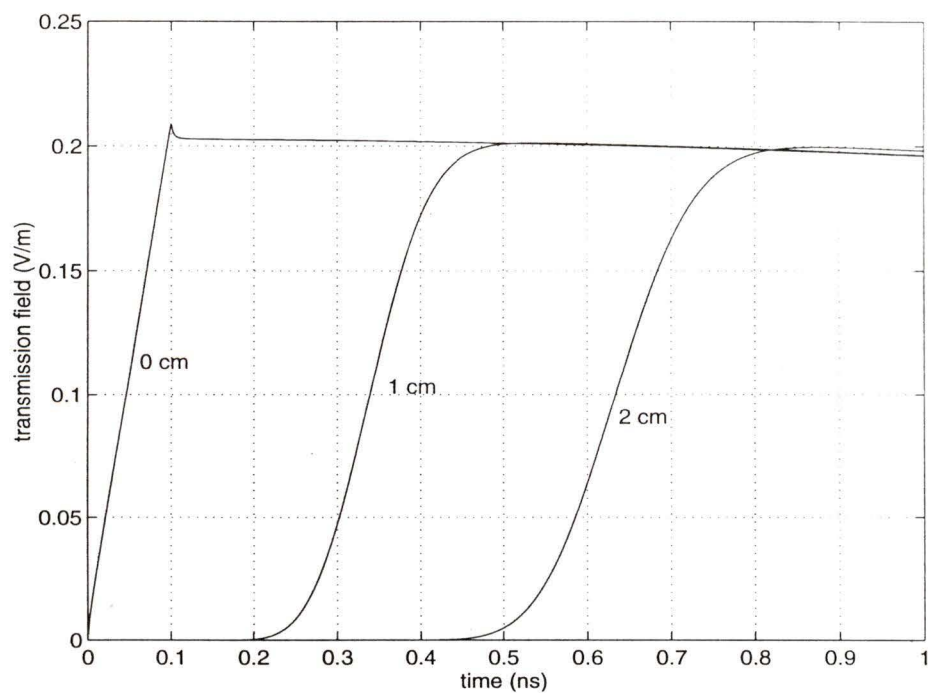


Figure 4.33 Ramp signal propagating in pure water as a function of time. The rise time is 100 ps.

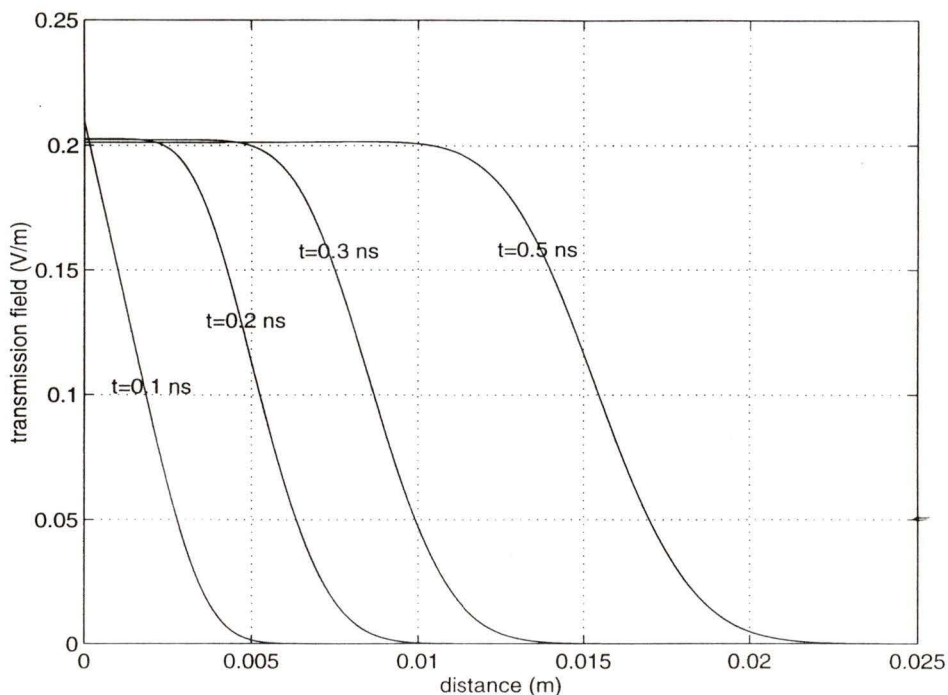


Figure 4.34 Ramp signal propagating in pure water as a function of distance. The rise time of the ramp is 100 ps.

Figure 4.31 shows the gaussian pulse as a function of time at different depths of water: at air-water interface, 1 cm and 2 cm. From this figure, we can see that the half-magnitude pulse width is 0.1 ns at the air-water interface, 0.154 ns at 1 cm, and 0.179 ns at 2 cm. Figure 4.32 shows the gaussian pulse in space at various time points: 0.1 ns, 0.2 ns, 0.3 ns and 0.5 ns. From the results, we could see that the magnitude of gaussian pulse decreases with the depth while pulse width widens even for pulses propagating only a small distance.

Figure 4.33 shows the ramp as a function of time at different depths: at air-water interface, 1 cm and 2 cm. The figure shows the increasing of the rise time of the ramp. From this figure, we can see that the rise time of the ramp is 0.1 ns at air-water interface, 0.142 ns at 1cm, and 0.186 ns at 2cm. Figure 4.34 shows the ramp signal in space at various time points: 0.1 ns, 0.2 ns, 0.3 ns and 0.5 ns. The results shows that the rise time of the ramp increases as it propagates along the sensor in water.

### 4.2.3 Pulse propagation in wet soil

For wet soil calculations, data of Suffield silty clay was used [3]. The data are fit to Debye relation to obtain constants in (4.7). The high frequency dielectric constant is  $\epsilon_{\infty}=14.6$ , the low frequency dielectric constant is  $\epsilon_0=4.5$ , and the relaxation frequency is  $f_0=1.5\times 10^9$  Hz.

Figure 4.35 shows the gaussian pulse (See Fig. 4.30) propagating in soil as a function of time at different depth: at air-soil interface, 20 cm and 30 cm. The depths are approximately equal to the length of TDR sensors. From this figure, we can see that the half-magnitude pulse width is 0.1 ns at the air-soil interface, 0.84 ns at 20 cm, and 1.05 ns at 30 cm. The pulse width becomes wider as it propagates along the sensor. Figure 4.36 shows the gaussian pulse in space at different time points:  $t=0$ ,  $t=2.5$  ns and  $t=4$  ns. The behavior of the gaussian pulse is similar to that in water. The magnitude decreases with the propagation and the pulse becomes wider.

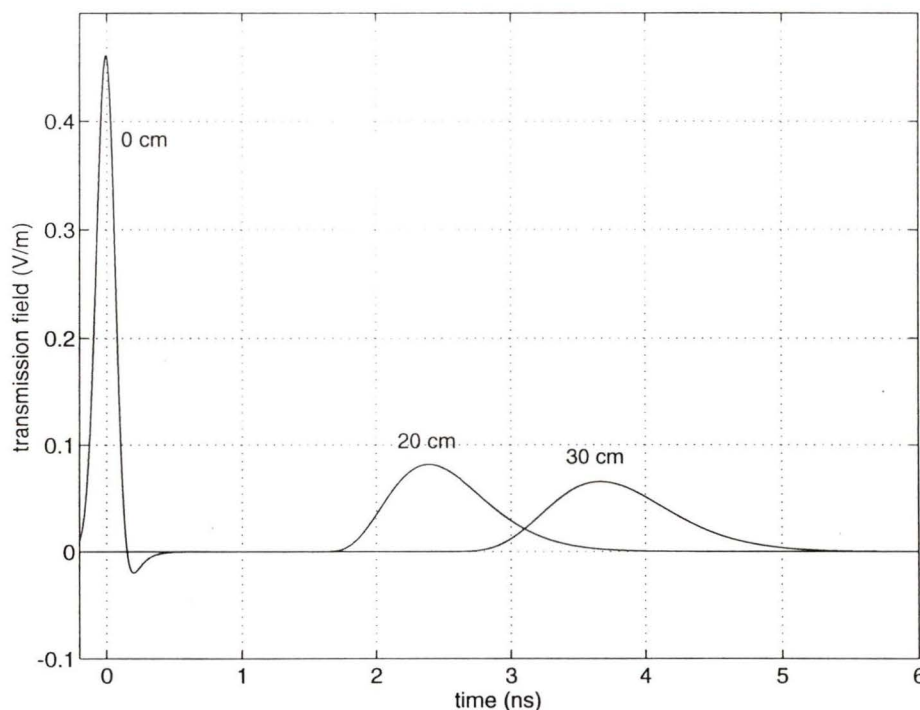


Figure 4.35 Gaussian pulse propagating in soil as a function of time. The pulse width is 100 ps.

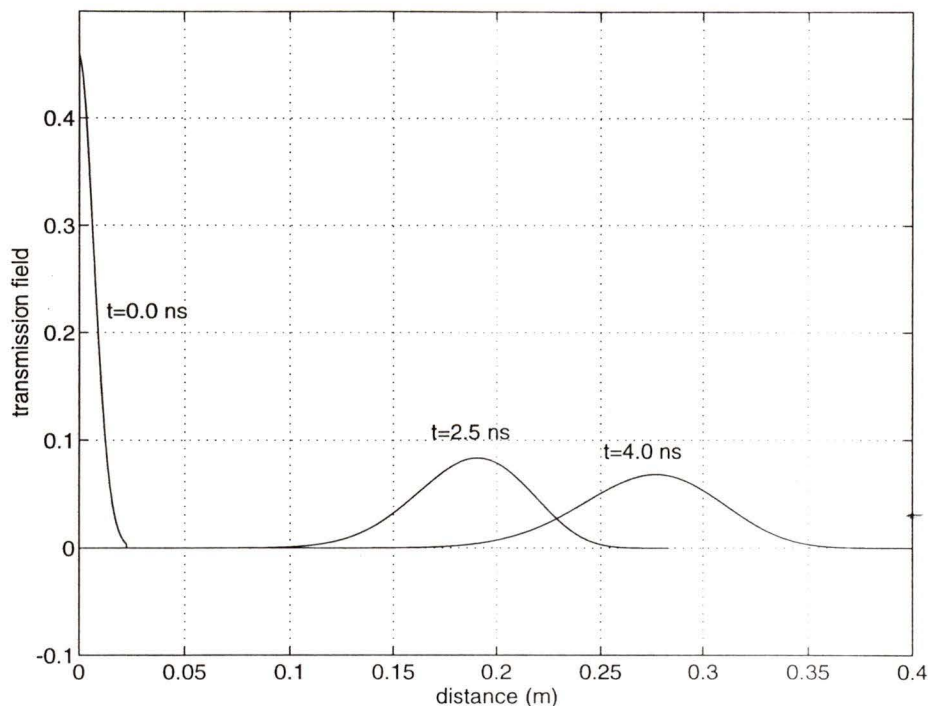


Figure 4.36 Gaussian pulse propagating in soil as a function of distance. The pulse width is 100 ps.

Fig. 4.37 shows the ramp as a function of time at different depths: at air-soil interface, 20 cm and 30 cm. From this figure, we can see that the rise time is 0.1 ns at air-soil interface, 1.01 ns at 20 cm, and 1.15 ns at 30 cm. The rise time of the ramp is longer as the wave propagates along the sensor. Figure 4.38 depicts the ramp in space at the following time points:  $t=0$ ,  $t=0.1$  ns,  $t=2.5$  ns and  $t=3.6$  ns. From these two figures, we can see that the magnitudes of the ramp do not change significantly, but the rise time increases significantly.

From above calculations, we can see that the dispersion of soil significantly affects the wave shape and that accurate measurements are difficult. Recently, Hook and Livingston [18] developed a circuit for the waveform subtraction technique that greatly improves the effective amplitude of the desired reflection and significantly reduces background noise. The results also show that there is no significant decrease on ramp signal's amplitude while the amplitude of the gaussian pulse decreases with the propagation.

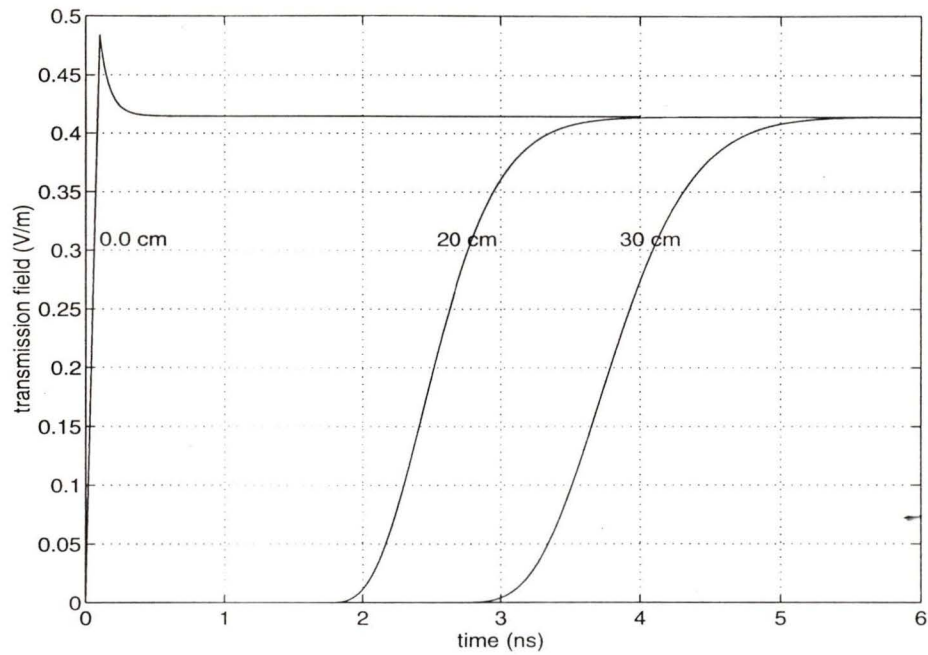


Figure 4.37 Ramp signal propagating in soil as a function of time. The rise time of the ramp is 100 ps.

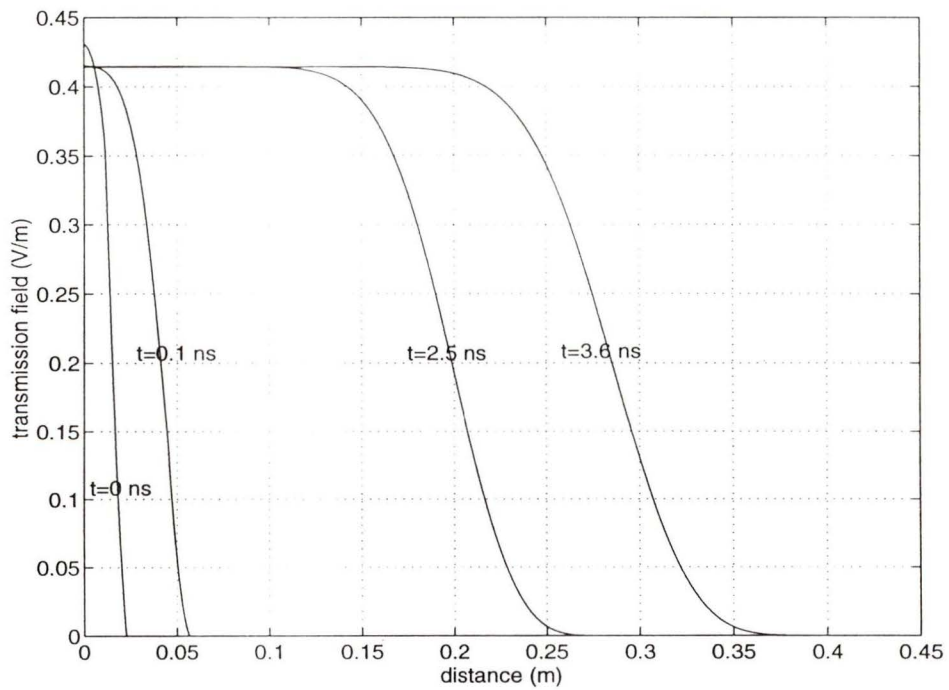


Figure 4.38 Ramp signal propagating in soil as a function of distance. The rise time is 100 ps.

# Chapter 5

## Sensitivity Experiment

In this chapter, the sensitivity experiments with a TDR sensor are discussed. Perturbation method is used in the experiments. The experimental system is described and the results and the uncertainties are analyzed.

### 5.1 Experimental Techniques

#### 5.1.1 Objectives

The first of objective of the experiments is to test the specifications of the TDR sensors, which are described in Section 4.1. These specifications include:

1. There should be a uniform electric field region, which is as large as possible compared with the sampling volume of the sensor, so that the weighing factor of the measurement remains constant throughout the sensing volume;
2. The field should decrease as fast as possible outside the uniform field area, i.e., the field's "tail" should be as short as possible.

The second objective of these experiments is to compare the sensitivity of sensors calculated using numerical methods with the perturbation method. The third objective is to investigate the effects of small perturbations around the sensors on the measurement results.

### 5.1.2 Perturbation theory

Perturbation methods are widely used in solving various engineering problems. The method can be applied to any electromagnetic resonant problem because the Maxwell's equations are universally applicable.

In air, the fields satisfy Maxwell's equations as following:

$$\nabla \times \vec{E}_0 = -j\omega_0\mu_0\vec{H}_0 \quad (5.1)$$

$$\nabla \times \vec{H}_0 = j\omega_0\varepsilon_0\vec{E}_0 \quad (5.2)$$

And in any area filled with a homogeneous medium with permittivity  $\varepsilon$  and permeability  $\mu$ , the fields satisfy:

$$\nabla \times \vec{E} = -j\omega\mu\vec{H} \quad (5.3)$$

$$\nabla \times \vec{H} = j\omega\varepsilon\vec{E} \quad (5.4)$$

In an air-filled cavity, a small dielectric body with permittivity  $\varepsilon$  and permeability  $\mu$  is introduced. Assume the cavity occupies a volume  $v$  and the dielectric occupies a volume  $v_1$ , and  $\omega_0$  is the resonant frequency without the small dielectric body and  $\omega$  is the resonant frequency with the dielectric body in the cavity. We can obtain the relative frequency change (See Appendix A):

$$\frac{\omega - \omega_0}{\omega} = -\frac{(\varepsilon - \varepsilon_0) \int_{v_1} \vec{E} \cdot \vec{E}_0^* dv + (\mu - \mu_0) \int_{v_1} \vec{H} \cdot \vec{H}_0^* dv}{\varepsilon_0 \int_v \vec{E} \cdot \vec{E}_0^* dv + \mu_0 \int_v \vec{H} \cdot \vec{H}_0^* dv} \quad (5.5)$$

There are not any approximations made up to this point. For  $v_1 \ll v$ , the denominator of (5.5) can be simplified as:

$$\varepsilon_0 \int_v \vec{E} \cdot \vec{E}_0^* dv + \mu_0 \int_v \vec{H} \cdot \vec{H}_0^* dv \approx \varepsilon_0 \int_v \vec{E}_0 \cdot \vec{E}_0^* dv + \mu_0 \int_v \vec{H}_0 \cdot \vec{H}_0^* dv = 4W_0 \quad (5.6)$$

where  $W_0$  is the total electromagnetic energy without perturbation. Then, (5.6) becomes:

$$\frac{\omega - \omega_0}{\omega} = -\frac{(\epsilon - \epsilon_0) \int_{v_1} \vec{E} \cdot \vec{E}_0^* dv + (\mu - \mu_0) \int_{v_1} \vec{H} \cdot \vec{H}_0^* dv}{4W_0} \quad (5.7)$$

Assume the dielectric is a non-magnetic material. For the loaded quality factor  $Q_L \gg 1$  and  $\omega \cong \omega_0$ :

$$\frac{\omega - \omega_0}{\omega} = -\frac{\epsilon_0 (\epsilon'_r - 1)}{4W_0} \int_{v_1} \vec{E} \cdot \vec{E}_0^* dv \quad (5.8)$$

where  $W_0$  is:

$$W_0 = \frac{1}{2} \epsilon_0 \int_v |\vec{E}_0|^2 dv \quad (5.9)$$

Therefore, the dielectric perturbation causes a shift of the resonant frequency. The resonant frequency change can be estimated, provided that the dielectric constant and the volume of the perturbation dielectric are known.

In (5.8), the electric field in the perturbation  $\mathbf{E}$  is unknown. To calculate  $\mathbf{E}$ , we assume the condition that  $v_1 \ll v$ , and the dimension of perturbation is much smaller than the wave length. Then the electric field for a small sphere is:

$$\vec{E} = \frac{3}{2 + \epsilon'_r} \vec{E}_0 \quad (5.10)$$

where  $\epsilon'_r$  is the relative dielectric constant of the perturbation element, and  $\mathbf{E}_0$  is the field without perturbation.

### 5.1.3 Principle of experiment

To investigate the sensitivity of TDR sensors, an oscillation circuit is designed. The oscillation frequency is determined by the TDR sensor, which acts as a capacitor in the circuit. The capacitance of the sensor reflects the stored electric energy in the capacitor. A

small dielectric or metal sphere between the sensor's electrodes causes the capacitance change and, in turn, shifts the oscillation frequency from the original one. Therefore, through the measurement of the oscillation frequency change for different positions of the small sphere, the local weighing factor, which is proportional to the local electric energy, can be measured.

We can obtain the relation between the oscillation frequency change and the weighing factor. Substituting  $W_0$  and  $\mathbf{E}$  in (5.8) with (5.9) and (5.10), respectively, we get:

$$\frac{\omega - \omega_0}{\omega} = -\frac{\epsilon'_r - 1}{2 \int_v |\dot{\mathbf{E}}_0|^2 dv} \int_{v_1} \frac{3}{2 + \epsilon'_r} \dot{\mathbf{E}}_0 \cdot \dot{\mathbf{E}}_0^* dv = -\frac{3(\epsilon'_r - 1) \int_{v_1} |\dot{\mathbf{E}}_0|^2 dv}{2(\epsilon'_r + 2) \int_v |\dot{\mathbf{E}}_0|^2 dv} \quad (5.11)$$

For a small volume  $v_1$ , the internal electric field can be assumed uniform. So, the integral  $\int_{v_1} |\dot{\mathbf{E}}_0|^2 dv$  is expressed as  $|\dot{\mathbf{E}}_0|^2 \cdot v_1$ . Then (5.11) becomes:

$$\frac{\omega - \omega_0}{\omega} = -\frac{3(\epsilon'_r - 1) v_1}{2(\epsilon'_r + 2)} \frac{|\dot{\mathbf{E}}_0|^2}{\int_v |\dot{\mathbf{E}}_0|^2 dv} \quad (5.12)$$

Comparing with (3.4), we can see the change of the oscillation frequency is proportional to the weighing factor.

From above analysis, we conclude that under small perturbation assumption, the weighing factor is proportional to the electric energy stored in the TDR sensor.

#### 5.1.4 Experiment system

The oscillation circuit is built using a Phase Locked Loop IC, NE 564, in which the VCO is used as the oscillator. This IC has an advantage over other circuits in that only a capacitor is needed as an external component to build the oscillator. This simple configuration makes it easy to obtain highly stable and reliable circuit.

The sensor under test is connected to the PLL as an external capacitor in to control the oscillation frequency. It is mounted on a fixed base for measurement convenience.

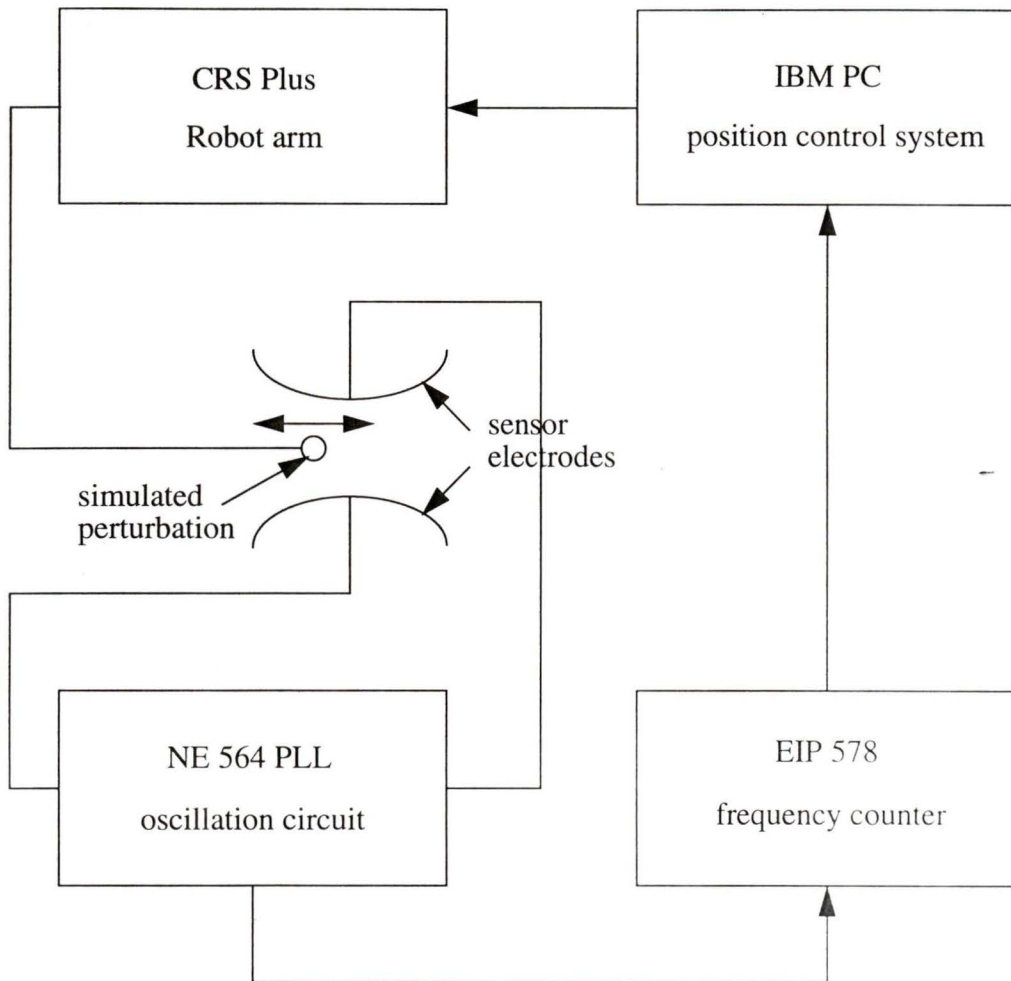


Figure 5.1 The configuration of the experiment system.

A EIP Model 578 Source Locking Microwave Counter is used to measure the oscillation frequency and with a standard interface, the counter's read-out can be stored in a PC computer for further processing.

A CRS Plus Robot-arm is employed to carry out the perturbation element position control. The robot-arm is controlled by a microcomputer in which the control and communication software are installed. The control software provides an integrated environment and simple programmable commands to control the robot-arm's movements.

A small (0.4 cm in diameter) steel sphere is used as the perturbation body. It is fixed on a fish line, which fastens to a frame, so that its position is controlled by the movements of the robot arm.

## 5.2 Experimental Results

### 5.2.1 Weighing function measurement

The experiment is conducted for the parallel-plate sensor. The sensor is designed to form a line with  $50 \Omega$  characteristic impedance. According to the calculation in Section 3.2.2, the dimension factor is  $d/b=0.167$ . We set  $d=2.0$  cm. Then,  $b=12.0$  cm. The test sensor is made of two  $12.0 \times 12.0$  cm<sup>2</sup> plates. The coordinate system used in the experiment is illustrated in Fig. 5.2. The perturbation element is moved in the plane  $z=0$ . The capacitance of the parallel-plate sensor was found to be 24.95 pF.

Table 5.1 shows the experimental results at  $y=0.0$  and  $1.0$  cm, respectively. The last row in the table for  $x=\infty$  is the oscillation frequency with no perturbation  $\omega_0$ .

To compare with the calculated weighing factor of the parallel-plate sensor, the experimental data are normalized and fit to the theoretical normalized weighing factor according to (5.12). Figure 5.3 shows the normalized weighing factors obtained from three sets experiment data and the theoretical weighing factor at  $y=0.0$  cm. Figure 5.4 show the normalized weighing factors obtained from two sets experiment data and the theoretical weighing factor at  $y=1.0$  cm.

From the experiment results, we can see that the theoretical weighing factor is consistent with the experimental data. This confirms the sensitivity of the parallel-plate sensor obtained from numerical calculation. The parallel-plate sensor has a uniform sensitivity around electrode's center. However, the sensitivity at the electrode's edge is higher than that in the center area, as shown in Fig. 5.4.

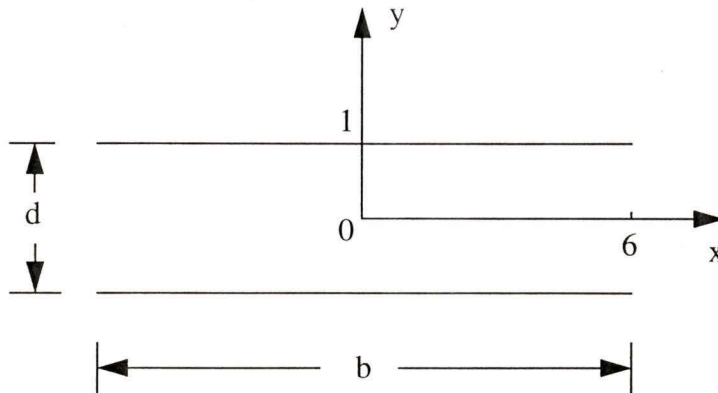


Figure 5.2 The coordinate system of the test parallel-plate sensor.

Table 5.1. The sensitivity experiment data of the parallel-plate sensor.

x (cm)	y=0.0 cm			y=1.0 cm	
	Test 1 frequency (MHz)	Test 2 frequency (MHz)	Test 3 frequency (MHz)	Test 1 frequency (MHz)	Test 2 frequency (MHz)
0.0	9.6042	9.6035	9.6046	9.6010	9.5997
0.5	9.6047	9.6039	9.6042	9.6011	9.6007
1.0	9.6047	9.6040	9.6039	9.6009	9.6006
1.5	9.6039	9.6034	9.6041	9.6008	9.6008
2.0	9.6044	9.6035	9.6040	9.6012	9.6008
2.5	9.6048	9.6035	9.6043	9.6017	9.6005
3.0	9.6049	9.6042	9.6055	9.6007	9.6007
3.5	9.6048	9.6037	9.6059	9.6017	9.6008
4.0	9.6049	9.6055	9.6064	9.6015	9.6010
4.5	9.6046	9.6063	9.6061	9.6017	9.6008
5.0	9.6053	9.6065	9.6068	9.6018	9.6009
5.5	9.6059	9.6069	9.6073	9.6011	9.6007
6.0	9.6065	9.6080	9.6082	9.6000	9.5990
6.5	9.6074	9.6086	9.6090	9.6039	9.6023
7.0	9.6079	9.6095	9.6098	9.6037	9.6028
7.5	9.6104	9.6095	9.6097	9.6033	9.6033
8.0	9.6112	9.6100	9.6099	9.6056	9.6034
8.5	9.6115	9.6104	9.6100	9.6057	9.6036

x (cm)	y=0.0 cm			y=1.0 cm	
	Test 1 frequency (MHz)	Test 2 frequency (MHz)	Test 3 frequency (MHz)	Test 1 frequency (MHz)	Test 2 frequency (MHz)
9.0	9.6115	9.6104	9.6103	9.6057	9.6038
9.5	9.6118	9.6107	9.6104	9.6057	9.6036
10.0	9.6116	9.6104	9.6106	9.6060	9.6038
10.5	9.6119	9.6107	9.6111	9.6059	9.6046
11.0	9.6118	9.6108	9.6109	9.6059	9.6043
11.5	9.6119	9.6110	9.6110	9.6062	9.6044
12.0	9.6118	9.6113	9.6115	9.6061	9.6044
$\infty$	9.6118	9.6115	9.6115	9.6060	9.6046

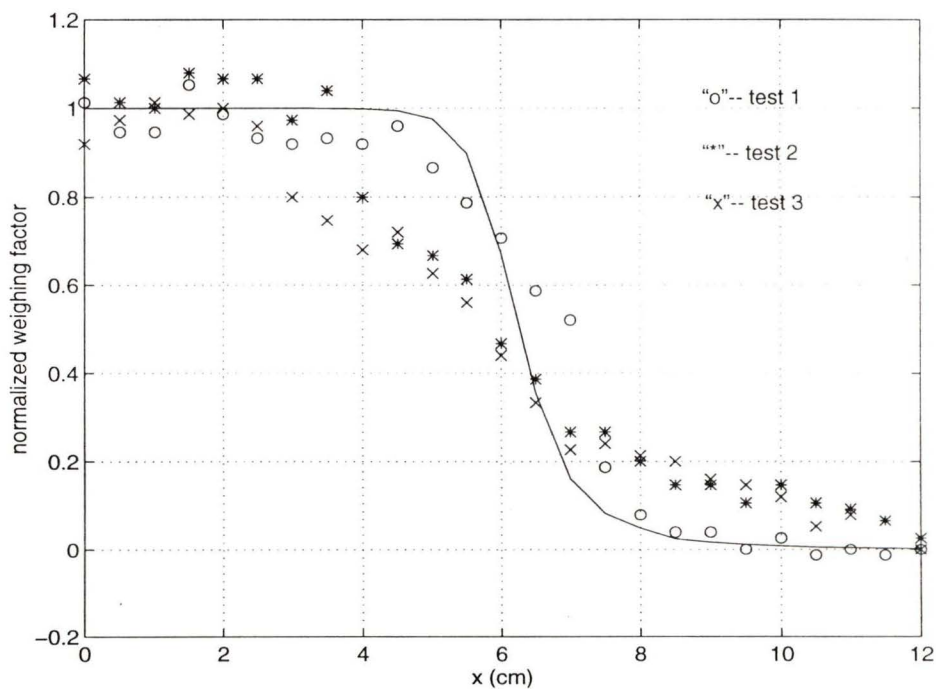


Figure 5.3 The normalized experiment and theoretical weighing factors at  $y=0.0$  cm. The solid line is the theoretical result and the separate data points are experimental results.

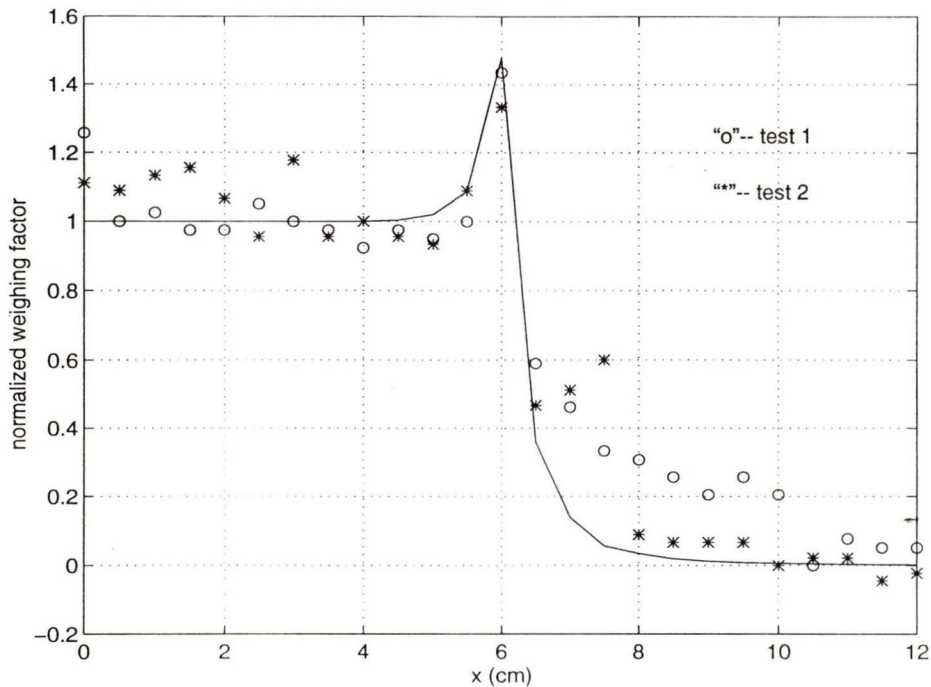


Figure 5.4 The normalized experiment and theoretical weighing factors at  $y=1.0$  cm. The solid line is the theoretical result and the separate data points are experimental results.

### 5.2.2 Uncertainty analysis

The uncertainties of the experiment come from several sources. The perturbation method itself is an approximation. The error is inevitable. To reduce this error, a small perturbation should be used. However, the smaller perturbation causes smaller frequency change which may be difficult to be accurately measured. So, it is necessary to compromise at this point. The rates of the frequency change  $(\omega - \omega_0)/\omega$  in the experiments are in the order of  $10^{-4}$ , which is the expected frequency shift in the perturbation methods. This value compromises both the theoretical and experimental accuracy.

Other uncertainties are from the measurement instruments and experiment operations. The accuracy of the position is determined by the robot arm's movement accuracy and the sensor's placement. With careful placement of the sensor, the position error is negligible.

The oscillation frequency is affected by the power supply voltage and temperature of the PLL. Typically, the VCO of the NE 564 IC has the frequency drift with temperature 400 ppm/°C from 0 °C to 70 °C and the frequency change with the supply voltage 3% of  $\omega_0$  when the voltage is from 4.5 V to 5.5 V. The temperature of the experimental environment in the laboratory can change 1 °C. The frequency change can be as large as 3.84 KHz when the oscillator operates at 9.6 MHz. Since it takes a period of time for the temperature to change, the measurements should be done when the temperature becomes stable, e.g., waiting some time after turning the equipments on, and should be conducted in a short time. The supply voltage change is at most 1 mV in the experiment. This can cause 288 Hz frequency shift. To keep the stability of the frequency, stable power supply and stable temperature are needed.

The capacitance of a parallel-plate capacitor can be estimated by:

$$C = \epsilon_0 \frac{S}{d} \quad (5.13)$$

where  $S$  is the area of the plates and  $d$  is the separation of the two plates. In this experiment,  $S=0.12 \times 0.12 \text{ m}^2$  and  $d=0.02 \text{ m}$ . The capacitance is 6.4 pF while the total capacitance, including the sensor and the leads, is 24.95 pF. Due to the small capacitance of the sensor, the capacitance of leads is important. Since the leads' capacitance changes with their shapes and lengths, it is important to use short leads and fix their positions. In the experiment system, the semi-rigid lines are used. To prevent induced field, the cables are kept perpendicular to the field direction. After using above methods, the frequency shift caused by leads' capacitance change can be prevented. However, the presence of the leads also affects the distribution of the electric field.

The oscillation frequency used is 9.6 MHz, in order to obtain adequate absolute frequency shift. In this frequency range, electromagnetic interferences are serious.

## Chapter 6

### Discussion and Conclusions

The main objective of this thesis is to investigate the TDR technique as applied to the measurements of the dielectric properties of porous substances. New TDR sensors with uniform sensitivity were proposed and their characteristics were studied. The propagation of electromagnetic pulses in dispersive and porous dielectrics, such as soil, was also investigated.

Several new TDR sensors were proposed. Although it has the uniform field near its center area, the parallel-plate sensor has much higher field strength at the sensor's edge. To eliminate the high field strength at the edge of the parallel-plate sensor, dielectric shield was used. However, when the dielectric constant of the measured substance changes, the sensitivity of the sensor changes, too. This makes the measurement complex. Sensors with Rogowski's profile eliminate the high field strength at the edge by increasing the separation of two electrodes. This kind of sensor only has a small area of uniform field. Therefore, it is not satisfactory, either. Sensors with a flat part and a sinusoidal curve edge give a uniform field in the center area and have no high field at the edge. The sensor is also satisfactory for its definite sampling area. Three-electrode sensors have advantages in that the sampling area is between two outer electrodes. From comparison, the sensor with sinusoidal curved edge seems to be optimized. The weighing functions of these sensors were calculated. To match the sensor to the connecting cable, which is usually  $50 \Omega$ , the sensor was designed to have  $50 \Omega$  characteristic impedance. By using a 1:4 impedance transformer, the  $200 \Omega$  sensors can also be used in order to increase the sampling volume.

The sensitivity experiments for the parallel-plate sensor were conducted. The experiments use the perturbation method which utilizes a small dielectric perturbation object to measure the sensitivity through measuring the oscillation frequency change. The experimental results are consistent with the calculated weighing functions.

The propagations of ramp and gaussian pulses in dispersive media, such as soil and water, were investigated. The calculations show that the pulses are smeared by the dispersive media. The extension of the pulse width and flattening of the ramp edge make the measurement of pulse and ramp positions difficult. These results partly interpret the reason of the increase of rise-time in the ramp signal and width in the gaussian pulse in TDR soil moisture content measurement results. We also noticed that the magnitudes of the ramp do not decrease with the propagation in the soil, while those of the gaussian pulse decrease.

Overall, the new TDR sensors provide more definite sampling area and uniform measurement sensitivity than those presently used. The study shows that the measurement results of the new sensors are independent of the position of the small soil dielectric constant difference in the sensor's sampling area. Through the investigation of pulse propagation in dispersive media, the nature of the TDR trace was further understood. From the study, we learned that the pulse is smeared with the propagation by the dispersive medium, so that the accurate measurements of the propagation time of the pulse become difficult.

From this study, we can see that the TDR technique shows potential for measurements of the moisture content in the inhomogeneous media. Although they are some difficult to insert into soil, the proposed sensors can find more applications in industry, where the insertion of the sensor is not a problem. TDR technique can provide highly accurate, routine and non-destructive measurements at a reasonable cost. Therefore, the technique has great economic potential in practical measurements.

For further study, the configurations of the sensors need to be optimized to reduce the "tail" of the electric field and to obtain large uniform field area. More sensitivity

experiments of proposed sensors should be conducted. A method of interpreting the TDR trace and further more, an accurate measurement technique should be studied based on the pulse propagation results.

## Bibliography

- [1] C. M. K. Gardner, J. P. Bell, J. D. Cooper, T. J. Dean, and M. G. Hodnett, "Soil Water Content," in *Soil Analysis: Physical Methods* ed. C. E. Mullins, and K. A. Smith, New York: Marcel Dekker, 1991, pp. 1-73.
- [2] H. Fellner-Felldg, "The measurement of Dielectrics in the Time-domain," *J. Phy. Chem.*, vol. 73, pp. 616-623, Mar. 1969.
- [3] P. Hoekstra, and A. Delaney, "Dielectric Properties of soils at UHF and Microwave Frequencies," *J. Geophy. Res.*, vol. 79, pp. 1699-1708, April 1974.
- [4] G. C. Topp, J. L. Davis, and A. P. Annan, "Electromagnetic Determination of Soil Water Content: Measurements in Coaxial Transmission Lines," *Water Resour. Res.*, vol. 16, pp. 574-582, June 1980.
- [5] F. N. Dalton, and M. T. van Genuchten, "The Time-domain Reflectometry Method for Measuring Soil Water Content and Salinity," *Geoderma*, vol. 38, pp. 237-250, 1986.
- [6] S. Dasberg, and J. W. Hopmans, "Time Domain Reflectometry Calibration for Uniformly and Nonuniformly Wetted Sandy and Clayey Loam Soils," *Soil Sci. Soc. Am. J.*, vol. 56, pp. 1341-1345, Sept. 1992.
- [7] C. H. Roth, M. A. Malicki, and R. Plagge, "Empirical Evaluation of the Relationship between Soil Dielectric Constant and Volumetric Water Content and the Basis for Calibrating Soil Moisture Measurements by TDR," *J. Soil Sci.*, vol. 43, pp. 1-10, Mar. 1992.
- [8] O. H. Jacobsen, and P. Schjonning, "A Laboratory Calibration of Time Domain Reflectometry for Soil Water Measurement Including Effects of Bulk Density and Texture," *J. Hydrol*, vol. 151, pp. 147-157, Nov. 1993.
- [9] O. H. Jacobsen, and P. Schjonning, "Field Evaluation of Time Domain Reflectometry for Soil Water Measurements," *J. Hydrol*, vol. 151, pp. 159-172, Nov. 1993.

- [10] M. D. Bui, S. S. Stuchly, and G. I. Costache, "Propagation of Transients in Dispersive Dielectric Media," *IEEE Trans. Microwave Theory Tech.*, vol. 39, pp. 1165-1172, Jul. 1991.
- [11] A. Kraszewski, "Microwave Aquametry-A Review," *J. Microwave Power*, vol. 15, pp. 209-220, 1980.
- [12] A. W. Kraszewski, "Microwave Aquametry-Needs and Perspectives," *IEEE Trans. Microwave Theory Tech.*, vol. 39, pp. 828-835, May 1991.
- [13] M. A. Stuchly, and S. S. Stuchly, "Industrial, Scientific, Medical and Domestic Applications of Microwave," *Proc. IEE*, vol. 130, pt. A, pp. 467-503, 1983.
- [14] B. Brisco, T. J. Pultz, and R. J. Brown, "Soil Moisture Measurement Using Portable Dielectric Probes and Time Domain Reflectometry," *Water Resour. Res.*, vol. 28, pp. 1339-1346, May 1992.
- [15] S. J. Zegelin, I. White, and D. R. Jenkins, "Improved Field Probes for Soil-Water Content and Electrical Conductivity Measurement Using Time Domain Reflectometry," *Water Resour. Res.*, vol. 25, pp. 2367-2376, Nov. 1989.
- [16] J. H. Knight, "Sensitivity of Time Domain Reflectometry Measurements to Lateral Variations in Soil Water Content," *Water Resour. Res.*, vol. 28, pp. 2345-2352, Sept. 1992.
- [17] S. L. Hokett, J. B. Chapman, and S. D. Cloud, "Time Domain Reflectometry Response to Lateral Soil Water Content Heterogeneities," *Soil Sci. Soc. Am. J.*, vol. 56, pp. 313-316, Jan. 1992.
- [18] W. R. Hook, N. J. Livingston, Z. J. Sun, and P. B. Hook, "Remote Diode Shorting Improves Measurement of Soil Water Content by Time Domain Reflectometry," *Soil Sci. Soc. Am. J.*, vol. 56, pp. 1384-1391, 1992.
- [19] W. N. Herkelrath, S. P. Hamburg, and F. Murphy, "Automatic, Real-time Monitoring of Soil Moisture in a Remote Field Area With Time Domain Reflectometry," *Water Resour. Res.*, vol. 27, pp. 857-864, May 1991.
- [20] J. M. Baker, and R. R. Allmaras, "System for Automating and Multiplexing Soil Moisture Measurement by Time-domain Reflectometry," *Soil Sci. Soc. Am. J.*, vol. 54, pp. 1-6, Jan. 1990.
- [21] F. N. Dalton, W. N. Herkelrath, D. S. Rawlins, and J. D. Rhoades, "Time Domain Reflectometry: Simultaneous Measurement of Soil Water Content and Electrical Conductivity with a Single Probe," *Sci.*, vol. 224, pp. 989-990, June 1984.
- [22] S. Dasberg, and F. N. Dalton, "Time Domain Reflectometry Field Measurements of Soil Water Content and Electrical Conductivity," *Soil Sci. Soc. Am. J.*, vol. 49, pp. 293-297, 1985.

- [23] G. C. Topp, S. Yanuka, W. D. Zebchuk, and S. Zegelin, "Determination of Electrical Conductivity Using Time Domain Reflectometry: Soil and Water Experiments in Coaxial Lines," *Water Resour. Res.*, vol. 24, pp. 945-952, Jul. 1988.
- [24] M. Yanuka, G. C. Topp, S. Zegelin, and W. D. Zebchuk, "Multiple Reflection and Attenuation of Time Domain Reflectometry Pulses: Theoretical Considerations for Applications to Soil and Water," *Water Resour. Res.*, vol. 24, pp. 939-944, Jul. 1988.
- [25] W. R. Whalley, "Considerations on the Use of Time-domain Reflectometry (TDR) for Measuring Soil Water Content," *J. Soil Sci.*, vol. 44, pp. 1-9, Mar. 1993.
- [26] J. L. Davis, and A. P. Annan, "Electromagnetic Detection of Soil Moisture: Progress Report I," *Canadian J Remote Sensing*, vol. 3, pp. 76-86, Dec. 1977.
- [27] W. R. Tinga, and S. O. Nelson, "Dielectric Properties of Materials for Microwave Processing - Tabulated," *J Microwave Power*, vol. 8, pp. 23-65, Jan. 1973.
- [28] G. C. Topp, J. L. Davis, and A. P. Annan, "Electromagnetic Determination of Soil Water Content Using TDR: II. Evaluation of Installation and Configuration of Parallel Transmission Lines," *Soil Sci. Soc. Am. J.*, vol. 46, pp. 678-684, 1982.
- [29] W. Hilberg, *Electrical Characteristics of Transmission Lines*. Dedham: Artech, 1979, pp. 89-97.
- [30] R. C. Booton, Jr., *Computational Methods for Electromagnetics and Microwaves*. New York: Wiley, 1992, pp. 87-108.
- [31] E. Kuffel, and W. S. Zaengl, *High-voltage Engineering Fundamentals*. Oxford: Pergamon, 1984, pp. 214-237.
- [32] F. M. Bruce, "Calibration of Uniform-Field Spark-Gaps for High-Voltage Measurement at Power Frequencies," *Proc. IEE*, vol. 94, pt. II, pp. 138-149, 1947.
- [33] M. A. Malicki, "A reflectometric (TDR) meter of moisture content in soils and other capillary-porous materials," *Zeszyty Problemowe Postepow Nauk Rolniczych*, vol. 388, pp. 107-114, 1990.
- [34] M. A. Malicki, and W. M. Skierucha, "A Manually Controlled TDR Soil Moisture Meter Operating with 300 ps Rise-time Needle Pulse," *Irrig. Sci.*, vol. 10, pp. 153-163, 1989.
- [35] E. Nyfors, and P. Vainikainen, *Industrial Microwave Sensors*. Norwood: Artech, 1989, pp. 62-68.

## Appendix A

### Frequency Change by Dielectric Perturbation in Cavity

Conjugating (5.1) and (5.2), we get:

$$\nabla \times \vec{E}_0^* = -j\omega_0\mu_0\vec{H}_0^* \quad (\text{A.1})$$

$$\nabla \times \vec{H}_0^* = j\omega_0\varepsilon_0\vec{E}_0^* \quad (\text{A.2})$$

Multiply  $\vec{H}_0^*$  by (5.3), and  $E$  by (5.2). Then the former result subtracts the latter one and integrate in the volume  $v$ :

$$\int_v \left( \vec{H}_0^* \cdot \nabla \times \vec{E} - \vec{E} \cdot \nabla \times \vec{H}_0^* \right) dv = \int_v \left( -j\omega\mu\vec{H}_0^* \cdot \vec{H} + j\omega_0\mu_0\vec{E} \cdot \vec{E}_0^* \right) dv \quad (\text{A.3})$$

For left side of (A.3), apply relation  $\nabla \cdot (\vec{A} \times \vec{B}) = \vec{B} \cdot \nabla \times \vec{A} - \vec{A} \cdot \nabla \times \vec{B}$  and gradient theorem. It becomes:

$$\int_v \left( \vec{H}_0^* \cdot \nabla \times \vec{E} - \vec{E} \cdot \nabla \times \vec{H}_0^* \right) dv = \int_v \nabla \cdot \left( \vec{E} \times \vec{H}_0^* \right) dv = \oint_s \vec{E} \times \vec{H}_0^* \cdot \hat{n} ds = 0 \quad (\text{A.4})$$

where  $\hat{n}$  is the normal unit vector outward from the inner wall of the cavity. The last step of (A.4) uses the relation  $\vec{E} \times \vec{H}_0^* \cdot \hat{n} = \hat{n} \times \vec{E} \cdot \vec{H}_0^*$ . Since the wall of the cavity is assumed to be perfect conductor,  $\hat{n} \times \vec{E} = 0$ .

Then from (A.3) and (A.4), we obtain:

$$\begin{aligned}
 & \int_v \left( -j\omega\mu\vec{H}_0^* \cdot \vec{H} + j\omega_0\mu_0\vec{E} \cdot \vec{E}_0^* \right) dv \\
 &= \int_v j\omega_0\mu_0\vec{E} \cdot \vec{E}_0^* dv - \int_{v-v_1} j\omega\mu\vec{H}_0^* \cdot \vec{H} dv - \int_{v_1} j\omega\mu\vec{H}_0^* \cdot \vec{H} dv \\
 &= \int_v j\omega_0\mu_0\vec{E} \cdot \vec{E}_0^* dv - \int_v j\omega\mu\vec{H}_0^* \cdot \vec{H} dv - \int_{v_1} j\omega(\mu - \mu_0)\vec{H}_0^* \cdot \vec{H} dv \\
 &= 0
 \end{aligned} \tag{A.5}$$

Applying the same process to (5.4), we can similarly obtain:

$$\int_v j\omega_0\mu_0\vec{H} \cdot \vec{H}_0^* dv - \int_v j\omega\mu\vec{E}_0^* \cdot \vec{E} dv - \int_{v_1} j\omega(\varepsilon - \varepsilon_0)\vec{E}_0^* \cdot \vec{E} dv = 0 \tag{A.6}$$

Adding (A.5) and (A.6) and rearranging it, we get:

$$\frac{\omega - \omega_0}{\omega} = - \frac{(\varepsilon - \varepsilon_0) \int_{v_1} \vec{E} \cdot \vec{E}_0^* dv + (\mu - \mu_0) \int_{v_1} \vec{H} \cdot \vec{H}_0^* dv}{\varepsilon_0 \int_v \vec{E} \cdot \vec{E}_0^* dv + \mu_0 \int_v \vec{H} \cdot \vec{H}_0^* dv} \tag{A.7}$$

## Appendix B

### Index for Abbreviations

FDTD	Finite-difference time-domain method
FFT	Fast Fourier transform algorithm
PLL	Phase-locked loop
TDR	Time-domain reflectometry
TEM	Transverse electromagnetic mode
VCO	Voltage controlled oscillator

## VITA

Surname: Xiao Given Names: Bin  
Place of Birth: Beijing, China Date of Birth: April 4, 1967

### Educational Institutions Attended:

Tsinghua University, Beijing, China Sept. 1985-Jul. 1990

### Degrees Awarded:

Bachelor of Engineering in Electronic Engineering Jul. 1, 1990

### Honours and Awards:

Research Assistantships 1993-1994

### Publications:

Bin Xiao, Zhanping Li, and W. Ho, "Deconvoluting Calculation of CVV Auger Electron Spectrum," *Vacuum Science and Technology (in Chinese)*, vol. 11, pp. 263-272, 1991.

## Partial Copyright License

I hereby grant the right to lend my thesis (or dissertation) to users of the University of Victoria Library, and to make single copies only for such users or in response to a request from the Library of any other university, or similar institution, on its behalf or for one of its users. I further agree that permission for extensive copying of this thesis for scholarly purposes may be granted by me or a member of the University designated by me. It is understood that copying or publication of this thesis for financial gain shall not be allowed without my written permission.

Title of Thesis/Dissertation: Moisture Content Measurements Using Time-domain Techniques

Author



(Signature)

Bin Xiao

(Name in Block Letters)

Jan 10, 1995

(Date)